Karlsruhe Institute of Technology

ETP-KA/2025-17

Measurement of the Charge Asymmetry in WH($\tau\tau$) Events in pp Collisions at 13 TeV at the LHC

Zur Erlangung des akademischen Grades eines

Doktors der Naturwissenschaften

von der KIT-Fakultät für Physik des
Karlsruher Instituts für Technologie (KIT)

vorgelegte

Dissertation

von

M.Sc. Ralf Schmieder

aus Schapbach

Erstgutachter: Priv. Doz. Dr. Roger Wolf
Zweitgutachter: Prof. Dr. Markus Klute

Tag der mündlichen Prüfung: 28.11.25

Institut für experimentelle Teilchenphysik

Declaration

I hereby declare that I have completed this work independently and have not used any sources or aids other than those cited in the text. All content taken from other works has been appropriately cited. In cases writing aids such as Large Language Models have been used in this thesis, I confirm that their output was derived from my own original work, and the sole function of the tool was to correct grammar and language wherever applicable. I take full responsibility for all erroneous content, incorrect references and plagiarism arising from the usage of such tools.

Karlsruhe, December 1, 2025	Ralf Schmieder
Place, Date	**Ralf Schmieder**

Abstract

The discovery of the Higgs boson in 2012 completed the particle content of the Standard Model (SM) and enabled detailed studies of its properties. While couplings to gauge bosons and third-generation fermions are well established, the coupling to charm quarks remains largely unconstrained. Direct searches for $H \to cc$ decays face severe challenges from QCD backgrounds and jet flavor identification. This thesis presents a complementary, indirect approach based on the measurement of the charge asymmetry in associated WH production, which is sensitive to the charm Yukawa coupling.

The analysis is performed using the full Run 2 dataset of the CMS experiment at the LHC, corresponding to an integrated luminosity of 138 fb^{-1}. Since the end of the Run 2 the data have been re-analyzed with improved and consistent simulation, detector alignments and calibrations throughout the data-taking years, by the CMS Collaboration. Events are selected in final states where the Higgs boson decays to a pair of τ leptons and the accompanying W boson decays to an electron or muon and a corresponding neutrino. Multiple $\tau\tau$ final states are reconstructed, and advanced analysis techniques are employed to enhance the sensitivity of the analysis. Backgrounds from jets misidentified as leptons are estimated with a data-driven F_F method, while genuine multi-lepton backgrounds are modeled with simulation. A neural network classifier is trained to distinguish signal from background and to provide event categorization, improving statistical precision and control over systematic uncertainties.

This work presents the first measurement of the WH charge asymmetry in $H \to \tau\tau$ decays, along with measurements of the WH, W^+H, and W^-H production cross sections. These measurements contribute to the global program of precision Higgs boson measurements, which aim to test the SM and probe for possible signs of physics beyond the SM.

Contents

1. Introduction

The Standard Model of particle physics (SM) has been remarkably successful in describing the fundamental particles and their interactions. Many of its predictions, such as the existence of the W and Z bosons, were confirmed experimentally long after they were theoretically proposed. The last missing piece, the Higgs boson (H), was predicted in 1964 through the Brout–Englert–Higgs (BEH) mechanism [1–6] and observed in 2012 by the ATLAS [7] and CMS [8] Collaborations at the Large Hadron Collider [9] (LHC) [10, 11]. This discovery confirmed the mechanism responsible for electroweak symmetry breaking and the generation of particle masses.

Despite these achievements, the SM is incomplete. It does not provide a description of gravity and cannot explain the observed dark matter content of the universe. Many other open questions remain, pointing to physics beyond the SM (BSM). The LHC is designed to address these questions by exploring two main avenues: the discovery of new particles at the highest accessible energies, and precision tests of the SM searching for deviations from its predictions. The Higgs sector plays a central role in both strategies. The BEH mechanism does not require the existence of only one Higgs boson, leaving room for extended models. At the same time, precise measurements of Higgs boson couplings may reveal subtle signs of BSM physics.

Since its discovery, the couplings of the Higgs boson have been tested in several channels. Its decays to heavy gauge bosons (W [12–14], Z [15–17]), photons [18, 19], b [20, 21] and top quarks [22–25], and τ leptons [26, 27] are established. Together, these measurements confirm couplings to all known gauge bosons and third-generation fermions. More recently, evidence for the rare $H \to \mu\mu$ decay provided the first direct probe of second-generation Yukawa couplings [28, 29]. The next step is the investigation of the Higgs boson coupling to charm quarks for which the ATLAS and CMS Collaborations have reported upper limits [30–33].

Among the fermionic final states, the decay into τ leptons is of particular interest. The τ lepton is the heaviest lepton, and its Yukawa coupling is therefore sizable. In fact, the $H \to \tau\tau$ final state provides the highest sensitivity to Higgs boson couplings in the Yukawa sector. At the same time, its analysis is challenging due to the many possible τ lepton decay modes and the presence of neutrinos in the final state, which escape undetected.

This thesis presents a measurement of the WH production mode with $H \to \tau\tau$ decays using the full reprocessed Run 2 dataset of the CMS experiment, with improved simulation, detector alignments and calibrations. The analysis targets the associated production of a Higgs boson with a W boson and the charge asymmetry between W^+H and W^-H production. The latter is in particular interesting to constrain the charm quark Yukawa coupling.

Events are selected in final states containing hadronic τ lepton decays, electrons, and muons. A main challenge of the analysis is the suppression and precise modeling of the

large backgrounds, in particular top quark pair (tt), Drell-Yan, W+jets and WZ production. To address this, the data-driven F_{F} method is used to estimate backgrounds from jets misidentified as leptons. Genuine multi-lepton backgrounds are estimated from simulation. A neural network (NN) is trained to optimally separate signal from background and to classify events into categories enriched in different processes. This multi-classification approach increases the sensitivity of the analysis and provides dedicated control regions to constrain systematic uncertainties.

The structure of the thesis is as follows. Chapter 2 introduces the theoretical background of the SM Higgs sector and the relation between the charge asymmetry in the WH production and the charm quark Yukawa coupling. Chapter 3 describes the CMS detector and its reconstruction algorithms. Chapter 4 explains the event selection, the overall analysis strategy and the results, and Chapter 5 concludes with a summary and outlook.

2. The Standard Model of Particle Physics

The SM is a theory that provides a comprehensive framework to describe all known fundamental particles and their interactions. Based on the symmetries of the universe, the SM successfully predicts the kinematic behavior, creation, and annihilation of elementary particles. These particles are classified into two main categories: fermions, which have half-integer spin and constitute matter, and bosons, which have integer spin and mediate the fundamental forces between matter particles, which are the weak, electromagnetic, and strong forces. Considered as the fourth fundamental force, the gravitational force cannot be described by the SM. The complete set of SM particles is shown in Figure 2.1.

Fermions are further divided into quarks and leptons, depending on the interactions they are involved in. Leptons participate only in electroweak interactions, whereas quarks participate in the strong interaction as well. Due to this fact, quarks and leptons show very different characteristics. Furthermore, fermions are organized into three generations, differing primarily in mass, with the first-generation fermions forming the matter that makes up our everyday lives. These are the up and down quarks forming protons and neutrons, and the electrons. The quarks are grouped into the up-type (electric charge +2/3) and down-type (electric charge −1/3) quarks. The leptons are grouped into charged leptons and neutral leptons, which are the neutrinos (ν). The Higgs boson is a scalar particle with spin zero. Unlike other bosons, it does not act as a force carrier. It evolves from the BEH mechanism, described below.

Mathematically described as a quantum field theory (QFT), the SM unifies quantum mechanics and special relativity in a field theory. The system is described by a Lagrangian density that determines the dynamics of the particles and is required to be invariant under symmetry transformations. These symmetries are related to Lorentz invariance but also to the three fundamental forces described by the SM. In mathematical terms, the three forces arise in the Lagrangian density by requiring the invariance of the Lagrangian density under local $\mathrm{SU}(3)_c \times \mathrm{SU}(2)_L \times \mathrm{U}(1)_Y$ transformations:

- The **electromagnetic force** is mediated by the massless photon and acts on electrically charged particles. It is of infinite range and relatively strong compared to the weak and gravitational forces. At the classical level it is described by Maxwell's equations, while in the SM it is formulated as a QFT.

- The **weak force** interacts very weakly compared to the other two forces described by the SM. With a similar coupling strength compared to the electromagnetic force, the weak force is mediated by the W and Z bosons. As both bosons carry a heavy mass, the force acts only at a very limited range 100 times smaller than the protons' diameter, which is the reason for its weakness. It is responsible for flavor-changing particle decays and is embedded in the SM through the electroweak theory [34–36]. This

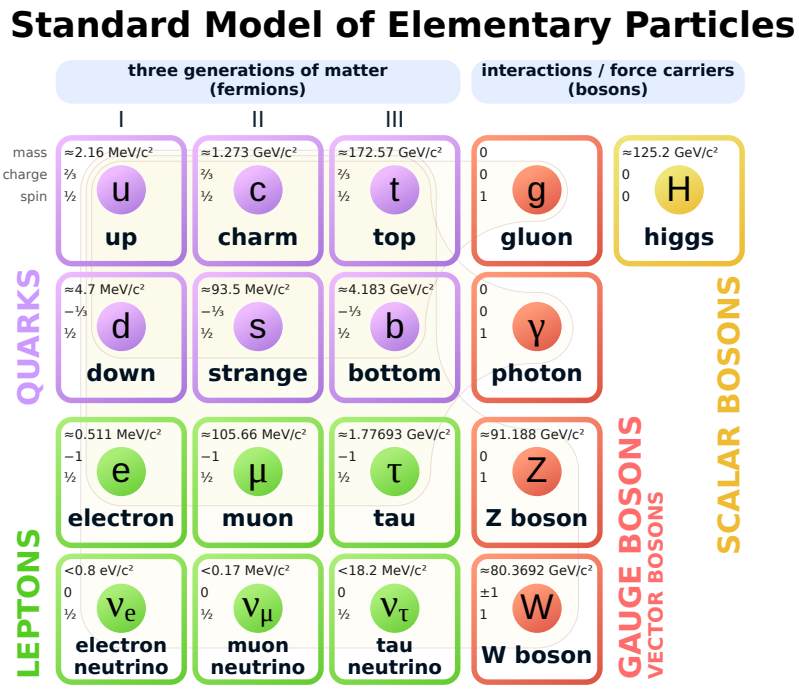

Figure 2.1.: Particles of the SM [37].

theory unifies the electromagnetic and the weak force into one fundamental force, the electroweak force. It is described by the gauge symmetry $\mathrm{SU}(2)_L \times \mathrm{U}(1)_Y$. The $\mathrm{SU}(2)_L$ group acts on the weak isospin I_3, while the $\mathrm{U}(1)_Y$ group acts on hypercharge.

- The **strong force** is described by quantum chromodynamics, a gauge theory with symmetry group $\mathrm{SU}(3)_c$. It acts in the three-dimensional color space and is mediated by massless gluons. The force grows with the distance between color-charged particles, a behavior opposite to that of electromagnetism. At short distances, quarks and gluons behave almost as free particles, a property known as asymptotic freedom. At large distances, the potential increases until new quark-antiquark pairs are created, leading to a phenomenon usually referred to as confinement. As a result, only color-neutral bound states, the hadrons, are observable, while free quarks and gluons cannot be isolated.

The Brout-Englert-Higgs Mechanism

The BEH mechanism [1–6] completed the SM by providing an explanation for the origin of elementary particle masses. Mass is an intrinsic and directly measurable property of elementary particles. However, the symmetries of the SM forbid the straightforward inclusion of mass terms for both bosons and fermions. In the case of vector bosons, a mass term would read like

$$\mathcal{L}_{\text{mass}} = -m_G^2 G_\mu G^\mu \,, \tag{2.1}$$

where G_μ is a generic vector field. Mass terms for bosons break the gauge symmetry of the SM Lagrangian density, while those for fermions violate the chiral symmetry of the $\mathrm{SU}(2)_L$ group. Instead of adding such a mass term, the BEH mechanism provides a consistent method for dynamically generating such mass terms through spontaneous symmetry breaking (SSB). In this framework, the vacuum state does not respect the full symmetry of the theory. Specifically, the electroweak symmetry of the $\mathrm{SU}(2)_L \times \mathrm{U}(1)_Y$ gauge group is broken down to the $\mathrm{U}(1)_Q$ symmetry of quantum electrodynamics (QED). This happens via the introduction of a complex scalar $\mathrm{SU}(2)_L$ doublet field Φ:

$$\Phi = \begin{pmatrix} \phi^+ \\ \phi^0 \end{pmatrix}. \tag{2.2}$$

The interaction of Φ with the SM Lagrangian density is described by

$$\mathcal{L}_{\text{Higgs}} = |D_\mu \Phi|^2 - V(\Phi^\dagger \Phi), \tag{2.3}$$

where D_μ is the covariant derivative associated with the electroweak gauge symmetry group $\mathrm{SU}(2)_L \times \mathrm{U}(1)_Y$ and is explicitly defined as

$$D_\mu = \partial_\mu - igW_\mu^a \frac{\sigma^a}{2} - ig' \frac{Y}{2} B_\mu, \tag{2.4}$$

with g and g' being the gauge coupling constants for the SU(2) and U(1) groups respectively and the σ^a are the Pauli matrices.

The scalar potential responsible for SSB is given by

$$V(\Phi^\dagger \Phi) = -\mu^2 \Phi^\dagger \Phi + \frac{\lambda}{2} (\Phi^\dagger \Phi)^2, \tag{2.5}$$

where μ and λ are real constants. The vacuum expectation value (VEV) of the field is found by minimizing the potential at

$$\langle \Phi^\dagger \Phi \rangle = \frac{\mu^2}{\lambda} \equiv \frac{v^2}{2}. \tag{2.6}$$

Only the neutral component of Φ can acquire a VEV to preserve the electric charge. In the unitary gauge, the scalar field becomes

$$\Phi = \frac{1}{\sqrt{2}} \begin{pmatrix} 0 \\ v + h \end{pmatrix}, \tag{2.7}$$

where h is the physical Higgs boson field.

Focusing on the non-derivative parts of $|D_\mu \Phi|^2$, the mass terms for the gauge bosons are obtained:

$$m_{\mathrm{W}} = \frac{1}{2} g v, \quad m_{\mathrm{Z}} = \frac{1}{2} \sqrt{g^2 + g'^2}\, v. \tag{2.8}$$

Three degrees of freedom of the scalar doublet are absorbed in order to give mass to the $\mathrm{W}^\pm$ and Z bosons. The remaining degree of freedom manifests as the Higgs boson, with its mass given by $m_{\mathrm{H}} = \sqrt{2\lambda} v$. Interaction terms between the Higgs field and the massive

vector bosons appear with strengths proportional to the square of the respective boson masses. Fermion mass terms of the form

$$\mathcal{L}_{\text{mass}} = -m\bar{\psi}\psi \tag{2.9}$$

are not gauge invariant under $\mathrm{SU}(2)_L \times \mathrm{U}(1)_Y$, as they couple left- and right-handed fermions, which transform differently. To provide fermions with masses while preserving gauge invariance, Yukawa couplings to the scalar field are introduced. For the electron, the interaction is written as

$$\mathcal{L}_{\text{Yukawa}} = -\lambda_{\mathrm{e}}(\bar{\mathrm{E}}_L \Phi \mathrm{e}_R + \bar{\mathrm{e}}_R \Phi^{\dagger} \mathrm{E}_L), \tag{2.10}$$

where λ_{e} is a dimensionless coupling constant, $\bar{\mathrm{E}}_L = (\bar{\nu}_{\mathrm{e}L}, \bar{\mathrm{e}}_L)$ is the left-handed lepton SU(2)-doublet, and e_R is the right-handed electron which is an SU(2)-singlet. After symmetry breaking, in the unitary gauge, this becomes:

$$\mathcal{L}_{\text{Yukawa}} = -\frac{\lambda_{\mathrm{e}} v}{\sqrt{2}}\left(1 + \frac{h}{v}\right)(\bar{\mathrm{e}}_L \mathrm{e}_R + \bar{\mathrm{e}}_R \mathrm{e}_L) \tag{2.11}$$

$$= -m_{\mathrm{e}}\bar{\mathrm{e}}\mathrm{e} - \frac{m_{\mathrm{e}}}{v}\bar{\mathrm{e}}\mathrm{e}h, \tag{2.12}$$

where the electron mass is given by $m_{\mathrm{e}} = \frac{\lambda_{\mathrm{e}} v}{\sqrt{2}}$ and $\mathrm{e} = \mathrm{e}_L + \mathrm{e}_R$ is the full Dirac field. The same mechanism also generates the masses of other leptons and quarks. For all fermions, the masses are proportional to v.

Higgs Boson Phenomenology

The discovery of the Higgs boson in 2012 by the ATLAS and CMS Collaborations marked a significant milestone in particle physics, confirming the final missing element of the SM predicted by the BEH mechanism. At hadron colliders like the LHC at CERN, Higgs bosons are produced through various mechanisms, each initiated by the quark and gluon constituents of the colliding protons. The dominant production channel is gluon fusion (ggF), in which gluons interact via a heavy-quark loop, primarily involving top quarks. Other important production modes include vector boson fusion (VBF), characterized by two forward jets resulting in little hadronic activity in the central detector, and Higgsstrahlung, where the Higgs boson is emitted from an off-shell vector boson produced in association with a W or Z boson. Associated production with heavy quarks, such as top or b quark pairs has smaller cross sections. The leading order Feynman diagrams of the main production channels are given in Figure 2.2.

The Higgs boson decays preferentially to the heaviest kinematically allowed SM particles due to its coupling being proportional to the particle mass. The largest branching fraction corresponds to decays into b quark pairs, followed by WW and ZZ decays, where one of the vector bosons must be off-shell due to the Higgs mass of approximately 125 GeV. Although rarer, decays into two photons via a quark loop and four leptons via ZZ offer clean experimental signatures and were pivotal in the discovery. In Figure 2.3 the branching fractions of the different final states of the SM Higgs boson are displayed. In the years

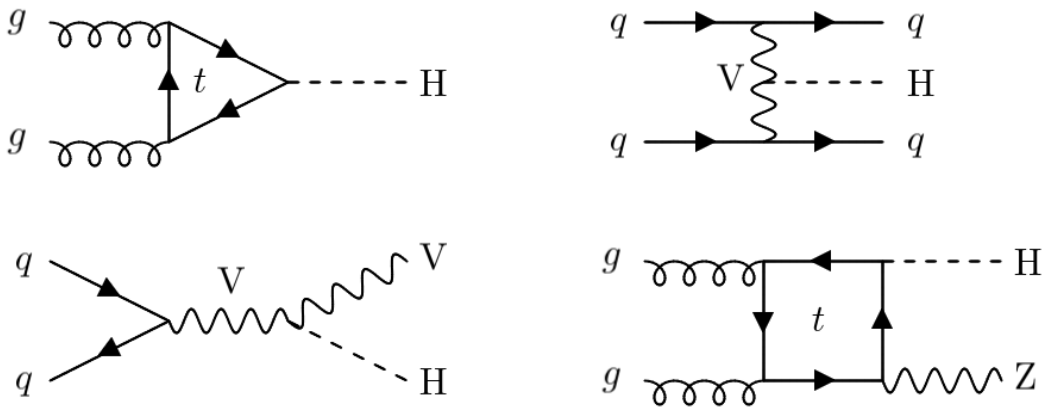

Figure 2.2.: Feynman diagrams of the major Higgs boson production channels at the LHC, which are ggF (upper left), VBF (upper right) and VH production (bottom).

following the discovery, further studies have confirmed Higgs boson couplings to third-generation fermions such as top [22–25] and b quarks [20, 21], and τ leptons [26, 27]. Notably, the $H \to \tau\tau$ decay channel, due to its manageable background and clean leptonic final states, has become a key probe of the Yukawa interaction and remains a central focus in ongoing analyses.

Higgs Boson to Charm Quark Coupling

A main goal in ongoing Higgs boson research is probing the couplings to second-generation fermions, which remains a major challenge. There is now experimental evidence for the Higgs boson decaying into a pair of muons, a second-generation process, as reported by the CMS and ATLAS Collaborations [28, 29]. The next target in the less well-constrained second-generation sector is to measure the charm quark Yukawa coupling. A direct search for the $H \to cc$ decay aims to probe this coupling but faces considerable experimental difficulty due to the overwhelming jet background at the LHC. Discriminating charm quark jets from those initiated by light or b quarks requires dedicated multivariate techniques, including charm-tagging algorithms trained to exploit differences in hadronization and decay patterns. Both ATLAS and CMS have performed searches for this decay mode and set upper limits on the charm quark Yukawa coupling, though a direct observation has not yet been achieved [39–42]. An alternative, indirect approach to constraining the charm quark Yukawa coupling involves studying the charge asymmetry in associated Higgs boson production with $W^{\pm}$ bosons (WH) which is defined as

$$A = \frac{\sigma(W^+H) - \sigma(W^-H)}{\sigma(W^+H) + \sigma(W^-H)}. \tag{2.13}$$

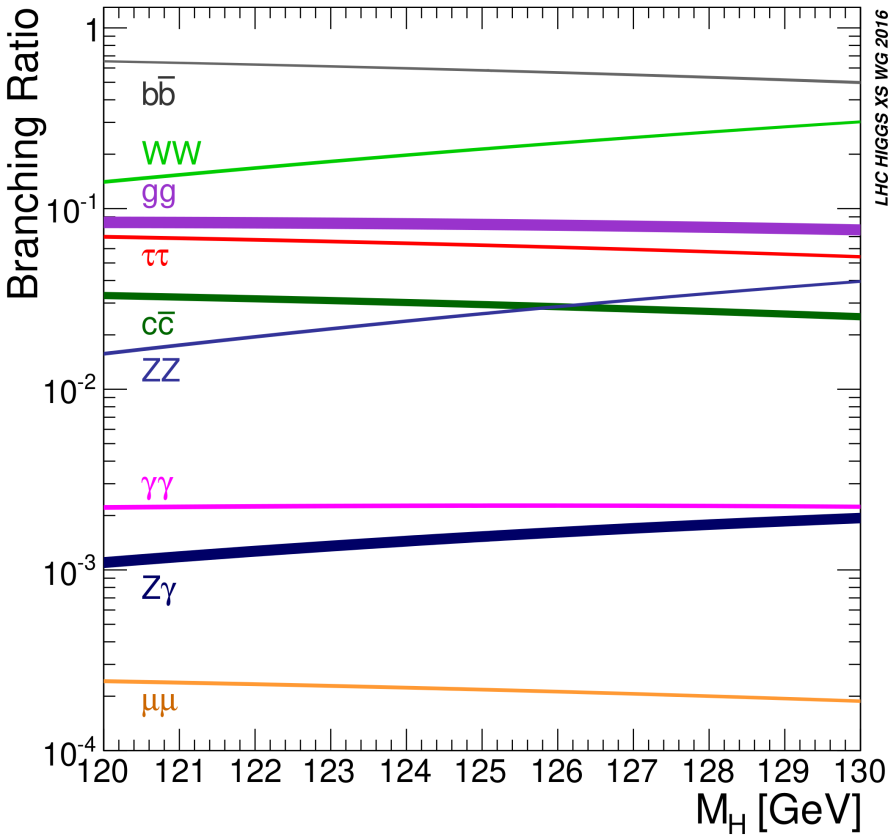

Figure 2.3.: The dependence of the Higgs boson's branching fractions on its mass. Taken from [38].

Due to the proton's parton distribution functions, more W^+ than W^- bosons are produced in proton-proton (pp) collisions, leading to a well-predicted charge asymmetry in the SM [43] of

$$A_{\mathrm{SM}} = 0.22 \pm 0.01. \tag{2.14}$$

In the WH process, contributions from Feynman diagrams involving t-channel quark exchange are sensitive to Higgs boson Yukawa couplings. Feynman diagrams of those production processes are given in Figure 2.4. An enhancement of the up or down quark Yukawa coupling increases the predicted asymmetry beyond the SM expectation. In contrast, an enhancement of the charm or strange quark Yukawa coupling decreases the asymmetry [44]. This dependence is illustrated in Figure 2.5, which shows the charge asymmetry in pp$\longrightarrow W^{\pm}H$ production at $\sqrt{s} = 14\,\mathrm{TeV}$ as a function of the Yukawa rescaling factor $\tilde{\kappa}_f$, with $\tilde{\kappa}_f^{\mathrm{SM}} \approx 0.23$. The observable therefore provides a clean and largely model-independent probe of light-quark Yukawa couplings. In particular, it offers an indirect method to constrain the charm Yukawa coupling, complementary to direct searches in the $H \longrightarrow cc$ decay mode.

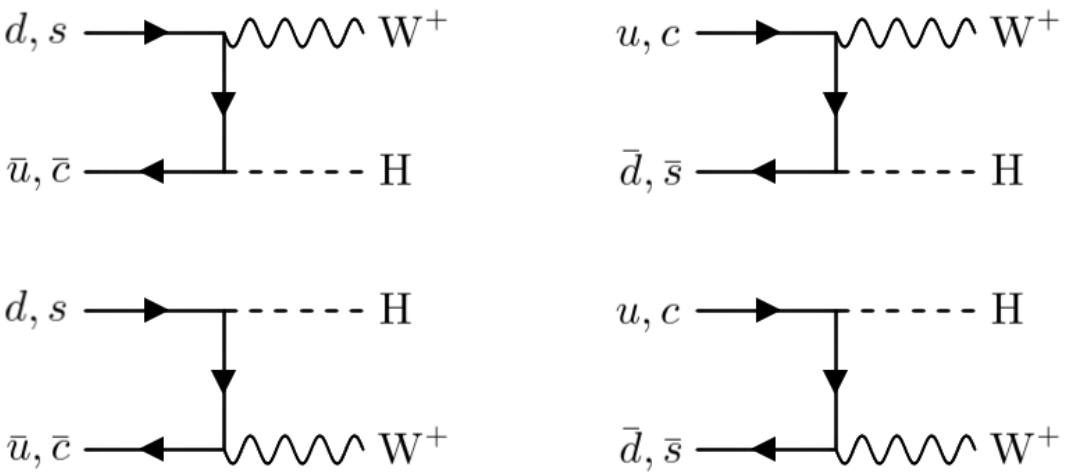

Figure 2.4.: Feynman diagrams of WH production involving a quark exchange in the t-channel, sensitive to light quark Yukawa couplings.

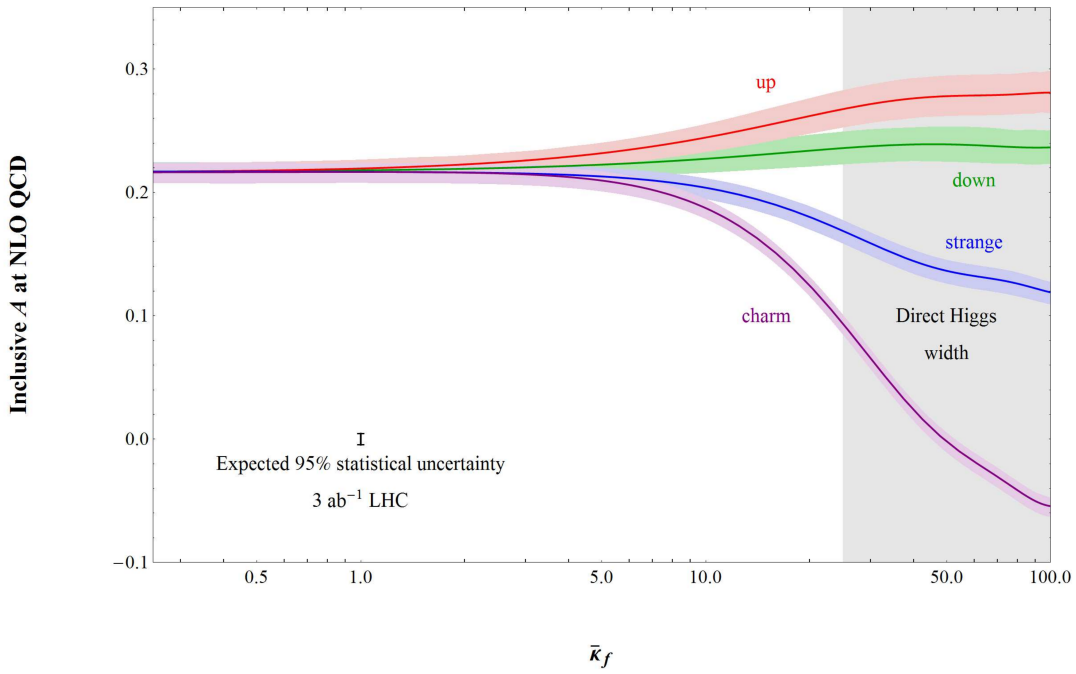

Figure 2.5.: Charge asymmetry for different Yukawa couplings scanned by $\tilde{\kappa}_f = m_f/m_b \cdot \kappa_f$, with κ_f defined as the coupling modifier for a given fermion f. Taken from [44].

3. The CMS Experiment

The data used in this analysis is collected by the CMS experiment, one of the four main detectors operating at the LHC at CERN near Geneva, Switzerland. The LHC is a 27-kilometer circular accelerator mainly to collide protons but also heavy ions. Since its commissioning in 2010, it has provided pp collisions at unprecedented energies, with Run 2 (2016–2018) reaching a center-of-mass energy of 13 TeV. During this period, protons were grouped into bunches, each containing approximately 10^{11} protons, with around 2500 bunches per beam circulating simultaneously. A minimum bunch spacing of 25 ns allowed for collision rates up to 40 MHz.

The LHC features four primary interaction points where beams are brought to collision, each instrumented with a large-scale detector: Compact Muon Solenoid (CMS) [8], A Toroidal LHC Apparatus (ATLAS) [7], A Large Ion Collider Experiment (ALICE) [45], and LHC-beauty (LHCb) [46]. CMS and ATLAS are general-purpose detectors designed to explore a broad range of SM and BSM physics. In contrast, ALICE specializes in studying heavy-ion collisions and the properties of the quark-gluon plasma, while LHCb focuses on precision measurements involving b quark decays and CP violation.

Following Run 2, Run 3 began in 2022 with an increased center-of-mass energy of 13.6 TeV and aims to collect a total integrated luminosity of up to $350\,\text{fb}^{-1}$ by the end of Run 3 in 2026. In the longer term, after a major upgrade phase, the LHC is expected to deliver up to $3000\,\text{fb}^{-1}$ of data, significantly enhancing the discovery potential and precision measurements at the energy frontier.

3.1. The CMS Detector

As illustrated in Figure 3.1, CMS features a cylindrical geometry centered around the collision point, with multiple concentric layers of detector components designed to measure the properties of particles produced in pp collisions. These layers utilize different detector technologies, each optimized for trajectory measurement, energy measurement, or particle identification, forming a highly integrated system capable of reconstructing complex final states. CMS employs a Cartesian coordinate system aligned with the nominal interaction point to describe particle trajectories and detector geometry. As shown in Figure 3.2, the x-axis points towards the center of the LHC ring, the y-axis extends vertically upward, and the z-axis follows the direction of the counterclockwise circulating proton beam. In addition to this, a polar coordinate system is used to account for the cylindrical symmetry of the detector. The azimuthal angle ϕ is measured in the plane perpendicular to the beam direction relative to the x-axis, while the polar angle θ is measured relative to the z-axis. To characterize particle directions more effectively, especially for relativistic particles, the

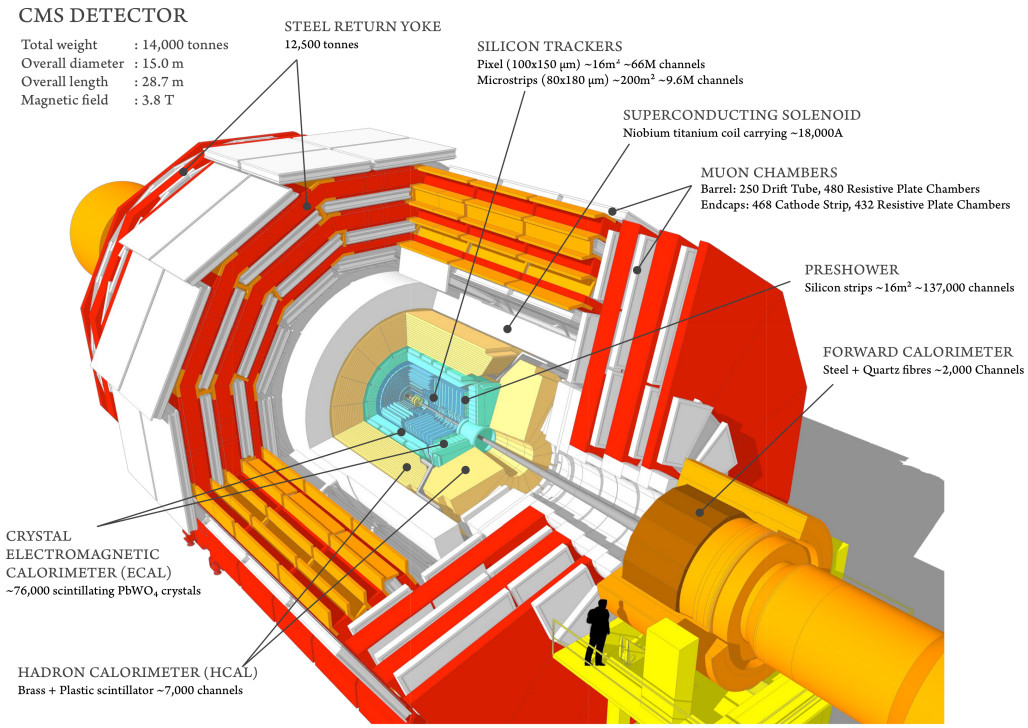

Figure 3.1.: Sketch of the CMS detector with its sub-detectors, build cylindrically around the beam pipe. Taken from [47].

variable pseudorapidity η is typically used instead of the polar angle. It is defined as

$$\eta = -\ln(\tan(\theta/2)) \tag{3.1}$$

and has the advantage of being invariant under Lorentz transformations along the beam axis. Therefore, it is a convenient quantity for comparing events and analyzing detector coverage. The following sections provide a brief overview of each CMS sub-detector, based primarily on [8], which offers more detailed technical documentation.

3.1.1. Silicon Tracker

At the core of the CMS detector lies the inner tracking system, surrounding the interaction point. Its primary function is to reconstruct the trajectories of charged particles with high precision, enabling accurate measurements of their momentum and the location of the primary collision vertex (PV). The tracking system operates within a strong magnetic field, which causes charged particles to curve due to the Lorentz force. Based on this curvature, the particle momentum is determined.

The innermost component of the tracker is the pixel detector. It consists of four barrel layers made of high-resolution silicon pixel sensors, each with a pixel size of 100 x150 μm^2, positioned at radial distances of 2.9 cm, 6.8 cm, 10.9 cm, and 16.0 cm from the beam axis. These are complemented by six forward pixel disks, located at $z = \pm 29.1$ cm, $z = \pm 39.6$ cm,

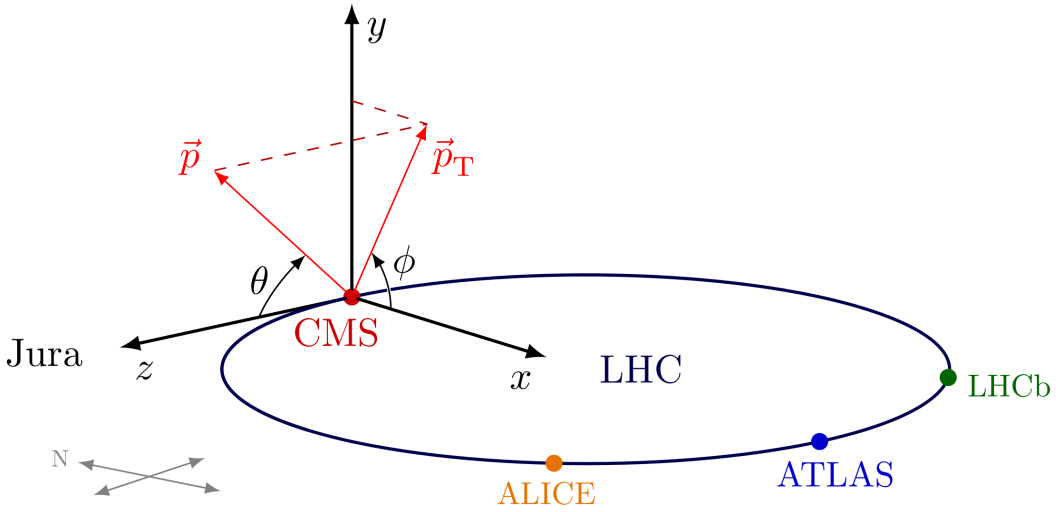

Figure 3.2.: Sketch of the CMS detector with its sub-detectors, build cylindrically around the beam pipe. Taken from [48].

and $z = \pm 51.6$ cm, which extend the coverage in the forward regions, allowing full tracking capability up to pseudorapidity values of $|\eta| < 2.5$. [49]

Surrounding the pixel detector is the silicon strip tracker, which forms the outer portion of the inner tracking system. It spans a radial range from approximately 25 cm to 116 cm and maintains full coverage within the same pseudorapidity range as the pixel system. The strip tracker is divided into several subcomponents: the tracker inner barrel and disks, the tracker outer barrel, and the tracker endcaps. Each region employs different types of silicon strip sensors tailored to their location and function. Together, the entire tracking system comprises roughly 75 million readout channels, enabling detailed and efficient reconstruction of particle trajectories throughout the CMS detector volume.

The transverse momentum (p_T) resolution of the tracker can be described with a simple two-term form

$$\frac{\sigma_{p_T}}{p_T} \approx \underbrace{\frac{a}{B\,L^2}\,\sigma_x\,p_T}_{\text{hit resolution}} \oplus \underbrace{\frac{b}{B\,\sqrt{LX_0}}}_{\text{multiple scattering}} , \tag{3.2}$$

where B is the magnetic field, L the effective lever arm, σ_x the hit resolution, X_0 the radiation length, and a, b are geometry/material constants. The first term grows linearly with p_T and improves with better hit resolution, stronger B, and larger L. The second term describes the contribution of multiple scattering and becomes more dominant at low p_T. It is approximately momentum independent and is set by the amount of material.

3.1.2. Electromagnetic Calorimeter

Surrounding the tracking system is the electromagnetic calorimeter (ECAL), which is designed to precisely measure the energy of electrons and photons. It functions by fully absorbing the particles and converting their energy into light using lead tungstate ($PbWO_4$)

crystals. These crystals have a high density ($8.28\,\mathrm{g/cm^{-3}}$) and short radiation length (0.89 cm), which, together with their small Molière radius (2.2 cm), enable a compact, finely segmented calorimeter suitable for high-resolution measurements.

The ECAL is composed of multiple subsystems, each optimized for different detector regions using varying crystal geometries and photodetector types. The barrel section covers the central detector region ($|\eta| < 1.479$) and is located at radii of 129–152 cm from the beam axis. The total length of this section corresponds to approximately 25.8 radiation lengths, allowing for effective energy containment. In the forward regions, the ECAL endcaps extend the coverage to $|\eta| < 3.0$ and are positioned at $z = \pm 315.4$ cm. Each endcap crystal measures 220 mm in length, equivalent to about 24.7 radiation lengths.

In front of the endcaps, the ECAL preshower system provides additional discrimination between photons and neutral pions. It is a sampling calorimeter that uses alternating layers of lead absorbers and silicon strip detectors. This setup improves the identification of electromagnetic showers in the forward region.

Altogether, the ECAL consists of 75848 lead tungstate crystals, each read out individually, providing high granularity and precise spatial and energy resolution across the pseudorapidity range up to $|\eta| < 3.0$.

The ECAL's energy resolution is characterized by three main contributions, each with a distinct dependence on the particle energy. It is typically expressed as

$$\frac{\sigma_E}{E} = \frac{S}{\sqrt{E}} \oplus \frac{N}{E} \oplus C. \tag{3.3}$$

The first term, known as the stochastic term, accounts for statistical fluctuations in the shower development and light collection within the crystals. The second, the noise term, represents contributions from electronic and digitization noise, which are more significant at low energies. The final term, the constant term, includes residual calibration errors and other effects.

3.1.3. Hadronic Calorimeter

Surrounding the ECAL, the hadronic calorimeter (HCAL) is responsible for measuring the energy of hadrons and other particles that do not deposit their full energy in the ECAL. As a sampling calorimeter, the HCAL consists of alternating layers of dense absorber material and active scintillating material. Specifically, brass is used as the absorber, while plastic scintillators serve as the active medium. When hadrons interact with the absorber and produce showers, the resulting scintillation light is collected via wavelength-shifting fibers and read out by silicon photomultipliers.

The HCAL is segmented into several subsystems, each designed to cover different regions in pseudorapidity and radial distance. The central part of the HCAL, known as the HCAL barrel, covers the region $|\eta| < 1.3$ and is positioned between radii of 1.77 m and 2.95 m, extending up to the inner surface of the superconducting solenoid. Outside the solenoid lies the HCAL outer, also referred to as the "tail catcher," which provides additional depth for hadronic energy containment in the same pseudorapidity region by using the solenoid itself as part of the absorber structure.

At higher pseudorapidities, the HCAL endcaps extend the coverage to the range $1.3 < |\eta| < 2.5$, located adjacent to the ECAL endcaps. In the very forward region, the HCAL forward calorimeters cover $2.8 < |\eta| < 5.2$ and are situated approximately 11.2 m from the interaction point. Unlike the other HCAL subsystems, it uses quartz fibers embedded in steel to detect Cherenkov radiation produced by the electromagnetic component of particle showers, enabling energy measurements in regions where radiation levels and particle flux are highest.

3.1.4. Solenoid and Return Yoke

A key feature that distinguishes the CMS detector is its powerful superconducting solenoid, which produces a uniform magnetic field of 3.8 T within its interior volume. This large-scale magnet is 6 m in diameter, 12.5 m long, and weighs approximately 220 t. It is energized by a high-current power supply delivering 20 kA. Enclosed within the solenoid's free bore are the inner tracking system and calorimeters, which operate within this magnetic field to enable precise particle measurements.

Surrounding the solenoid is a 10000 t iron return yoke that serves both to contain the magnetic flux within the detector and to provide mechanical support. This structure houses the vacuum vessel and encloses four layers of superconducting niobium-titanium coils. Together, the solenoid and return yoke account for nearly 90 % of the CMS detector's total mass.

The magnetic field plays a critical role in charged particle reconstruction. As charged particles move through the field, their trajectories bend due to the Lorentz force. This curvature not only allows for the determination of a particle's charge sign based on the direction of its deflection but also allows to measure the particle's momentum from the radius of curvature.

3.1.5. Muon Chambers

Integrated into the iron return yoke is the muon detection system, which is responsible for identifying and measuring muons—particles that typically traverse the entire detector without being absorbed by the calorimeters. To achieve this, CMS employs a combination of gaseous detectors, each optimized for different regions of the detector and providing complementary information.

In the barrel region of the detector, up to $|\eta| < 1.2$, muons are detected using 250 drift tube chambers arranged in four layers. These chambers are filled with a gas mixture of argon and carbon dioxide. As charged particles pass through the gas, they ionize it, and the resulting free electrons drift towards positively charged wires, generating a signal. By combining signals from multiple drift tubes, the particle's trajectory can be reconstructed with high precision.

In the endcap regions, where the magnetic field becomes less uniform and particle rate are higher compared to the barrel, cathode strip chambers are used. A total of 468 strip chambers cover the range up to $|\eta| < 2.4$. These detectors consist of anode wires crossed by orthogonal cathode strips, which enables accurate position and timing measurements.

Complementing the drift and strip chambers are resistive plate chambers, which are deployed in both the barrel and endcap regions, up to $|\eta| < 1.6$. They consist of two parallel resistive plates separated by a gas-filled gap. When a charged particle passes through, it ionizes the gas, initiating an avalanche of electrons that induces a signal on the readout strips. Due to their fast response of ≈ 1 ns, significantly shorter than the 25 ns interval between the LHC bunch crossings, they play an important role in the CMS trigger system.

3.1.6. Trigger and Data Acquisition

During LHC Run 2, the accelerator operated with a bunch crossing frequency of 40 MHz, corresponding to 40 million pp collisions per second. However, the CMS detector's data acquisition and storage systems are only capable of processing and recording events at a maximum rate of approximately 1 kHz [50]. Moreover, only a tiny fraction of these collisions contains events relevant for physics analyses. To manage this disparity and isolate potentially interesting events, CMS utilizes a two-level trigger system that progressively reduces the data rate.

The first level, known as the Level-1 (L1) trigger [51], is implemented in hardware using field-programmable gate arrays (FPGAs). It is responsible for the initial event selection, operating in real time with extremely low latency of around 4 µs. The L1 trigger is composed of two independent subsystems: one that processes calorimeter data to reconstruct candidates for electrons, photons, jets, and hadronic tau decays, and another that analyzes muon system data to identify muon candidates. These subsystems work in parallel, and their outputs are combined to determine whether a given event meets the criteria to be read out in full. The L1 trigger reduces the input event rate by a factor of approximately 400, down to about 100 kHz—the highest rate at which complete detector data can be transferred for further analysis.

The second stage of the trigger system is the High-Level Trigger (HLT), which runs in software on a large farm of servers located near the detector. It applies a streamlined, speed-optimized version of the full event reconstruction algorithm, as used offline. The HLT is organized into sequences of processing modules that reconstruct physics objects—such as leptons, jets, and missing transverse momentum ($\vec{p}_{\mathrm{T}}^{\,\mathrm{miss}}$)—and apply selection criteria based on those objects. To minimize computation time, fast preselection steps based on coarse quantities like localized calorimeter energy deposits are performed before executing more computationally expensive algorithms such as track reconstruction.

The HLT further reduces the event rate from 100 kHz to about 1 kHz. Events that pass any of the predefined HLT paths are forwarded to the offline reconstruction system, where the full event reconstruction is carried out, and the resulting data is stored for later analysis.

3.2. Event Reconstruction

Particle Flow Algorithm

In pp collisions at the LHC, a wide variety of particles are produced, including charged and neutral hadrons, leptons, and photons. These particles interact with multiple subsystems of the CMS detector and often leave signals in more than one detector layer. To exploit this complementary information and improve the overall reconstruction accuracy, CMS employs the Particle Flow (PF) algorithm [52]. It aims to identify and reconstruct each individual particle combining data from all relevant subdetectors, leading to a global and consistent interpretation of the event.

The algorithm starts by forming basic reconstruction units known as PF elements. These include charged particle tracks reconstructed from the inner tracking system and muon detectors, as well as energy clusters identified in the ECAL and HCAL. Tracks are extrapolated outwards and matched to calorimeter clusters within a defined angular distance in the $\eta - \phi$ plane. If multiple associations are found, only the match with the smallest spatial distance is retained to minimize ambiguities. Further linking accounts for photon emission via bremsstrahlung, which can produce ECAL clusters or lead to secondary electron-positron track pairs. Such links are formed if the tangents to a charged particle's trajectory through the traversed tracker layers are consistent with the location or momentum of these clusters or tracks.

Additional connections are made between ECAL and HCAL clusters, particularly in cases where the spatial footprint of an ECAL cluster lies within the extent of a nearby HCAL cluster. Once all links are established, PF blocks are formed, as groups of connected PF elements, which are used to sequentially reconstruct the final-state particles. This process begins with muons and electrons, followed by isolated photons, and finally by hadrons and their nearby electromagnetic energy deposits.

To ensure accurate event interpretation, CMS also applies pileup (PU) mitigation strategies within the PF framework [53]. PU, the presence of multiple overlapping collisions in a single bunch crossing, can contaminate the reconstructed particle collection. Charged hadrons originating from additional vertices are removed, reducing their impact on quantities such as jet energy, lepton isolation, and $\vec{p}_{\mathrm{T}}^{\,\mathrm{miss}}$. However, PU effects are more challenging to correct for neutral particles, which leave no tracks and cannot be directly associated with a specific vertex.

Muons

Muon reconstruction in CMS [54] is handled slightly differently from other particles due to the unique capabilities of the dedicated muon detection system. While the PF algorithm includes muons in its final particle list, their initial reconstruction is performed separately to take advantage of the muon system's extensive coverage and high purity. Most other particles are absorbed by the calorimeters before reaching the muon detectors, making muons relatively easy to isolate. Only neutrinos and, rarely, hadrons escape to the muon system, which helps maintaining a reconstruction efficiency of about 99 %.

CMS reconstructs three types of muon candidates: standalone muons, global muons, and tracker muons. Standalone muons are built using only information from the muon system—namely hits in the drift tubes, cathode strip chambers, or resistive plate chambers. These hits are assembled into track segments and fitted to form a standalone track. However, this method provides lower momentum resolution and is more susceptible to backgrounds like cosmic muons. Global muons are formed by matching a standalone muon track to a track reconstructed in the inner tracker. The hits from both subsystems are combined in a global fit, yielding a significant improvement in momentum resolution, particularly for high-p_T muons. Tracker muons, on the other hand, are reconstructed by extrapolating tracks from the inner tracker to the muon system. If these tracks are compatible with at least one hit or segment in the muon detectors, they are classified as tracker muons. This approach is more efficient for low-p_T muons but more prone to mis-identification due to hadronic activity in the outer detector regions.

Once the muon candidates are reconstructed, they are passed to the PF algorithm, which applies additional selection criteria to identify high-quality PF muons. These candidates are required to be isolated, which helps distinguish genuine prompt muons from those originating from hadron decays. Isolation is computed using reconstructed PF candidates within a cone of radius $\Delta R = 0.4$ around the muon candidate. For charged particles, contributions to the isolation can be directly associated with the PV. Neutral particles—such as photons and neutral hadrons—are also included but cannot be linked to a specific vertex. Therefore, an estimated contribution of neutral particles from PU is subtracted. The combined relative isolation is defined as

$$I_{\text{rel}} = \frac{1}{p_{\text{T}}^{\mu}} \left[I_{\text{ch}} + \max\left(I_{\text{n}} + I_{\gamma} - I_{\text{PU}},\, 0 \right) \right], \tag{3.4}$$

where, p_{T}^{μ} is the p_T of the muon candidate, I_{ch} is the sum of transverse momenta of charged hadrons from the PV, I_{n} and I_{γ} are the contributions from neutral hadrons and photons, respectively, and $I_{\text{PU}} = \frac{1}{2} \sum p_{\text{T}}^{\text{ch, PU}}$, estimates the PU contribution from charged hadrons. Based on this definition, loose and tight WPs are defined by thresholds of 0.25 and 0.15, respectively, where a smaller value means a more isolated particle. This leads to a selection efficiency of approximately 98 % for the loose and 95 % for the tight working point (WP).

For the identification of muons, additional variables like the number of hits in the inner tracker or the goodness-of-fit (GoF) of the global muon track are used to set a score between zero and one defining the quality of the muon candidate. For this thesis muons passing the medium WP are used, corresponding to a score of 0.303 for global muons and an efficiency of 99 % in $Z \rightarrow \mu\mu$ decays.

Electrons

Electrons in the CMS detector [55] are reconstructed as part of the PF algorithm by combining information from the inner tracking system and the ECAL. As electrons pass through the tracker material, they are prone to bremsstrahlung, emitting photons that may further convert into electron-positron pairs. These interactions give rise to electromagnetic showers, which deposit energy primarily in the ECAL. To capture the full energy of the

initial electron, including that carried by associated photons, clusters of ECAL energy deposits are merged into extended superclusters. Because the electron is bent by the magnetic field while the emitted photons propagate roughly along the tangent, the energy from a single electron is dispersed predominantly along ϕ in the ECAL.

The electron track reconstruction relies on a specialized fitting method known as the Gaussian-Sum Filter (GSF) [56], which is optimized to model the energy losses of electron trajectories. Two seeding strategies are employed: an ECAL-based method for high-p_T electrons that starts from ECAL clusters and matches them to tracker hits, and a tracker-based method for lower-p_T electrons or those inside jets, which propagates existing tracks toward the ECAL. Both approaches improve the efficiency of electron reconstruction across a wide phase space. The final energy of each reconstructed electron is obtained by combining the momentum from the GSF track and the calibrated supercluster energy using a weighted average.

Since ECAL superclusters can suffer from energy losses due to shower leakage, dead crystals, or material interactions in the tracker, an additional energy correction is applied. This correction is determined by a multivariate regression based on boosted decision trees (BDTs), trained on simulation, to estimate the ratio of true to reconstructed energy. The correction is performed in three steps: first correcting the supercluster energy, then improving its resolution, and finally combining the energy information with that from the GSF track. Residual differences between simulation and real data are accounted for by calibrating against the invariant mass peak of $Z \rightarrow ee$ events, extracting a scale correction, and applying an energy smearing to match the resolution observed in data.

Electron identification further distinguishes genuine electrons from hadronic fakes, photon conversions, and decay products of heavy-flavor hadrons. Two algorithms are used: a cut-based selection applying fixed thresholds on shower shape, track-supercluster matching, isolation, and conversion rejection criteria; and a multivariate (MVA) approach using BDTs trained on extended input variables including track quality and energy-matching features. While the MVA method omits isolation variables, additional isolation requirements are imposed externally. Electron isolation is computed in a cone of $\Delta R = 0.3$ with contributions from PU estimated differently compared to the muon isolation. For the electron isolation the effective area method is used, with $I_{PU} = \rho \cdot A_{eff}$. Here, ρ is the median transverse energy density and A_{eff} is the area defined by the isolation cone and the $\eta - \phi$ plane it covers. The resulting isolation helps suppress background from non-prompt electrons while retaining high selection efficiencies. Throughout this thesis, electron candidates identified with the MVA method and a WP with 90 % efficiency for $Z \rightarrow ee$ events are used.

Hadronic Jets

Hadronic jets are collimated sprays of particles arising from the fragmentation and hadronization of high-p_T quarks and gluons. Because of color confinement, the partons are not observed directly but as clusters of stable particles in the detector. In the CMS detector, they appear as clustered energy deposits in the ECAL and HCAL, associated with several particle tracks. The reconstruction is performed by clustering PF candidates using the anti-k_T algorithm [57]. Throughout the thesis jets with a radius parameter of

$R = 0.4$ are used. PU complicates the reconstruction by adding extra particles throughout the event. To reduce the impact of PU, charged hadrons that originate from vertices other than the PV are excluded from the clustering process [52]. Within the tracker coverage ($|\eta| < 2.5$), the calorimetric energy deposits of hadrons are primarily in the HCAL, as only a small portion of their energy is deposited in the ECAL. HCAL clusters without track associations are interpreted as neutral hadrons, while those linked to tracks are assigned as charged hadrons. To ensure accurate jet energy measurements, a multi-step calibration is applied. This includes corrections on the jet energy scale and resolution binned in jet p_T and η for PU effects, detector response differences in data and simulation, and adjustments based on momentum balance in di-jet or Z/γ + jet events [58]. These calibrations help improve both the resolution and accuracy of the reconstructed jets.

Hadronically Decaying τ leptons

Hadronic decays of τ leptons play a crucial role in many analyses at CMS. With a short lifetime of about $2.9 \cdot 10^{-13}$ s [59], τ leptons decay before reaching the detector. Due to their mass of 1.78 GeV [59], they are the only leptons that can decay hadronically, with approximately 65 % of all decays producing narrow, low-multiplicity jets (τ_h) composed of charged hadrons and neutral pions. These signatures are challenging to distinguish from the abundant jets initiated by quarks and gluons. The hadrons-plus-strips (HPS) algorithm [60] is used to reconstruct τ_h candidates from anti-k_T clustered jets. It starts by identifying charged hadrons associated with the PV (with $p_T > 0.5$ GeV) and builds strips from nearby photons and electrons to capture energy from neutral pion decays. Strips are constructed within a dynamic $\Delta\eta \times \Delta\phi$ window that scales with the p_T of the constituents. Valid τ_h candidates must have a total charge of ±1 and fall within a signal cone of radius $R_{sig} = \frac{3\,\text{GeV}}{p_T}$, bounded between 0.05 and 0.1. From all possible decay mode hypotheses, the one with the highest p_T is selected. The decay modes and corresponding branching fractions $\mathcal{B}$ are given in Table 3.1.

To suppress backgrounds from jets initiated by quarks and gluons and misidentified electrons and muons, CMS employs the DeepTau algorithm—a convolutional NN trained on both low-level detector features and high-level tau candidate variables [61]. DeepTau outputs a probability p_α for each candidate to be a true τ_h or to originate from an electron, muon, or quark or gluon induced jet. These outputs are combined into discriminants:

$$D_\alpha = \frac{p_{\tau_h}}{p_{\tau_h} + p_\alpha},\ \alpha \in \{\text{jet}, \text{e}, \mu\}. \tag{3.5}$$

WPs of these discriminants are defined based on expected efficiencies or misidentification rates. For example, a medium WP for D_{jet} corresponds to a 70 % efficiency with ≈1 % misidentification rate from jets initiated by quarks and gluons, evaluated with an $H \to \tau\tau$ event sample with $p_T(\tau_h) \in [30, 70]$ GeV.

Missing Transverse Momentum

Since neutrinos do not interact with the detector material, they escape undetected and leave no direct signal. However, their presence in an event can be inferred from an

Table 3.1.: τ lepton decay channels and corresponding $\mathcal{B}$s which are the same for τ leptons and antileptons.

Decay Mode	$\mathcal{B}$ (%)
$e\nu_e\nu_\tau$	17.8
$\mu\nu_\mu\nu_\tau$	17.4
Leptonic	35.2
$h^\pm\nu_\tau$	11.5
$h^\pm\pi^0\nu_\tau$	25.9
$h^\pm\pi^0\pi^0\nu_\tau$	9.5
$h^\pm h^+ h^-\nu_\tau$	9.8
$h^\pm h^+ h^-\pi^0\nu_\tau$	4.8
Other	3.3
Hadronic	64.8

imbalance in the visible momentum in the transverse plane. This is possible because the initial protons and their constituents have negligible p_T, so the total p_T of all final-state particles is expected to be zero as well. Any deviation from this balance indicates the presence of undetected particles, such as neutrinos. The imbalance is quantified using the $\vec{p}_T^{\,\text{miss}}$. It is defined as the negative sum of $\vec{p}_T$ of all reconstructed particles N:

$$\vec{p}_T^{\,\text{miss}} = -\sum_{i=1}^{N} \vec{p}_{T,i} \quad \text{and} \quad p_T^{\text{miss}} = \left|\vec{p}_T^{\,\text{miss}}\right|. \tag{3.6}$$

The accuracy of the p_T^{miss} measurement depends strongly on the quality of the reconstructed particles entering the sum. In particular, additional soft particles from PU interactions can degrade the resolution. To mitigate these effects, the PileUp Per Particle ID (PUPPI) algorithm [53, 62] assigns a weight w_i to each particle based on the likelihood of it to originate from the PV. This weight can be used to compute a PU-suppressed version of $\vec{p}_T^{\,\text{miss}}$:

$$\vec{p}_T^{\,\text{miss}} = -\sum_{i=1}^{N} w_i \cdot \vec{p}_{T,i}.$$

Using PUPPI weights improves the resolution of the p_T^{miss} measurement and leads to better agreement with the true missing momentum, especially in high PU environments.

B Quark Induced Jets

The identification of jets induced by b quarks (b jets) exploits differences between jets from b quarks and those from light quarks or gluons. These differences arise from the decay behavior of b hadrons and their unique fragmentation and hadronization patterns. Hadrons with b quarks have a mean lifetime of about $\sim 10^{-12}$ s [59] and therefore can travel up to a few mm in the rest frame before decaying. This often creates a displaced secondary vertex with additional tracks [63]. The high mass and hard fragmentation of b hadrons

lead to decay products with higher p_T relative to the jet axis. In about 20 % of cases, b hadrons decay with a charged lepton in the final state, producing non-isolated leptons inside the jet. The DeepJet algorithm [64] is used to separate b jets from light quark or gluon induced jets. It takes as input up to 25 charged and 25 neutral PF candidates per jet, along with up to four secondary vertices as well as global jet and event properties.

4. Towards the WH Cross Section and Charge Asymmetry Measurements

The analysis presented in this thesis aims to measure the inclusive production cross section of a Higgs boson in association with a W boson ($\sigma(\mathrm{WH})$), the individual cross sections $\sigma(\mathrm{W^+H})$ and $\sigma(\mathrm{W^-H})$, and the charge asymmetry A, defined in Equation 2.13. This work provides the first-ever measurements of $\sigma(\mathrm{W^+H})$, $\sigma(\mathrm{W^-H})$, and A. Crucially, A is sensitive to the light-quark Yukawa couplings, providing a novel probe of H–quark interactions. While the Higgs boson is expected to decay into a pair of τ leptons the W boson is required to decay into an electron or a muon and corresponding neutrino. This analysis was performed and published within the CMS Collaboration [65] and includes the dataset collected by the CMS experiment during the LHC Run 2 period, divided into four run periods during the years 2016 to 2018, corresponding to a total integrated luminosity of 138 fb^{-1} [66–68]. This chapter outlines the main steps of the analysis: the selection of events targeting $\mathrm{WH}(\tau\tau)$ production, the estimation of background contributions from other processes, the strategy used to extract the signal, and the results of the measurements.

4.1. Event Selection

As discussed in Section 3.2, a τ lepton can decay into an electron, a muon or hadronically. The possible final states for a $\tau\tau$ pair are sketched in Figure 4.1. All of these decays involve neutrinos, which cannot be detected with the CMS detector. Therefore, a significant fraction of the τ energy can not be measured. The same argument holds for the leptonic W boson decays. In total, the final states of the signal process require three objects. Four final states of the WH production are considered: $\mathrm{e}\tau_\mathrm{h}\tau_\mathrm{h}$, $\mu\tau_\mathrm{h}\tau_\mathrm{h}$, $\mathrm{e}\mu\tau_\mathrm{h}/\mu\mathrm{e}\tau_\mathrm{h}$, and $\mu\mu\tau_\mathrm{h}$, where the first object in this notation is the W boson decay product and the latter two objects are associated with the $\mathrm{H} \rightarrow \tau\tau$ decay. Before the statistical inference of the signal these final states are combined to an $\ell\ell\tau_\mathrm{h}$ ($\ell = \mathrm{e}, \mu$; light lepton) and an $\ell\tau_\mathrm{h}\tau_\mathrm{h}$ final state. In the $\ell\ell\tau_\mathrm{h}$ final states, the light lepton leading in p_T is considered to belong to the W boson decay, which is correct in more than 75% of the cases according to on generator level studies [69]. This is expected as the light lepton from the Higgs boson decay chain shares the energy with a second τ lepton and two neutrinos. The light lepton from the W boson shares the energy only with one more neutrino. In the $\ell\tau_\mathrm{h}\tau_\mathrm{h}$ final states the light lepton is associated with the W boson decay. These final states have the highest impact on the parameters of interest (POIs): A, $\sigma(\mathrm{WH})$, $\sigma(\mathrm{W^-H})$, and $\sigma(\mathrm{W^+H})$. All other possible final states are neglected.

By the HLT, events are selected based on an isolated, high-p_T light lepton. For the $\mathrm{e}\tau_\mathrm{h}\tau_\mathrm{h}$ final state single electron triggers are used, while for the $\mu\mu\tau_\mathrm{h}$ and $\mu\tau_\mathrm{h}\tau_\mathrm{h}$ final states

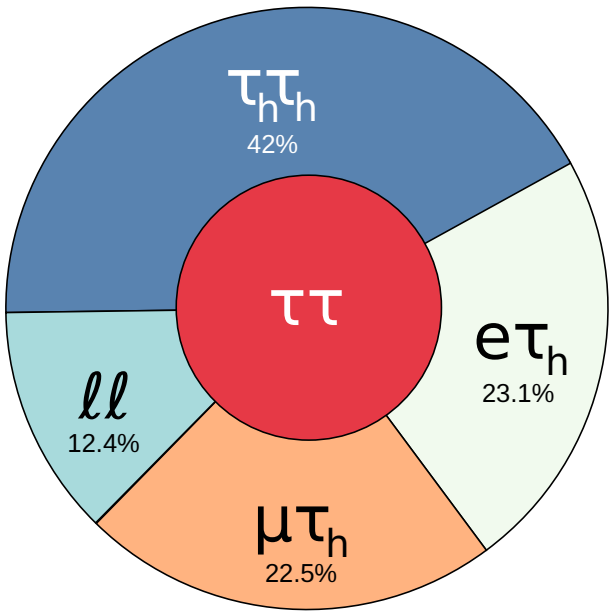

Figure 4.1.: Branching fractions of $\tau\tau$ decays. For the analysis only decays with at least one τ_h are considered covering 87 % of the final states.

single muon triggers are used. In the $e\mu\tau_h/\mu e\tau_h$ final state, the light lepton with the higher p_T is considered as the triggering object, associated with the corresponding single light lepton trigger. To ensure offline selections tighter than the trigger thresholds, minimum p_T values are applied. For electrons, the thresholds are 26 GeV (2016), 28 GeV (2017), and 33 GeV (2018). For muons, they are 23 GeV, 25 GeV, and 25 GeV, respectively. During parts of 2016, some triggers also required $|\eta| < 2.1$ for the triggering electron and muon. Unless restricted by trigger conditions, electrons (muons) must have $p_T > 15\,(15)$ GeV and $|\eta| < 2.5(2.4)$. For the τ_h candidates it holds $p_T > 20$ GeV and $|\eta| < 2.3$. In order to obtain resolved and isolated objects, electrons and muons must be separated by $\Delta R(e, \mu) > 0.3$. Any light lepton and τ_h candidates must be separated by $\Delta R(\ell, \tau_h) > 0.5$ after the selection. In di-τ_h final states, the two τ_h candidates must also satisfy $\Delta R(\tau_h, \tau_h) > 0.5$. The selection requirements for the objects in each final state are summarized in Table 4.1. All objects are required to have a distance of $\Delta R > 0.5$ from any jet in the event. Events with b jets are vetoed to suppress the background from tt production. Furthermore, events with additional light leptons passing the requirements given in Table 4.1 are vetoed to suppress backgrounds with two or three vector bosons. Charge requirements are applied to suppress backgrounds and increase the purity with respect to the signal process. In the di-ℓ final states, the two light leptons must have the same charge, and the τ_h must have opposite charge to result in the neutral charge for the Higgs boson decay. This reduces backgrounds with prompt light leptons, like Drell–Yan, by three orders of magnitude in the $\mu\mu\tau_h$ and by a factor of five in the $e\mu\tau_h/\mu e\tau_h$ final state. Because they originate from the Higgs boson decay the two τ_h candidates must have opposite charges in the di-τ_h final states.

Table 4.1.: Selection criteria for the objects of the final states of the analysis. The p_T cuts are given for the triggering light lepton for 2016, 2017 and 2018. In parentheses the p_T threshold for the non-triggering light lepton is given. D_α corresponds to the DeepTau WP against $\alpha \in \{\text{jet}, \text{e}, \mu\}$ for the τ_h candidate.

Final state	Object	p_T (GeV)	$\lvert\eta\rvert$	D_α / I_{rel}
$\mu\mu\tau_h$	muon	$> 23, 25, 25(15)$	$< 2.4^\dagger$	< 0.15
	τ_h	> 20	< 2.3	Medium
$e\mu\tau_h$	electron	$> 26, 28, 33(15)$	$< 2.5^\dagger$	< 0.15
	muon	$> 23, 25, 25(15)$	$< 2.4^\dagger$	< 0.15
	τ_h	> 20	< 2.3	Medium
$e\tau_h\tau_h$	electron	$> 26, 28, 33$	$< 2.5^\dagger$	< 0.15
	τ_h	> 20	< 2.3	Medium
$\mu\tau_h\tau_h$	muon	$> 23, 25, 25$	$< 2.4^\dagger$	< 0.15
	τ_h	> 20	< 2.3	Medium

† 2.1 for the triggering lepton for some trigger paths in 2016.

If more than one possible di-τ pair is present after the requirements listed above, the τ_h candidates with the highest scores of DeepTau against jets are chosen.

4.2. Background and Signal Model

Although the event selection described in Section 4.1 targets events from the signal processes, background processes are selected as well. In order to estimate the cross section of the signal process, the description of the background processes and its corresponding uncertainties must be estimated as accurate as possible. The individual background processes are introduced below. Based on their modeling, two background classes are formed. The first class includes events in which a light lepton or a τ_h does not originate from a genuine particle of the targeted final state but instead arises from a misidentified jet. These backgrounds are referred to as reducible backgrounds and mainly originate from Drell–Yan, W+jets and tt production processes. Smaller contributions come from events with two vector bosons with hadronic decays. As Higgs boson production via ggF or VBF contributes only when a jet is misidentified as one of the required objects these processes are considered as reducible backgrounds as well. All reducible backgrounds are estimated using data, as explained in Section 4.2.1.

Irreducible backgrounds arise from processes that produce the same final state particles as the signal and therefore cannot be suppressed by object identification. The dominant process in this category is WZ production. Smaller contributions come from ZZ, VVV production, and W/Z bosons produced in association with tt. These backgrounds are estimated using simulation, as described in Section 4.2.2. The signal processes are described via simulation as well. Both the WH($\tau\tau$) and WH(WW) processes are considered as signal. Although this analysis targets WH($\tau\tau$), WH(WW) is included in the signal model to be able to combine this analysis with an anticipated, dedicated WH(WW) analysis.

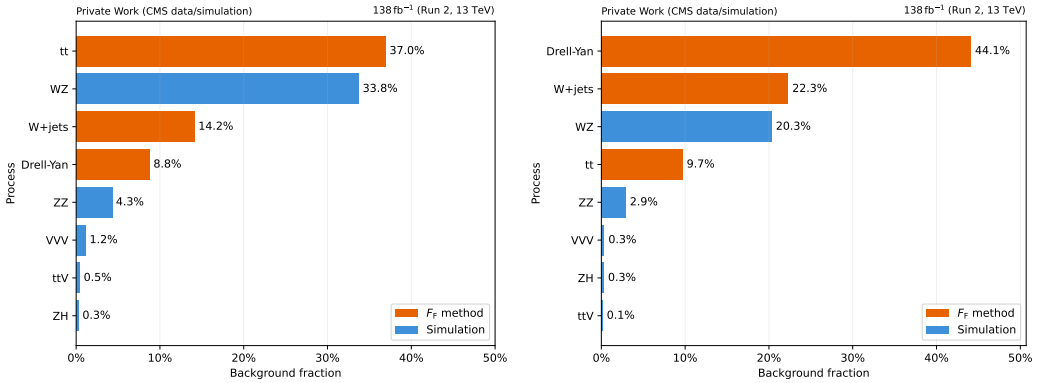

Figure 4.2.: Fraction of background processes after the event selection in the $\ell\ell\tau_h$ final state (left) and $\ell\tau_h\tau_h$ final state (right) integrated over the Run 2 dataset. In colors the corresponding estimation method is drawn.

In the following the physics of the background processes and their impact on the analysis are introduced. The background processes included are

- Z boson production in association with jets (Drell–Yan),
- Top quark pair production (tt),
- W boson production in association with jets (W+jets),
- Diboson (WZ, ZZ) production (VV),
- Triboson (WWZ, WWW, ZZZ, ZZW) production (VVV),
- Higgs boson production in association with a Z boson (ZH),
- tt in association with a vector boson (ttV).

The relative contribution of each background process to the event selection integrated over the Run 2 dataset and split by the $\ell\ell\tau_h$ and $\ell\tau_h\tau_h$ final states is shown in Figure 4.2. In the $\ell\ell\tau_h$ final state the major background sources originate from tt and WZ processes, while in the $\ell\tau_h\tau_h$ final state the major background process is Drell–Yan followed by W+jets and WZ.

Top quark pair production

At $\sqrt{s} = 13$ TeV tt production has an inclusive cross section of about 830 pb [70]. In Figure 4.3 the leading order Feynman diagrams of the tt process are shown. Each top quark decays almost exclusively via t→bW, while other decay modes are suppressed by the Cabibbo–Kobayashi–Maskawa matrix encoding the quark-flavor mixing. For this analysis, mainly the leptonic decays of the W boson are relevant. With two leptons from the W bosons the third object in the event selection must be faked by a jet. With 37 %, this process has the highest contribution to the total background in the $\ell\ell\tau_h$ final state. In the $\ell\tau_h\tau_h$ final state, the contribution is 9.7 %. To pass the selection in both final states, the charge

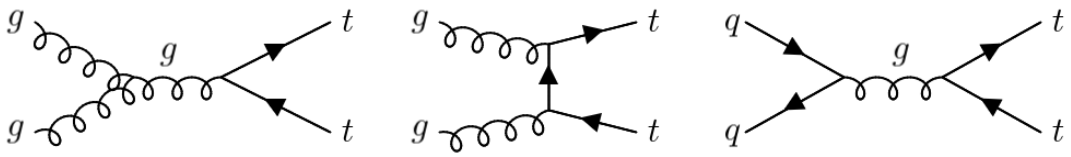

Figure 4.3.: Leading-order Feynman diagrams for tt production in pp collisions. The dominant mechanism is gluon fusion (left and middle); quark–antiquark annihilation (right) also contributes.

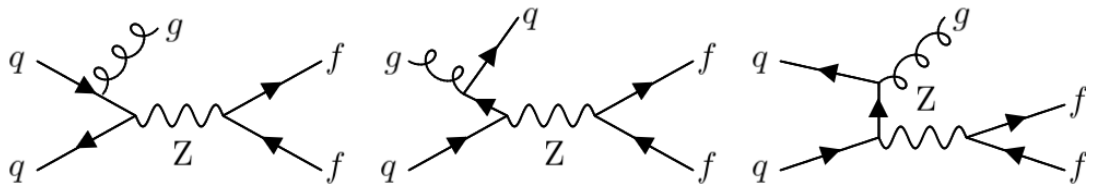

Figure 4.4.: In Drell–Yan, the Z boson originates predominantly from qq annihilation and decays into fermion (f) pairs. In this analysis, only the leptonic decays of the Z boson are relevant. Extra jets in the event are generated by initial- or final-state quark/gluon radiation.

requirements must be satisfied. In tt events, the prompt light leptons and τ_h from the two W bosons typically mimic the Higgs boson decay products, while the third object is a misidentified jet (often b jet, but light-flavor jets also contribute). Alternatively, the selection can be met via charge misidentification.

Drell–Yan production

At $\sqrt{s} = 13\,\text{TeV}$ Drell–Yan production has an inclusive cross section of about 2000 pb. Representative leading order diagrams are shown in Figure 4.4. This process has the highest contribution in the $\ell\tau_h\tau_h$ final state with 44 %. Here, Drell–Yan enters the event selection if the Z boson decays into $\ell\tau_h$ and the τ_h with the same charge as the light lepton is faked by a jet. This process is strongly suppressed in the $\ell\ell\tau_h$ final state due to the same charge requirement on the two light leptons. Via semi-leptonic $\tau\tau$ decays and a jet misidentified as a light lepton this process has a contribution of 8.8 % to the total background in this final state.

VV production

Although the VV cross sections are only at the few-pb level, VV remains a significant background because its event topology closely matches the signal. This is especially true for WZ($\tau\tau$), which yields the same final state signature. Discrimination relies primarily on the mass difference, which induces shifts in the τ lepton pair kinematics. Its contribution to the total background is 33.8 % in the $\ell\ell\tau_h$ and 20.3 % in the $\ell\tau_h\tau_h$ final states. Feynamn diagrams of VV production are displayed in Figure 4.5.

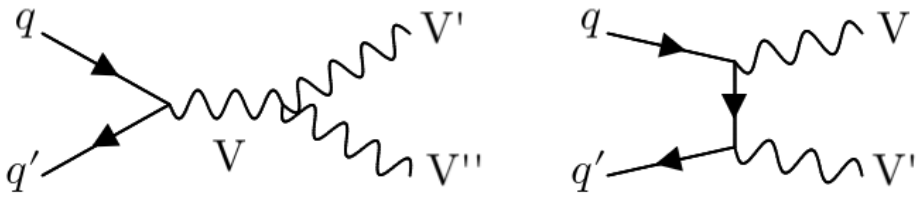

Figure 4.5.: Representative leading-order Feynman diagrams for VV production. Left: *s*-channel topology; right: *t*-channel topology (via quark exchange). This process is irreducible as it shares the same objects as the signal process in the final states. This holds especially for WZ, which has a very similar topology as WH.

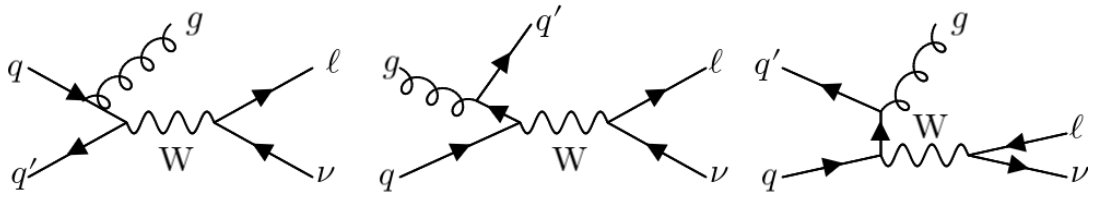

Figure 4.6.: Representative Feynman diagrams for W+jets production. The W boson is produced predominantly via qq' annihilation. Like in Drell–Yan, only the leptonic decays of the W boson are relevant for this analysis. One or more additional jets arise from initial- or final-state QCD radiation.

W+jets production

W+jets production has similar topology and kinematic properties compared to Drell–Yan. Representative leading-order Feynman diagrams for W+jet production are shown in Figure 4.6. Only the W$\rightarrow \ell\nu$ decay is relevant for this analysis. Because such events contain only a single prompt lepton, the selection suppresses W+jets production. Contributions occur when two jets are misidentified as light lepton or τ_h.

4.2.1. Estimation of Reducible Backgrounds

Events selected in the analysis region defined in section 4.1 may include jets that are misidentified as light lepton or τ_h. These *fake* objects are primarily due to jets in Drell–Yan, tt and W+jet production processes being wrongly identified as τ_h (jet $\rightarrow \tau_h$), electron (jet $\rightarrow$ e), or muon (jet $\rightarrow \mu$). To estimate the contribution from these processes, a data-driven method known as the F_F method is used, as described in [71, 72]. The basic principle of the method is given in Figure 4.7, here as an example for the estimation of the contribution of jet $\rightarrow \tau_h$. In this example, the phase space is divided into four regions that are orthogonal to each another. On the y-axis a cut on the DeepTau against jets WP is introduced that separates the signal and signal-like regions (SR, SR-like) from the application and application-like regions (AR and AR-like). On the x-axis a process-specific selection is splitting the phase space into the SR, AR and SR-like, AR-like, where the

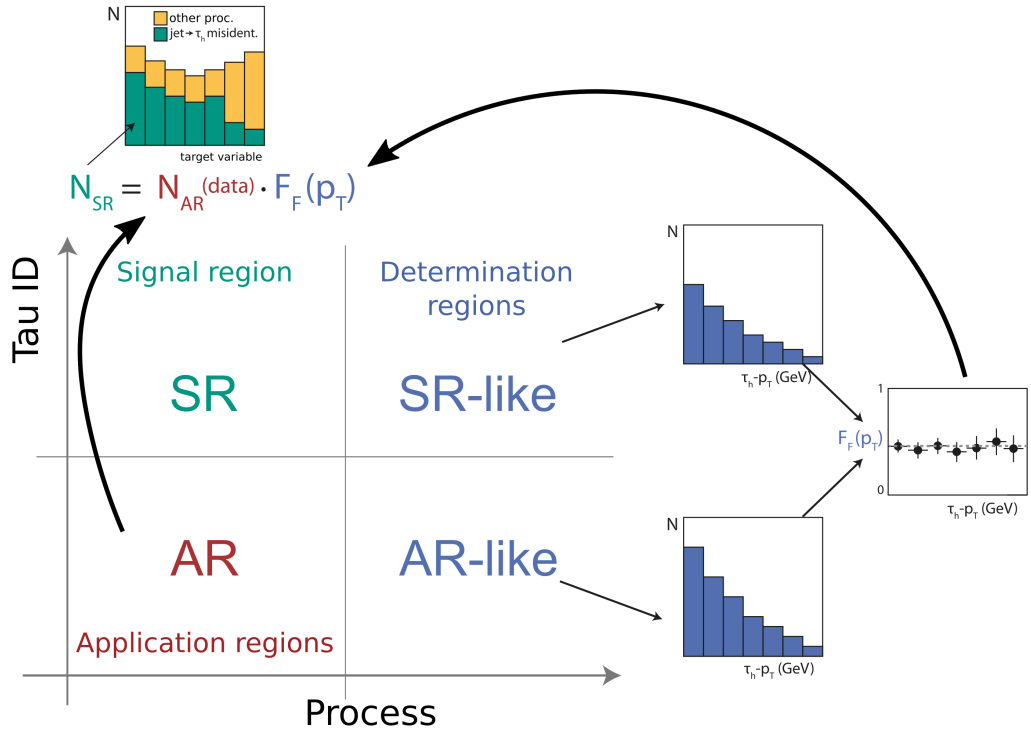

Figure 4.7.: Illustration of the basic principle of the F_F method. In this example the contribution of jet$\rightarrow \tau_h$ is estimated. Adapted from [73].

combined phase space of SR-like and AR-like is called determination region (DR). The SR and SR-like are enriched in real τ_h candidates, the AR and AR-like are enriched in jet$\rightarrow \tau_h$ candidates, and the DR enhances the background process under study. The F_F method estimates the yield and shape of reducible backgrounds by extrapolating from the AR into the SR. Each lepton flavor $i \in \{\tau_h, e, \mu\}$ has its own corresponding DR_i and AR_i. The exact choice of selection for the DR_i depends on the object and is given in detail in Table 4.2. The AR and AR-like are enriched in fake leptons by inverting I_{rel} or loosening identification requirements compared to the SR:

- For jet $\rightarrow \tau_h$, the DeepTau discriminant is inverted to fail the medium WP, while still passing the VVVLoose WP.
- For jet $\rightarrow \ell$, looser I_{rel}, $0.15 < I_{rel} < 0.5$, or ID is required.

These modified criteria are anticipated to keep the kinematic properties of the AR_i similar to the SR but enhance the contribution of fake leptons. A transfer factor, or fake factor F_F^i, is derived to connect the event counts in the AR_i to the expected contributions in the SR. The F_F^i are measured in dedicated Drell–Yan control regions DR_i, each orthogonal to the SR and designed to enrich events with fakeable objects. The F_F^i is defined as:

$$F_F^i = \frac{N^i_{\text{SR-like}}}{N^i_{\text{AR-like}}}. \tag{4.1}$$

Table 4.2.: Summary of selection criteria used to define the DR_i for jet $\rightarrow \tau_h, \mu, e$.

Mis-ID Channel	Selection	Event Selection Cuts
jet $\rightarrow$ e	$\mu\mu$+e	– μ: $p_T > 10$ GeV, $\lvert\eta\rvert < 2.4$, $I_{rel} < 0.15$, medium ID – Leading μ: $p_T > 23, 25$ GeV (2016, 2017/2018) – $\mu\mu$-pair: $\Delta R > 0.3$, opposite charge – e: $p_T > 10$ GeV, $\lvert\eta\rvert < 2.5$, $I_{rel} < 0.5$, loose ID – $\Delta R(e, \mu) > 0.3$ – Event must pass single muon trigger – b jet veto – $m_T(e, \vec{p}_T^{miss}) < 40$ GeV
jet $\rightarrow \mu$	ee+μ	– e: $p_T > 10$ GeV, $\lvert\eta\rvert < 2.5$, $I_{rel} < 0.15$, ID WP90 – Leading e: $p_T > 26, 28, 33$ GeV (2016, 2017, 2018) – μ: $p_T > 10$ GeV, $\lvert\eta\rvert < 2.4$, $I_{rel} < 0.5$, loose ID – ee-pair: $\Delta R > 0.3$, opposite charge – $\Delta R(\mu, e) > 0.3$ – Event must pass single electron trigger – b jet veto – $m_T(\mu, \vec{p}_T^{miss}) < 40$ GeV
jet $\rightarrow \tau_h$	$\mu\mu + \tau_h$	– μ: $p_T > 10$ GeV, $\lvert\eta\rvert < 2.4$, $I_{rel} < 0.15$, medium ID – Leading μ: $p_T > 23, 25$ GeV (2016, 2017/2018) – $\mu\mu$-pair: $\Delta R > 0.3$, opposite charge – τ_h: $p_T > 20$ GeV, $\lvert\eta\rvert < 2.3$, VVVLoose WP – $\Delta R(\mu, \tau_h) > 0.5$ – Event must pass single muon trigger – b jet veto

To reduce the contamination from real leptons in the DR_i, the contributions from genuine leptons, mainly from VV, are estimated using simulation and subtracted before calculating the F_F^i. In the case of jet$\rightarrow \ell$, an additional cut on the transverse mass, $m_T < 40\,\text{GeV}$, is applied to suppress leptons from WZ decays and increase the purity of Drell–Yan and tt. Distributions of m_T in the μμ+e and ee+μ selections are given in Figure 4.8 explanatory for the 2018 run period.

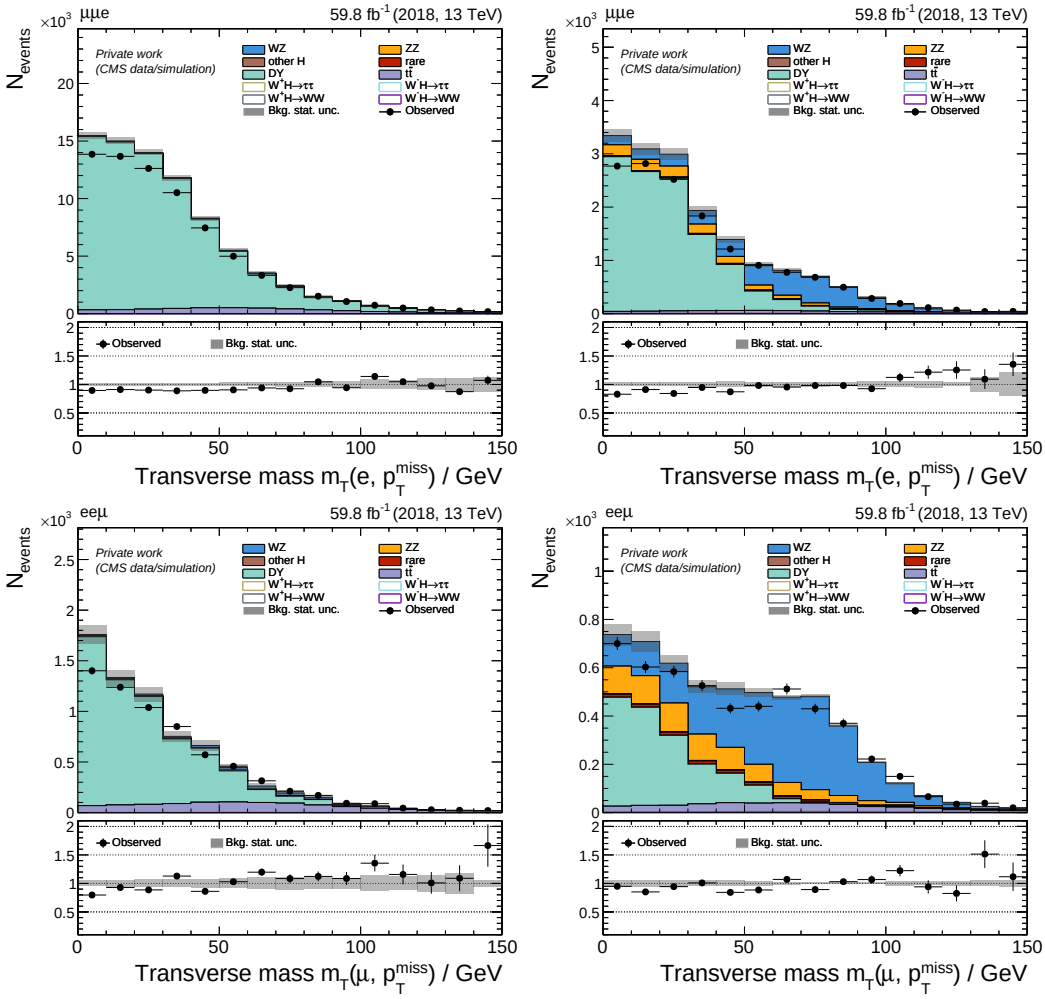

Figure 4.8.: Distributions of $m_T(e, \vec{p}_T^{\,miss})$ (top) and $m_T(\mu, \vec{p}_T^{\,miss})$ (bottom) for events selected in the denominator (left) and numerator (right) of the jet$\rightarrow$ μ/e fake rate measurement, in 2018. To increase the purity of Drell–Yan and tt processes, a cut of $m_T < 40\,\text{GeV}$ is applied. The gray band represents the statistical uncertainty of the simulated processes.

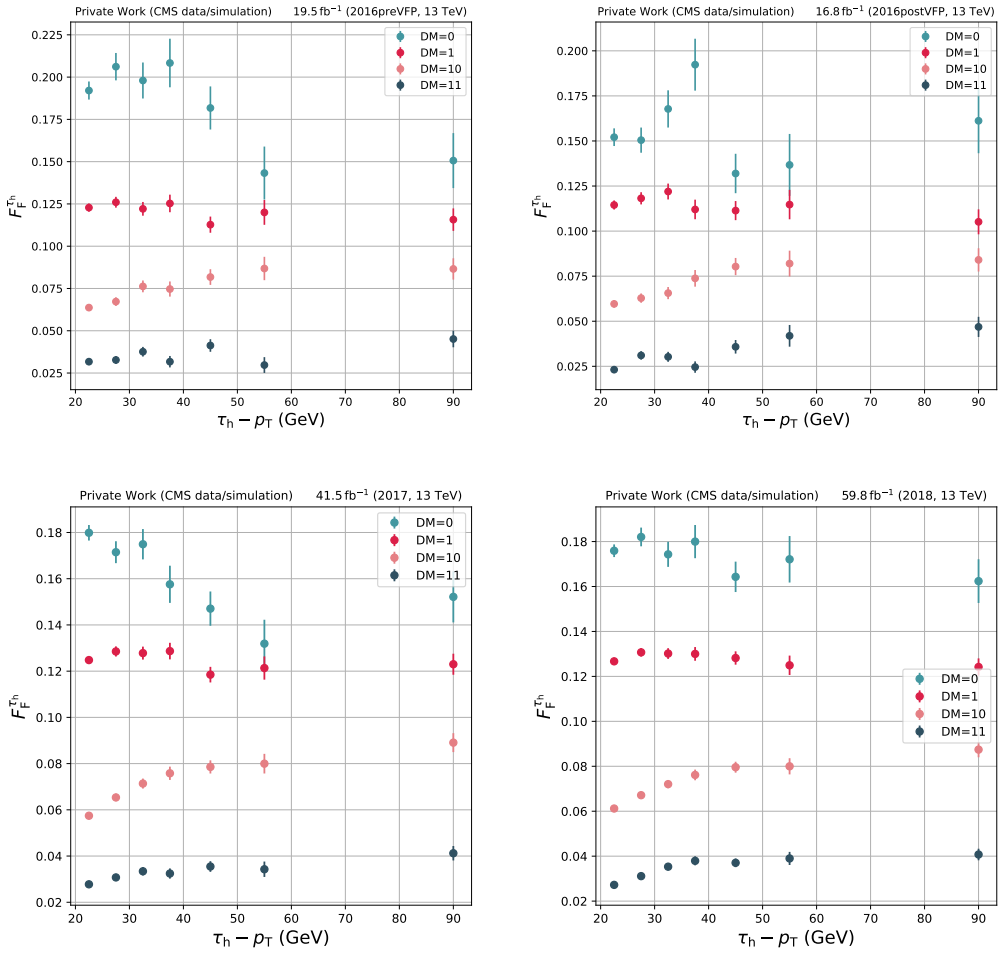

Figure 4.9.: Distributions of $F_F^{\tau_h}$ binned in τ_h p_T and using the medium WP on all DeepTau discriminants for 2016preVFP (top left), 2016postVFP (top right), 2017 (bottom left) and 2018 (bottom right) data.

The F_F^i depend on the following object properties:

- For τ_h: dependence on p_T, decay mode, and DeepTau discriminator scores, D_e and D_μ.
- For e/μ: dependence on p_T.

The distributions of $F_F^{\tau_h}$ are given in Figure 4.9 and of F_F^ℓ in Figure 4.10. Once the F_F^i are known, the expected number of background events in the SR can be calculated. In the $\ell\tau_h\tau_h$ final states, the τ_h, which has the same charge as the light lepton, is always faked by a jet in the case of the reducible backgrounds. Therefore the contribution of jet fakes is estimated by inverting the DeepTau requirement for the same-charge τ_h to define the AR_{τ_h}. Other contributions, e.g., from a faked opposite-charge τ_h, are negligible.

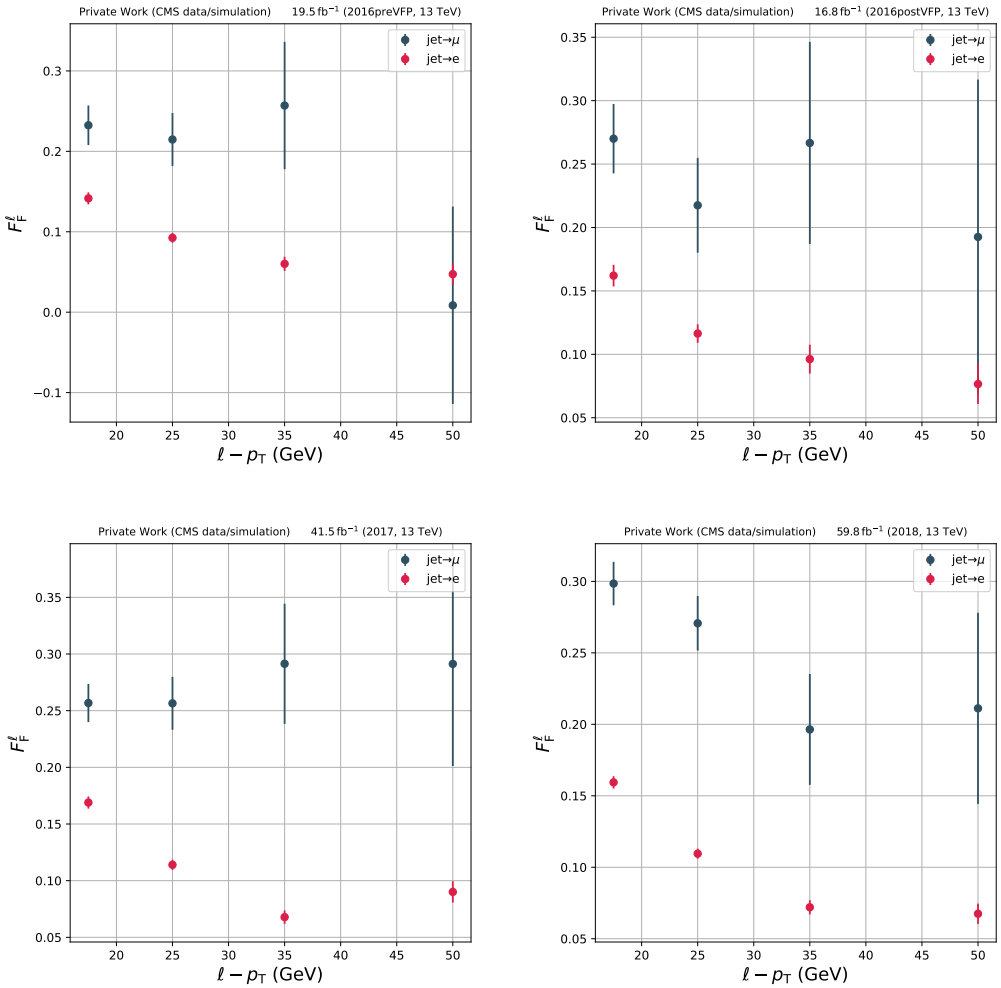

Figure 4.10.: Distributions of F_F^ℓ binned in ℓ-p_T for 2016preVFP (top left), 2016postVFP (top right), 2017 (bottom left) and 2018 (bottom right) data.

In the $\ell\tau_h\tau_h$ final states, the yield and kinematic distributions of events with jet$\rightarrow\tau_h$ are derived from

$$N_{SR} = N_{AR_{\tau_h}} \cdot F_F^{\tau_h}. \tag{4.2}$$

In the $\ell\ell\tau_h$ final states the τ_h, the non-triggering ℓ, or both are considered as objects that can be faked by a jet. Other contributions are negligible. Special care is taken to avoid double counting where both objects pass their AR_i selection, denoted with AR_{ℓ,τ_h}. Double counting may occure since this case is estimated by $F_F^{\tau_h}$ and F_F^ℓ. This overlap is subtracted from the yield by

$$N_{SR} = \sum_{i=\tau_h,\ell} N_{AR_i} F_F^i - N_{AR_{\ell,\tau_h}} F_F^\ell F_F^{\tau_h}. \tag{4.3}$$

A summary sketch of the F_F method adapted to this analysis is given in Figure 4.11. This method allows for a precise estimate of fake backgrounds, using data as much as possible, while simulations are used only for minor corrections and validation.

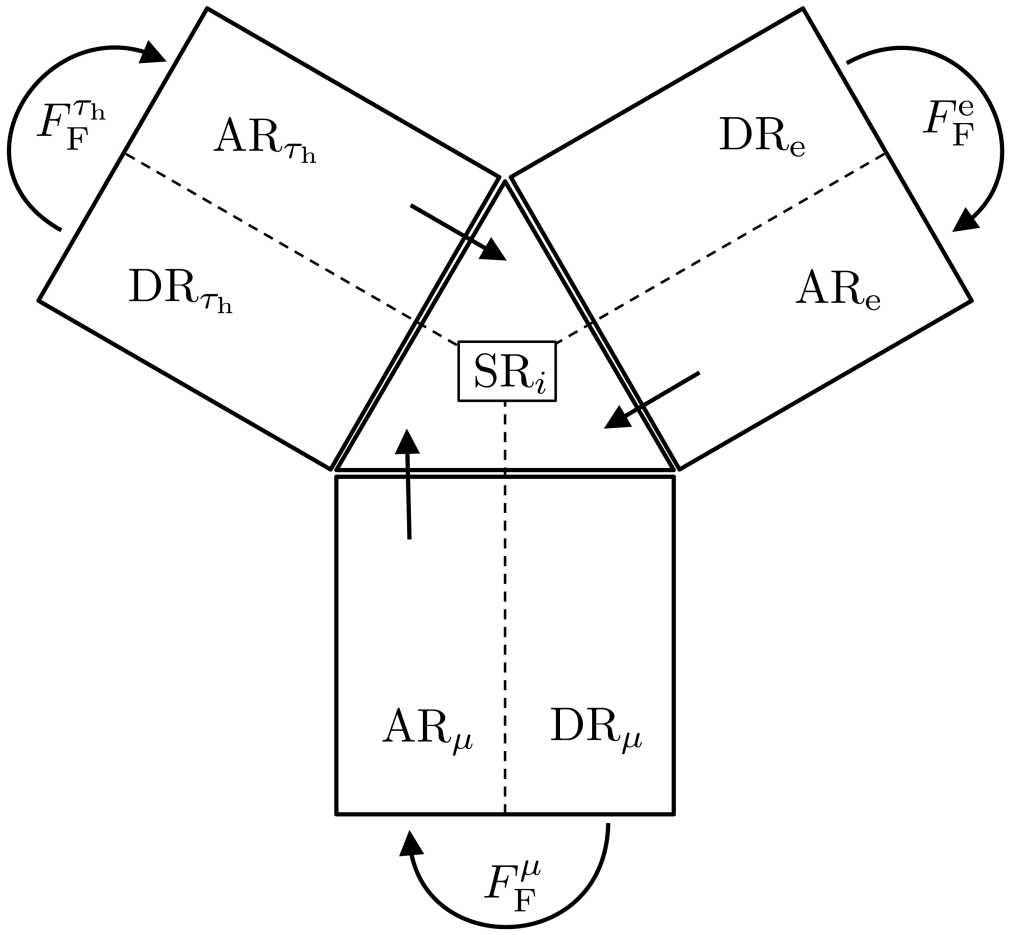

Figure 4.11.: Application of the F_{F} method in this thesis. F_{F}^{i} for jet$\rightarrow \tau_{\mathrm{h}}, \mu, \mathrm{e}$ are calculated in the corresponding DR_i. Event by event the F_{F}^{i} are applied in the AR_i to get the total contribution of jet fakes. Taken from [65].

4.2.2. Estimation of Processes by Simulation

To estimate the irreducible background and signal processes, Monte Carlo simulation is used. It complements the F_{F} method by covering all processes that are not estimated from data. Simulated samples are generated using state-of-the-art tools such as MadGraph5_aMC@NLO [74], POWHEG [75], and PYTHIA 8.2 [76]. The simulation begins with the pp collision. At LHC energies, not the protons as a whole but the individual partons of the protons interact with each other. Since the momentum fractions of the colliding partons are unknown, parton distribution functions (PDFs) are used to estimate the momenta. The NNPDF3.1 [77] set is applied in all simulations throughout this analysis.

The first step in the simulation is the hard scattering process. This defines the main partonic interaction, e.g., a Z boson production or a semileptonic top quark decay. After

Table 4.3.: Monte Carlo event generators used for signal and background simulation.

Process	Event Generator
ggZZ	POWHEG
ttV	POWHEG
VVV	MADGRAPH5_AMC@NLO
WZ	MADGRAPH5_AMC@NLO
ZZ	POWHEG
VH	POWHEG

this, parton showering is simulated using PYTHIA 8.2, modeling additional radiation and softer interactions. As the energy scale drops, hadronization occurs, where partons form hadrons. Underlying event (UE) activity, caused by softer parton interactions, is also simulated using the CP5 tune [78]. Additionally, PU is added to reflect the observed PU profile in data.

Next, the interaction of particles with the CMS detector is simulated using GEANT4 [79]. This includes detailed modeling of the detector geometry and signal response. The simulated detector signals are then reconstructed using the same software as for real data.

Different generators are used depending on the process, which are all simulated at next-to-leading order of perturbative QCD. Table 4.3 summarizes the generators.

Samples involving a Higgs boson are normalized to the cross sections recommended in [43]. An Higgs boson mass of 125 GeV is used in the event generation. For cross section and branching ratio calculations, the value 125.38 GeV [80] is used. The other simulated samples are normalized to the cross sections provided by the cross section database [81].

4.2.3. Corrections to Simulated Events

In order to match simulation to data as closely as possible, several correction factors are applied. These corrections account for known differences in trigger efficiency, object identification, I_{rel}, energy scales, and b-tagging performance.

Pileup Reweighting

The number of PU interactions in data depends on the instantaneous luminosity provided by the LHC. At the time of event generation, this number is typically unknown. To account for it, additional interactions are added randomly using a Poisson distribution, based on the expected number of PU events for the run period. However, the expected and actual pileup distributions often differ. A correction is therefore applied. This correction is derived from the ratio of the measured PU distribution in data to that used in the simulation.

Table 4.4.: Requirements applied on the *tag* muon.

Property	Criteria
Trigger	Single muon trigger
$p_T(\mu)$	$> 25\,\text{GeV}$
ID(μ)	medium
$I_{\text{rel}}(\mu)$	< 0.15

Lepton Reconstruction Efficiencies

In case of electron and muon triggers, identification and I_{rel} efficiencies are corrected using scale factors (SFs):

$$\text{SF} = \frac{\epsilon_{\text{Data}}}{\epsilon_{\text{MC}}}. \tag{4.4}$$

These are derived using the Tag-and-Probe method [82] explained below in $Z\rightarrow \mu\mu/ee$ events and applied as a function of p_T and η. In most cases, they amount to only a few percent. The efficiencies are calculated step by step, with each new measurement applying the corrections from the previous one, starting with the identification:

$$\epsilon(\text{ID}, I_{\text{rel}}, \text{trig}) = \epsilon(\text{trig} \mid I_{\text{rel}}, \text{ID}) \cdot \epsilon(I_{\text{rel}} \mid \text{ID}) \cdot \epsilon(\text{ID}). \tag{4.5}$$

The efficiency for identifying τ_h is corrected by SFs as well via the Tag-and-Probe method. The SFs are measured in an inclusive $\mu\tau_h$ selection, using genuine $Z\rightarrow \mu\tau_h$ events as a signal and the visible invariant mass of the τ lepton pair as an observable. They are provided by CMS and are binned in decay mode or $p_T(\tau_h)$, depending on the $\tau\tau$ final state, and also depend on D_e [60].

The Tag-and-Probe Method

The Tag-and-Probe method exploits the clean $Z \rightarrow \mu\mu$ and $Z \rightarrow ee$ processes, which can be reconstructed with high precision and efficiency. In the following, the efficiency measurement for muon identification using the medium WP is described as an example.

A loose preselection is applied, requiring two muons without any isolation, identification, or trigger criteria. As a baseline, both muon must satisfy $p_T > 7\,\text{GeV}$ and be separated by $\Delta R > 0.5$. To improve the modelling of the Z boson resonance, events containing a reconstructed photon with $p_T > 10\,\text{GeV}$ within $\Delta R = 0.4$ of either muon are vetoed to suppress final state radiation.

After this preselection, Tag-and-Probe pairs are formed. The *tag* muon is required to pass any tight selection criteria (see Table 4.4), ensuring a high probability that it originates from a Z boson decay. The other muon in the event, the *probe*, is assumed to be genuine as well but is not required to pass tight selection criteria. This allows testing whether the identification algorithm correctly recognizes the probe muon. If both muons in an event satisfy the tag criteria, each can be used as a tag or probe, effectively doubling the number of Tag-and-Probe pairs. Pairs are sorted into two regions: *pass*, if the probe muon passes the medium identification WP, and *fail*, if it does not. The efficiency of

the identification algorithm is then extracted from the invariant di-μ mass distributions in both regions. These are fitted simultaneously with a combined model. The Z boson signal peak is described by a Voigtian function (a convolution of a Gaussian resolution and a Breit-Wigner line shape), while the background is parametrized by a product of an exponential function and an error function. The efficiency in each phase space bin i (typically defined in p_T and η of the probe muon) is obtained as

$$\epsilon_i = \frac{N_{\text{pass},i}}{N_{\text{pass},i} + N_{\text{fail},i}}, \tag{4.6}$$

where $N_{\text{pass},i}$ and $N_{\text{fail},i}$ are the extracted signal yields in the pass and fail regions, respectively. These yields are determined from the normalization of the fitted Voigtian functions. The resulting efficiencies capture both kinematic and detector-dependent effects in the muon identification. An example fit to extract the medium identification efficiency for data and simulation is given in Figure 4.12. The SF distribution for the 2018 run period is given in Figure 4.13.

Lepton Energy Scale

The energy scale of genuine τ_h candidates is corrected per decay mode and measured in an inclusive $\mu\tau_h$ control region. The visible mass of the $\mu\tau_h$ system is used as the observable. A maximum likelihood fit is applied to the data and simulated distributions. The τ_h energy scale in the simulation is varied, and the negative log-likelihood is computed. The scale correction is taken from the minimum of this curve. It is then applied as a rescaling of the τ_h four-vector in simulation. The corrected τ_h four-vectors are also used to update $\vec{p}_T^{\text{miss}}$ and all related variables. The corrections are provided by the CMS Collaboration [60, 61]. Similarly, corrections are applied for electron misidentified as τ_h. These depend on the decay mode and η and are only applied for τ decays with one charged hadron with one or no neutral pion.

The description of the electron energy correction can be found in Section 3.2, whereas the muon energy correction can be neglected for this analysis.

Jet Energy Scale

Jet energies are corrected to match the expected detector response at the stable hadron level. These corrections are derived in bins of jet-p_T and η, as detailed in [83], and typically range between $10 - 15\,\%$. Additional residual corrections are applied to simulated events to account for differences between data and simulation. These corrections are generally below $1\,\%$ for high-p_T jets in the central detector region and up to a few percent in the forward region. All corrections are propagated to $\vec{p}_T^{\text{miss}}$ and any derived quantities, such as m_T or the estimated mass of the $\tau\tau$ system.

B Jet Identification Efficiency

A precise modeling of the b jet identification efficiency in simulation is important for this analysis, as a b jet veto is applied to suppress the background from the tt production.

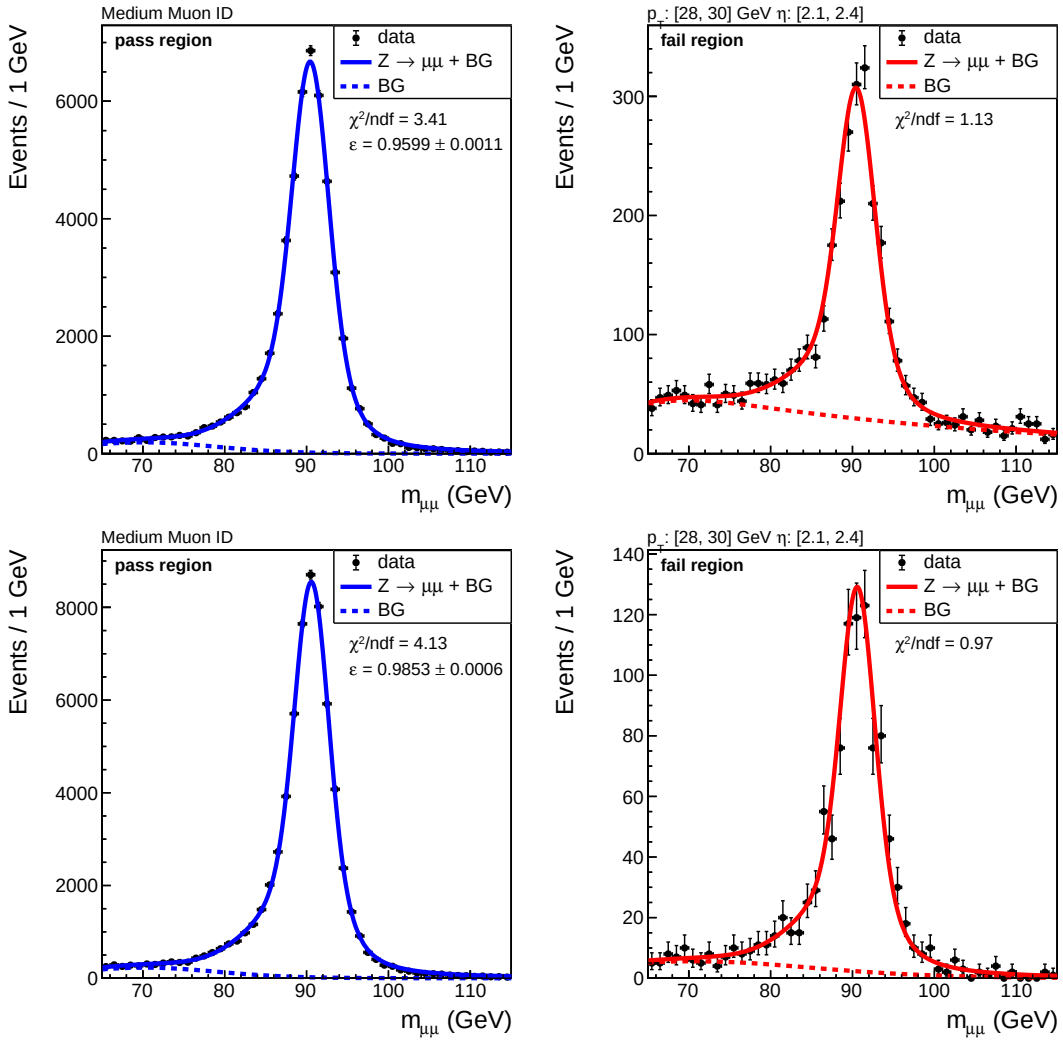

Figure 4.12.: Example distributions of $Z \to \mu\mu$ events for the pass (left) and fail (right) regions in the Tag-and-Probe measurement for data (top) and simulation (bottom). The probe muon is required to have $p_T \in [28, 30]$ and $|\eta| \in [2.1, 2.4]$. The black markers refer to data and simulation yields. The dashed line represents the background model, and the solid line shows the fitted signal-plus-background model.

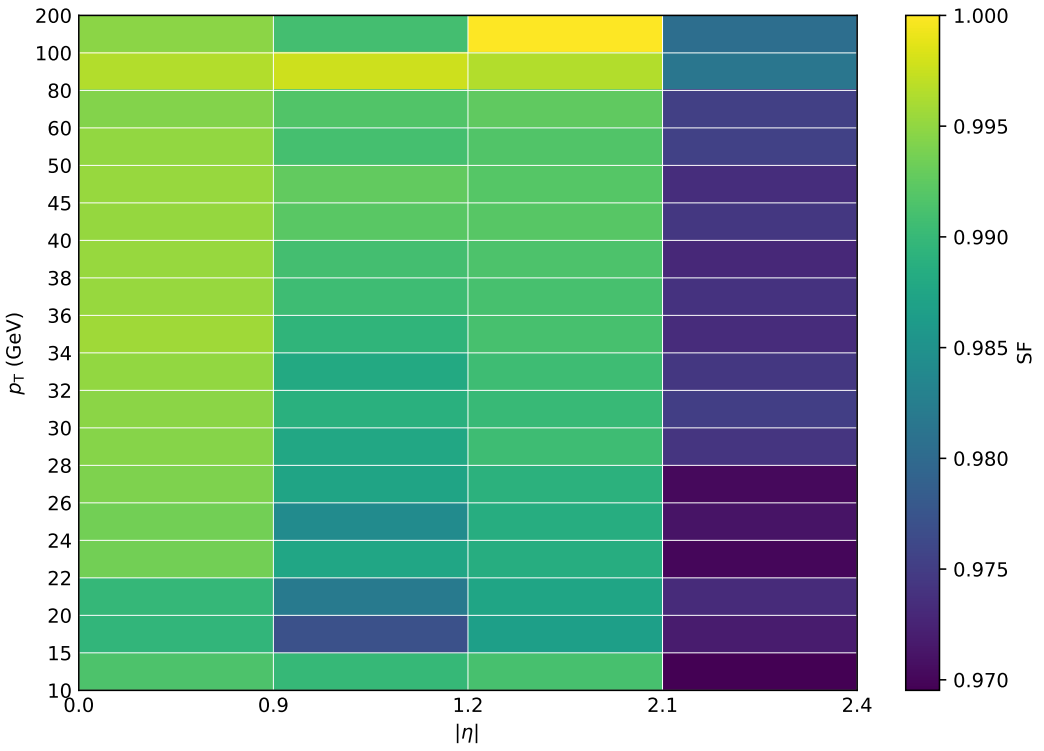

Figure 4.13.: Distribution of SFs for the muon medium ID binned in p_T and $|\eta|$ for the 2018 run period. No SF is larger than 3 % in this case, and the deviation between data and simulation is largest at high $|\eta|$.

However, the b jet efficiency in simulation does not perfectly match that in data. The CMS Collaboration provides the necessary corrections, derived using the Tag-and-Probe method in a tt-enriched phase space with two opposite-sign light leptons and at least two jets [84]. To reduce contamination from Drell–Yan production, events with a di-ℓ mass near the Z mass are excluded. One jet passing the medium DeepJet WP is selected as the tag. Similar methods are used to measure corrections for misidentified light-flavor jets in Drell–Yan events. The corrections are functions of the discriminant value D, jet-p_T, and η. An event weight is computed by multiplying the SFs for all jets in the event:

$$w_{\text{event}}^{\text{SF}} = \prod_{i=1}^{N_{\text{jets}}} \text{SF}(D_i, p_{T,i}, \eta_i). \tag{4.7}$$

Applying this weight alters the event yield in the analysis selection. To correct for this, a reweighting ratio is calculated using the total weights before and after applying the scale factors and before any b jet selection:

$$r = \frac{\sum_{i=1}^{N_{\text{events}}} w_i^{\text{before}}}{\sum_{i=1}^{N_{\text{events}}} w_i^{\text{after}}}. \tag{4.8}$$

These ratios are computed separately for each background process and analysis channel. The final per-event weight used in the analysis is

$$w_{\text{event}} = r \cdot w_{\text{event}}^{\text{SF}}. \tag{4.9}$$

4.2.4. Control Distributions of Modeling

Control distributions are used to check the consistency between data and estimation. They ensure that all estimated processes accurately represent the conditions observed by the CMS experiment. Additionally, these distributions help validate the reconstruction of physics objects in both data and the corresponding model. They can also reveal potential systematic effects in key observables. Relevant corrections for such effects, discussed in the previous section, are applied. In Figure 4.14, distributions of the (leading) light lepton p_{T} are shown exemplary using data integrated over all run periods of Run 2. Control distributions of more variables differential in single run periods can be found in the Appendix A.1. A quantitative evaluation of the agreement between data and estimation is performed via GoF tests, described in section 4.3.2.

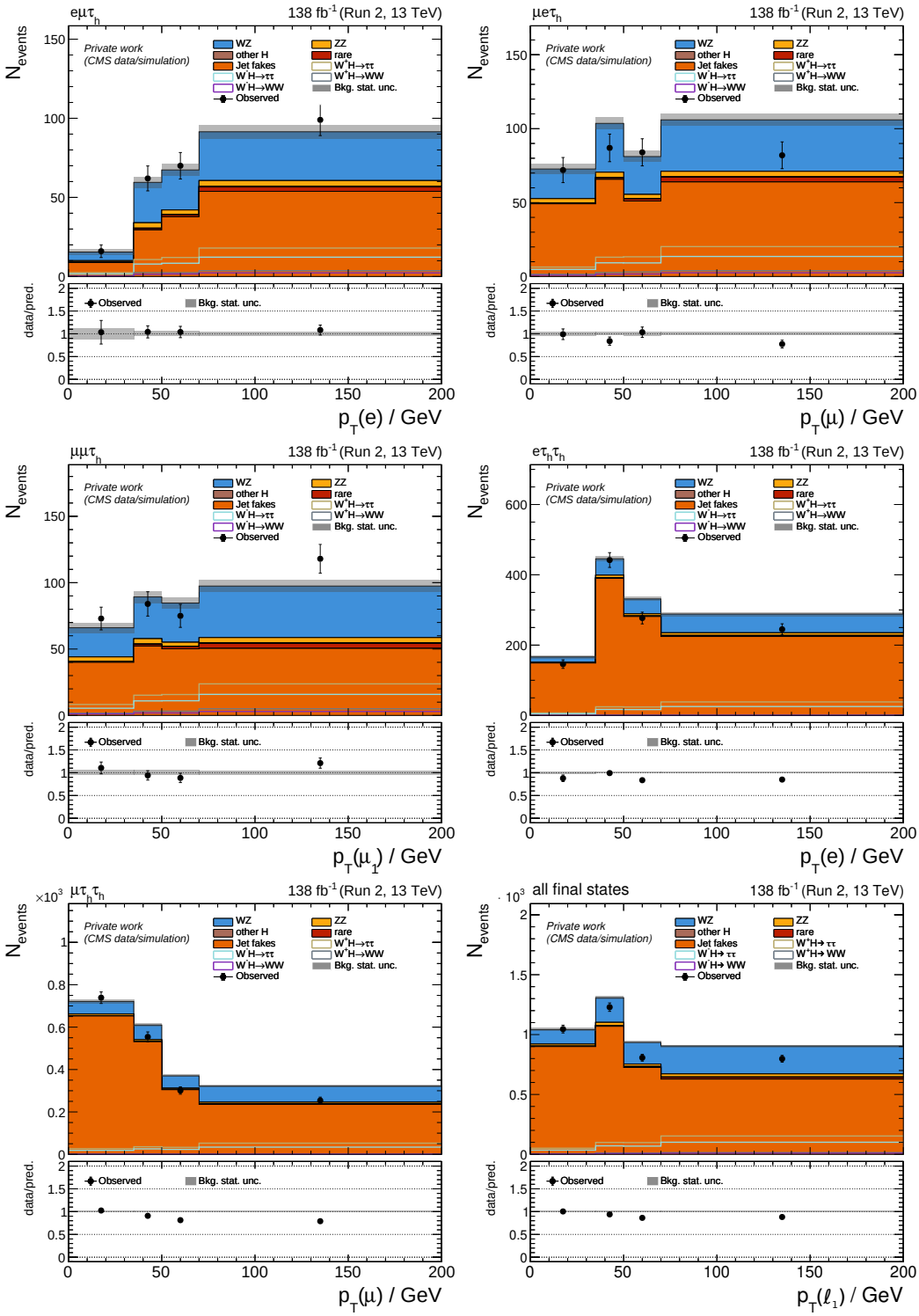

Figure 4.14.: Control distributions of the (leading) light lepton p_T in each final state integrated over all run periods with events passing the selection criteria described above. The bottom panel shows the ratio between data and estimation and the gray band shows the statistical uncertainty of the estimated processes.

4.3. Measurement Strategy

The measurements of $\sigma(\mathrm{WH})$, $\sigma(\mathrm{W^-H})$, $\sigma(\mathrm{W^+H})$, and A in the $\mathrm{WH}(\tau\tau)$ process involve several steps. First, selected events are categorized to enhance either signal or background contributions in distinct regions. Next, both observed events and those used for background and signal estimation are distributed into bins of a variable that separates signal from background. The aim is to maximize the signal-over-background ratio in bins with high signal efficiency. Finally, a statistical model is constructed, incorporating all relevant statistical and systematic uncertainties. Based on this model, the statistical inference of the signal is performed. This allows the determination of cross sections or interpretations in terms of signal strengths for the $\mathrm{W^\pm H}$ production process and A.

4.3.1. Event Classification via Neural Networks

To separate signal from background events, NNs are used. These classify events based on a variety of input variables, such as the kinematic properties of τ_h, electron and muon. It assigns each event to one of the predefined process categories. The architecture is based on a fully connected feed-forward design that includes an input layer featuring 22 event variables, two hidden layers with 128 nodes, and an output layer with one node for each process category used for categorizing events in the analysis. This categorization allows for a high purity of specific processes, either signal or background. Higher efficiency and purity in these categories lead to increased sensitivity of the measurement. All input variables are standardized to have zero mean and unit variance. The nodes in an NN follow the same structure. They receive inputs $\vec{x}^{\mathrm{prev}}$ from the previous layer to compute a weighted sum:

$$\tilde{x}_j(\vec{x}^{\mathrm{prev}}) = \sum_i^N w_i \cdot x_i^{\mathrm{prev}} + b. \tag{4.10}$$

Here, each node j has a trainable weight vector $\vec{w}$, matching the number of inputs from the previous layer N, and a trainable bias term b. After calculating this sum, an activation function is applied to introduce non-linearity. For the hidden layers, the hyperbolic tangent function is used:

$$x_j(\vec{x}^{\mathrm{prev}}) = \tanh(\tilde{x}_j(\vec{x}^{\mathrm{prev}})). \tag{4.11}$$

Compared to other non-linear activation functions, the hyperbolic tangent is a smooth function with a well-defined first and second derivative at all points, which is important for the calculation of Taylor coefficients explained below. In the output layer, a softmax function is applied, with j running over all output nodes i:

$$y_i = \frac{e^{x_i}}{\sum_j e^{x_j}}. \tag{4.12}$$

This ensures the NN output scores y_i being between zero and one, which allows for an interpretation that an event belongs to a process category with a certain probability. An event is then assigned to the category with the highest y_i. A sketch of the NN architecture is given in Figure 4.15. The training is based on minimizing the categorical cross-entropy

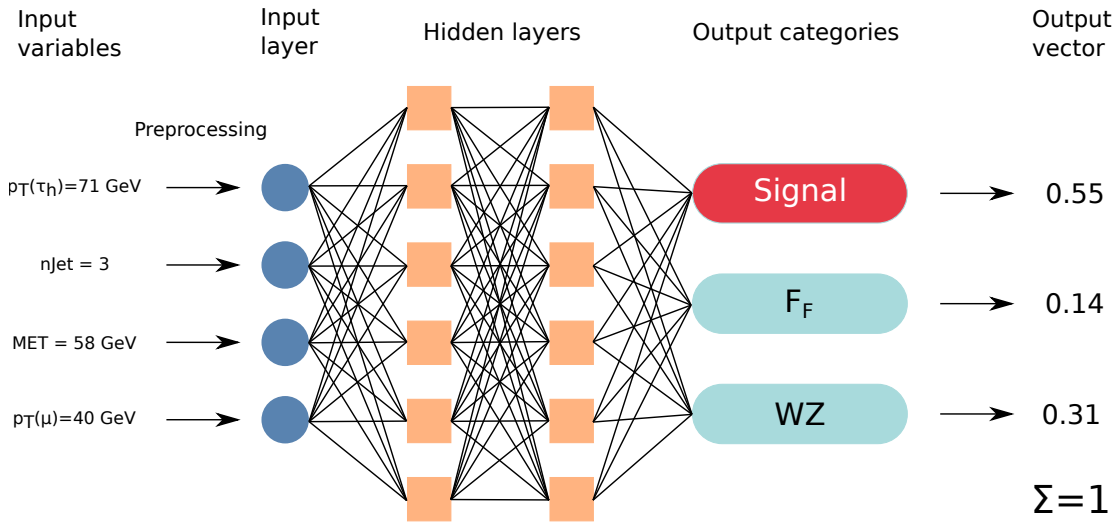

Figure 4.15.: Sketch of the NN classification: The input layer receives a vector of 22 variables describing the kinematic properties of various objects of a single event. After passing through two hidden layers, the NN output vector outputs a score for each output category indicating how likely an event belongs to the given category. Two of these categories correspond to the main background processes and one to the signal processes.

loss function $\mathcal{L}$, which compares the predicted and true class labels:

$$\mathcal{L} = -\sum_{n}^{N}\sum_{i}^{C} y^{(n)}_{\text{true},i} \cdot \log(y^{(n)}_{\text{pred},i}). \tag{4.13}$$

After processing a batch, the NN weights are updated. The first sum runs over all N events in a given batch. The second sum compares the true label $y^{(n)}_{\text{true},i}$ with the predicted value $y^{(n)}_{\text{pred},i}$ for each of the C output categories where $y^{(n)}_{\text{true},i}$ is one for the correct category and zero for all others. The objective of the NN training is to minimize $\mathcal{L}$. The minimization is performed using backpropagation and exploiting the Adam optimization algorithm [85], with an initial learning rate of $\eta = 10^{-5}$. The optimization rule for the w_i has the form

$$w_{\text{new},i} = w_i - \eta \frac{\partial \mathcal{L}}{\partial w_i}. \tag{4.14}$$

As the NN processes the training data, it learns the features that characterize the different physics processes. To avoid the NN from learning patterns that are specific to the training sample and not representative of the general process known as overtraining, Dropout [86] and L2 regularization [87] algorithms are applied. The Dropout algorithm randomly disables a fraction of nodes during training. This helps prevent the NN from relying too heavily on specific nodes, a common symptom of overtraining. In this analysis, a dropout rate of 30 % is applied, meaning that 30 % of the nodes are randomly turned off in each training iteration. L2 regularization adds a penalty term to the loss for large weight values

Table 4.5.: List of hyperparameters used to train the NNs.

Hyperparameter	value
Dropout	0.3
Learning rate	0.0001
L2 regularization	0.001
Batch size	256
Early stopping	50
Early stopping threshold	0.1

to reduce the dependence of the NN on single trainable parameters. The chosen set of hyperparameters is presented in Table 4.5. The training data is split into two halves. Each half is used to train a NN model, which is then applied to the other half to exploit the full available statistics. Within each half, a further split into training (75 %) and validation (25 %) subsets ensures proper control of the learning process. After every training step, $\mathcal{L}$ is evaluated on the independent validation dataset with fixed training weights. The training is stopped once the performance on the validation data stops improving with the early stopping threshold of 0.1 within 50 iterations, known as epochs. The evolution of $\mathcal{L}$ over epochs is shown for the $\mu\tau_h\tau_h$ final state in Figure 4.16. The training and validation loss decrease monotonically, while the validation loss flattens and eventually turns upward, indicating the onset of overfitting. With a patience of 50 epochs, early stopping triggers at epoch 176. The NN model is restored to the checkpoint at the validation-loss minimum (red dashed line) for optimal performance on unseen events.

A separate NN is trained for each final state to account for the distinct event topologies and background compositions. In contrast, the differences between the four data-taking periods are relatively small. Moreover, the available dataset is too limited to train a separate NN for each data-taking period. Therefore, a single NN is used across all eras. To allow the NN to adapt to era-specific characteristics, the data-taking years are encoded as four Boolean input nodes. Only one of these nodes is activated per event, corresponding to the respective era.

Grouping Processes into Neural Network Output Classes

The NN output nodes are designed to represent distinct physics processes. The goal of the multiclass classification is not only to separate signal from background but also to isolate the main background processes into dedicated control regions. This categorization improves the precision of the measurement, as categories with high purity allow for better constraints on systematic uncertainties related to the major background processes during the statistical inference. For example, if the cross section of WZ production is mis-estimated, this effect will be visible in the corresponding category. This enables the fit to correct such deviations and constrain the systematic uncertainty related to the WZ cross section.

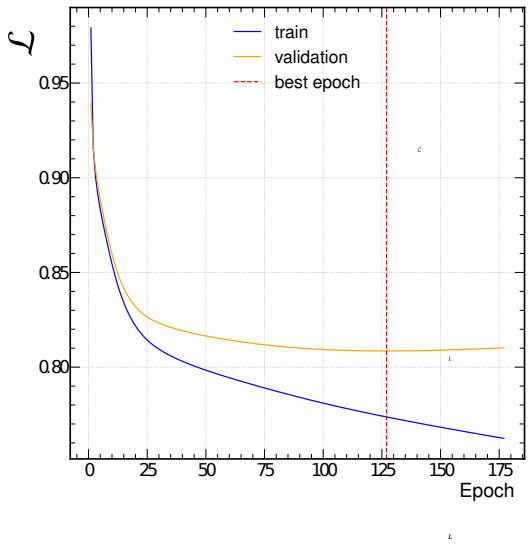

Figure 4.16.: $\mathcal{L}$ of the training and validation sample versus epoch for the $\mu\tau_h\tau_h$ final state. The red dashed line marks the epoch of the minimum validation loss. The NN configuration of this epoch is used for the statistical inference of the signal.

Three categories are chosen, reflecting the phase space for signal and the two major background sources:

- WH: The signal class with WH($\tau\tau$) and WH(WW) events.
- F_F: This category is dominated by events with jet $\rightarrow \tau_h, \mu, e$ mainly due to Drell–Yan, W+jets and tt processes and modeled by the F_F method. Also, other minor backgrounds like ttV, ggZZ, ggZH, ZH, VVV are included in this category.
- WZ: Events from WZ and ZZ, where WZ dominates the category.

As no dedicated sample for jet $\rightarrow \tau_h, \mu, e$, exists, events of each AR_i are used and weighted by the corresponding event-dependent F_F^i to reflect their contribution to the yield. Figure 4.17 shows the confusion matrix of the $\mu\tau_h\tau_h$ final state, which is used to quantify per-class efficiencies. The signal class is identified with the highest efficiency (≈67 % on the diagonal), while F_F and WZ are more challenging (≈45 % and ≈50 %, respectively). The similarity in topology between the signal and WZ processes is evident in the cross-class assignments: ≈21% of signal events are predicted as WZ, and ≈25% vice versa. The reduced efficiency of processes of the WZ class further reflects its topological similarity to processes of the F_F class, which increases confusion between the two classes. The input variables and their power to discriminate between the different processes are discussed in the next paragraphs.

4.3.2. Input Variables of the NN and their Validation

For event classification, the NN is provided with a set of input features for each event. Variables related to the final state objects are expected to carry discriminating power, as

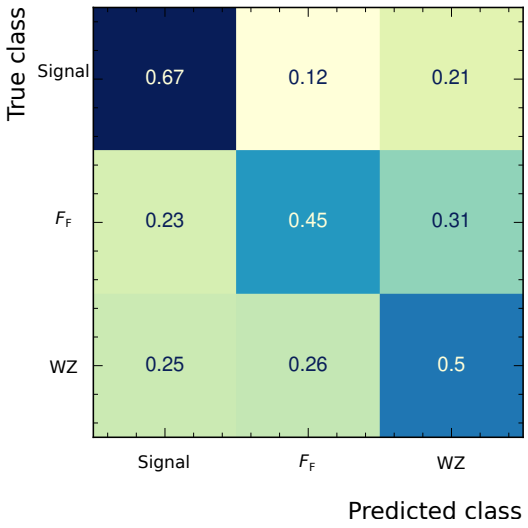

Figure 4.17.: Row-normalized confusion matrix of the NN; diagonal entries indicate per-class efficiencies, and off-diagonal entries quantify cross-class misidentification efficiencies.

they are direct decay products of the signal process. But also higher-level variables like $p_{\mathrm{T}}^{\mathrm{miss}}$ or the scalar sum of p_{T} of the final state objects are selected. Additionally, jet-related variables are included in the input vector. A summary of the variable selection is given in Table 4.6.

The choice of input variables is based on the Taylor coefficient analysis (TCA) [88]. Via this method the contribution of each input feature to the NN classification is evaluated. Starting from 30 input feature candidates, eight features were removed due to their negligible impact. In the TCA applied to this analysis the NN output function of the signal class, $y_{\mathrm{WH}}(\vec{z})$, is expanded into a Taylor series with respect to the NN input vector $\vec{z}$ up to second order. For an event $\vec{a}$ with input feature values a_i, the expansion reads

$$y_{\mathrm{WH}}(\vec{z}) \approx f(\vec{a}) + \sum_i t_{z_i}(z_i - a_i) + \frac{1}{2}\sum_{i,k} t_{z_i z_k}(z_i - a_i)(z_k - a_k)\,.$$

The first-order coefficients t_{z_i} measure the sensitivity of the NN output to changes in single variables z_i. The second-order coefficients $t_{z_i z_k}$ quantify the impact of linear correlations between variable pairs. The mean absolute Taylor coefficient for feature z_i is defined as

$$\langle t_i \rangle = \frac{\sum_{j=1}^{N} w_j \, |t_i(a_j)|}{\sum_{j=1}^{N} w_j}\,,$$

with event weights w_j and total number of events N. Using $\langle t_i \rangle$ to rank the input variables, it is possible to include both marginal and correlation effects. Figure 4.18 shows the most important features to classify the signal process for all final states. Across all final states, $p_{\mathrm{T}}^{\mathrm{tot}}$, $p_{\mathrm{T}}^{\mathrm{miss}}$, and $m(\tau\tau)$ have the highest sensitivity to classify the signal processes. The variable $p_{\mathrm{T}}^{\mathrm{tot}}$ is expected to be close to zero for the signal processes. This results from summing the p_{T} of all final-state particles from the primary interaction, including the

Table 4.6.: Selection and short description of variables used to train the NNs.

Label	Description
pt_1	p_T of the (leading) ℓ
pt_2	p_T of the sub-leading ℓ in $\ell\ell\tau_h$ or leading τ_h in $\ell\tau_h\tau_h$
pt_3	p_T of the (sub-leading) τ_h
m_vis	Visible mass of the $\tau\tau$-system
pt_vis	Visible p_T of the $\tau\tau$-system
jpt_1	p_T of the leading non-b-tagged jet
jpt_2	p_T of the sub-leading non-b-tagged jet
njets	Number of non-b-tagged jets
eta_1	η of the (leading) ℓ
eta_2	η of the sub-leading ℓ in $\ell\ell\tau_h$ or leading τ_h in $\ell\tau_h\tau_h$
eta_3	η of the (sub-leading) τ_h
deltaR_13	ΔR of the leading ℓ and τ_h in $\ell\ell\tau_h$ or the ℓ and sub-leading τ_h in $\ell\tau_h\tau_h$
deltaR_12	ΔR of the leading and sub-leading ℓ in $\ell\ell\tau_h$ or the ℓ and leading τ_h in $\ell\tau_h\tau_h$
deltaR_23	ΔR of the sub-leading ℓ and τ_h in $\ell\ell\tau_h$ or the leading and sub-leading τ_h in $\ell\tau_h\tau_h$
Lt	Scalar sum of the p_T of the final state objects
met	Missing transverse momentum p_T^{miss}
m_tt	Reconstructed mass of the $\tau\tau$-system $m(\tau\tau)$
mt_1	m_T of the (leading) ℓ and $\vec{p}_T^{miss}$
mt_2	m_T of the sub-leading ℓ in $\ell\ell\tau_h$ or leading τ_h in $\ell\tau_h\tau_h$ and $\vec{p}_T^{miss}$
mt_3	m_T of the (sub-leading) τ_h and $\vec{p}_T^{miss}$
pt_W	Reconstructed p_T of the W boson
pt_123met	p_T of the sum of 4-vectors of the final state objects and $\vec{p}_T^{miss}$: p_T^{tot}

neutrinos from the W and $\tau\tau$ decays. As a consequence, momentum conservation in the transverse plane is satisfied, yielding values near zero for well-reconstructed signal events. The reconstructed mass of the $\tau\tau$ system, $m(\tau\tau)$, exhibits a pronounced peak at approximately 125 GeV, consistent with the Higgs boson mass. This feature provides strong separation power against the dominant backgrounds, like WZ and jet $\rightarrow \tau_h, \mu, e$, both of which peak at significantly lower values. Furthermore, the WZ and WH processes typically yield larger p_T^{miss} than the jet$\rightarrow \tau_h$, μ,e background. This difference is effectively exploited by the NN to enhance discrimination between these processes. In Figure 4.19, distributions of those variables are shown for the $\mu\tau_h\tau_h$ final state.

The NN input variables are validated using GoF tests. These tests quantify how well the background model describes the data. Both statistical and systematic uncertainties are included. The main method is the *saturated model test* [89]. It is a likelihood-based extension of the χ^2 test,

$$\chi^2 = \sum_i \frac{(d_i - f_i)^2}{\sigma_i^2}, \tag{4.15}$$

where d_i is the observed value for bin i, σ_i its uncertainty, and f_i the model prediction.

In a case with only statistical uncertainties, the likelihood is

$$\mathcal{L} = \prod_i \frac{1}{\sqrt{2\pi\sigma_i^2}} \exp\left[-\frac{(d_i - f_i)^2}{2\sigma_i^2}\right]. \tag{4.16}$$

For the saturated model it holds $f_i = d_i$, giving

$$\mathcal{L}_{\text{saturated}} = \prod_i \frac{1}{\sqrt{2\pi\sigma_i^2}}. \tag{4.17}$$

With equations 4.16 and 4.17 the likelihood ratio can be calculated via

$$\lambda = \frac{\mathcal{L}}{\mathcal{L}_{\text{saturated}}} = \prod_i \exp\left[-\frac{(d_i - f_i)^2}{2\sigma_i^2}\right], \tag{4.18}$$

leading to the test statistic

$$q_{\text{obs}} = -2 \ln \lambda. \tag{4.19}$$

For the simple case above, $q_{\text{obs}} = \chi^2$. This equality does not hold for likelihoods that include systematic uncertainties like in this analysis.

The saturated model always maximizes the likelihood. Thus, $\lambda \leq 1$ and $q_{\text{obs}} \geq 0$. Smaller q_{obs} means better agreement between model and data. The test is not sensitive to the sign or ordering of deviations and therefore cannot easily detect correlated trends in the data. Therefore, if necessary, the Kolmogorov-Smirnov [90, 91] and Anderson-Darling [92] tests are also performed.

The p-value is computed with Monte Carlo toys based on the uncertainty model. For each variable and variable pair in each final state and run period, 1000 pseudo-datasets are generated. As the NN is also sensitive to correlations between variables, both 1D and 2D GoF tests are performed in order to detect correlated clusters of mis-modeling. For the

input variable set in Table 4.6, in total 440 1D and 4620 2D tests of this kind have been performed. All nuisance parameters have been varied according to their uncertainties. The p-value is

$$p = \frac{N_{\text{toys}}(q_{\text{toy}} \geq q_{\text{obs}})}{N_{\text{toys}}}, \tag{4.20}$$

while values near zero indicate strong disagreement and variables above a predefined value of $p = 5\,\%$ pass the test. For the 1D tests, 10 equipopulated bins are used. For the 2D tests neighboring bins are merged to obtain 5×5 bins for each variable pair. In case a bin contains less than 10 expected events, neighboring bins are merged. In Figure 4.20, the distribution of the leading τ_h p_T in the $\mu\tau_h\tau_h$ final state in the 2018 run period is shown together with its toy distribution and the saturated GoF test result. Variables with low p-values in GoF tests are scrutinized for systematic mis-modeling and compared with their Taylor coefficient ranking, with priority given to failed GoF tests among the highest-ranked variables. Systematic mis-modeling is diagnosed by a persistent trend in the data/estimation ratio and by the recurrence of similar deviations across related final states and across different run periods; for variables meeting these criteria and showing high sensitivity to the NN output, dedicated modeling uncertainties are assigned.

The outcomes of the 1D GoF tests are presented in Figures A.21 - A.39, while the results of the 2D GoF tests are shown in Figures A.41-A.60. A consolidated overview of all test results is provided in Figure 4.21. Out of the 440 individual 1D tests performed, approximately 98 % meet the defined GoF criteria. For the 4620 2D tests, about 96 % pass the test, which demonstrates the good agreement between data and model.

During the GoF test evaluation, the uncertainty model of the F_F method was refined by introducing two additional uncertainty components. These were specifically designed to address observed mis-modeling in p_T^{miss} and the (leading) lepton p_T, which have particularly large influence on the NN performance. Their calculation is described in details in section 4.4.2. Post-fit distributions of those variables in the $\mu\tau_h\tau_h$ final state for the 2018 run period can be found in Figure 4.22. After these adjustments, no further significant mis-modeling was identified. The distribution of GoF test results in the $\mu\tau_h\tau_h$ final state in the 2018 run period is shown in Figure 4.23. In this case, no variable is failing the GoF test. Variables with failed GoF tests were studied, and no further systematic mis-modeling or pathological behavior was found. Variables that failed the test were assessed to fail due to statistical fluctuations in single bins.

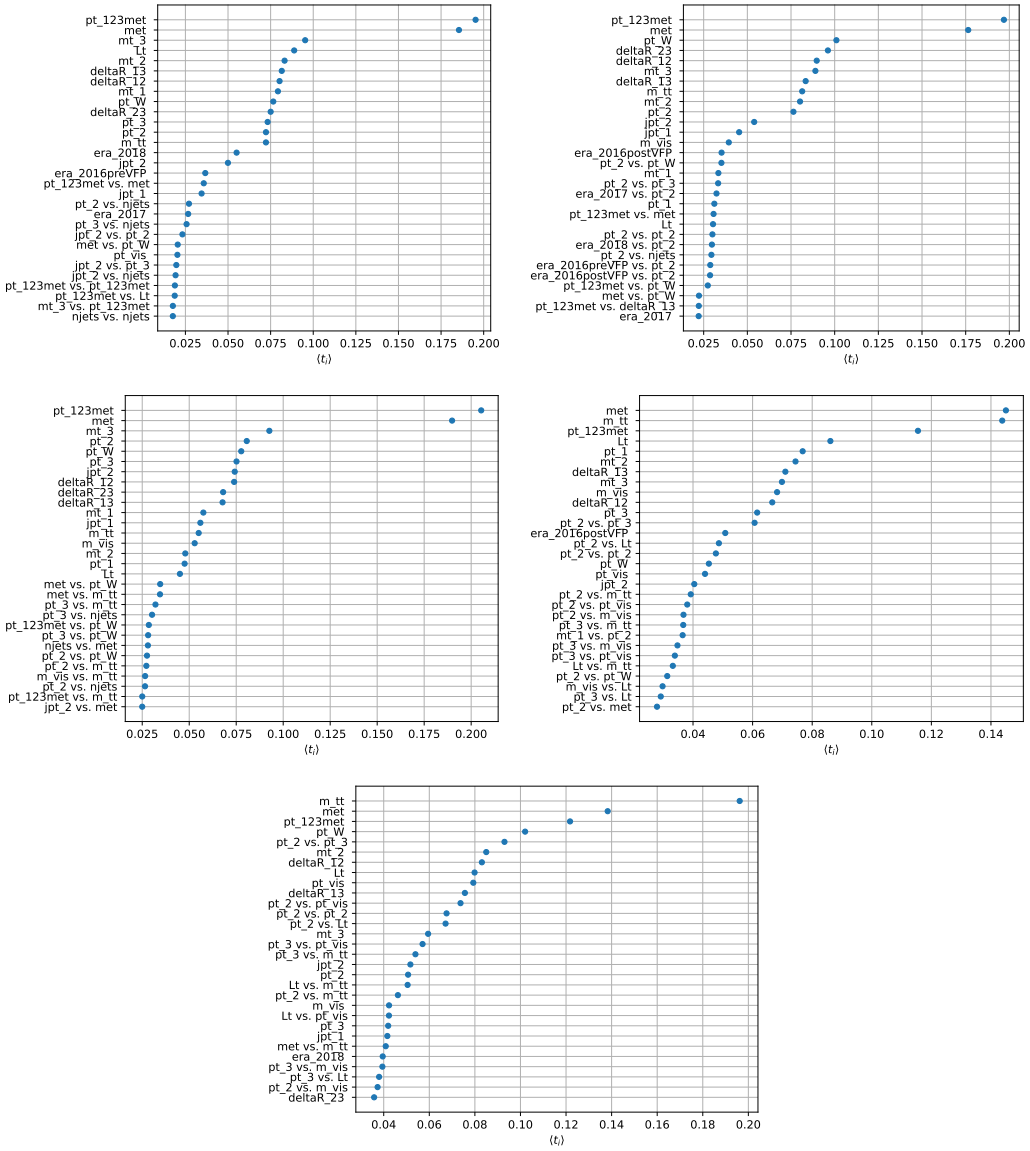

Figure 4.18.: TCA ranking of the NN input features to discriminate signal events from background for $e\mu\tau_h$ (upper left), $\mu e\tau_h$ (upper right), $\mu\mu\tau_h$ (middle left), $\mu\tau_h\tau_h$ (middle right), and $e\tau_h\tau_h$ (bottom) final states.

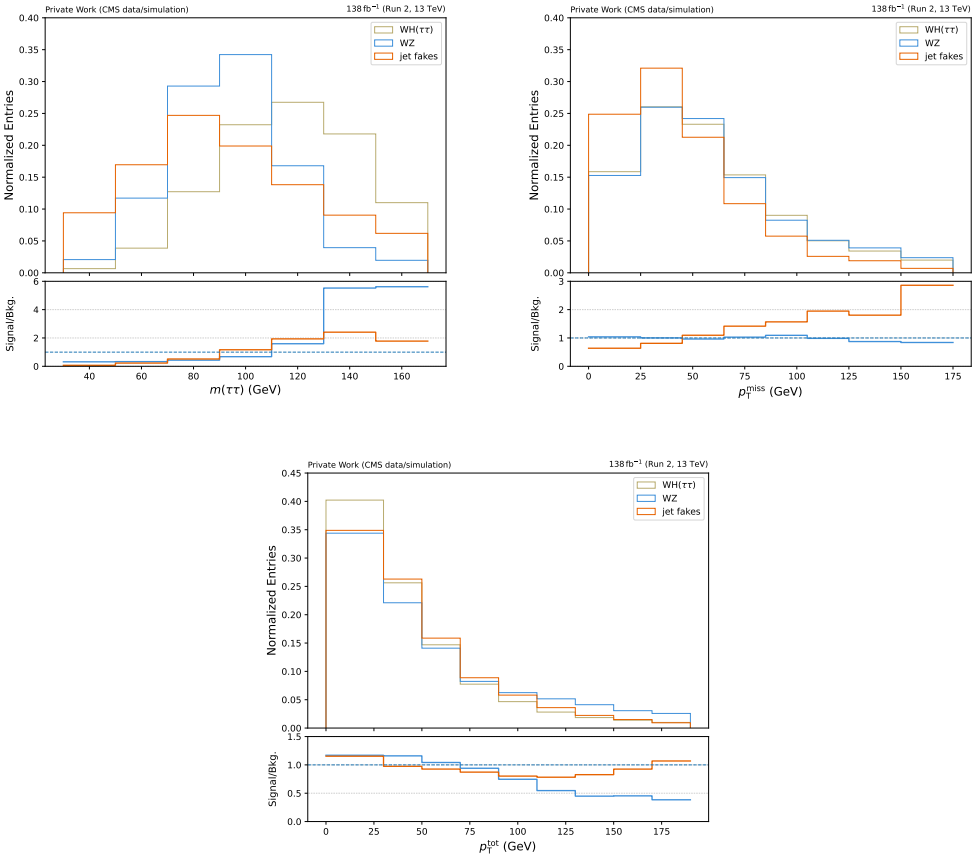

Figure 4.19.: Normalized distributions of the signal and the two major backgrounds in the $\mu\tau_h\tau_h$ final state. The events are distributed in the three most sensitive variables for the NN to classify the signal correctly.

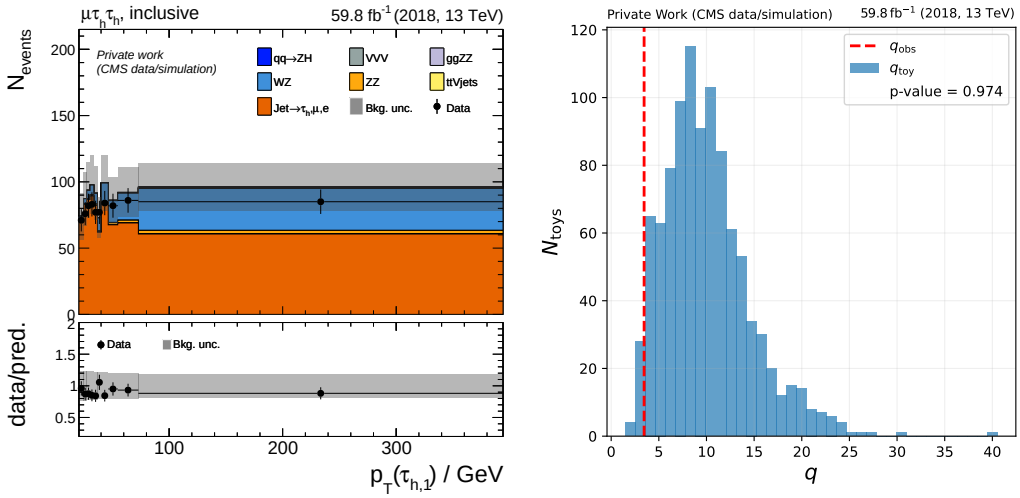

Figure 4.20.: Pre-fit distribution (left) of the leading τ_h p_T in the $\mu\tau_h\tau_h$ final state in the 2018 run period. In gray the combined statistical and systematic uncertainties are shown. On the right, the distribution of the saturated GOF test statistic q is shown for 1000 toy datasets with varied samples of the statistical model. The observed value, q_{obs}, is given with a p-value of 0.974.

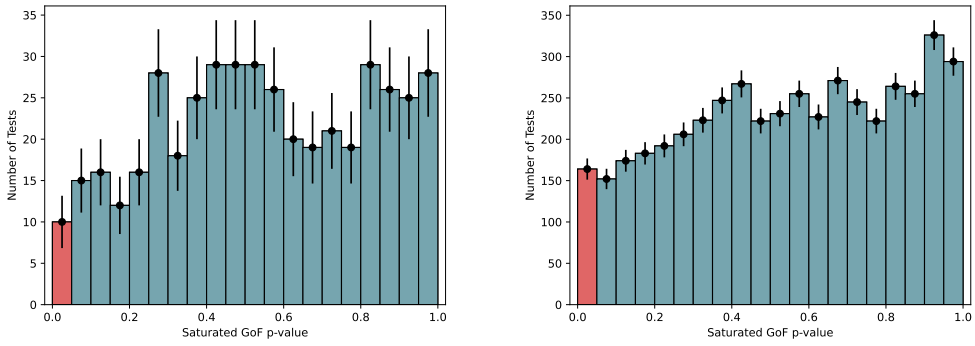

Figure 4.21.: Aggregated GoF test results for all run periods and final states. On the left for the 440 1D tests and on the right for the 4620 2D tests. In red the tests below $p = 5\,\%$ are shown. The error bars correspond to the Poisson-error in each bin.

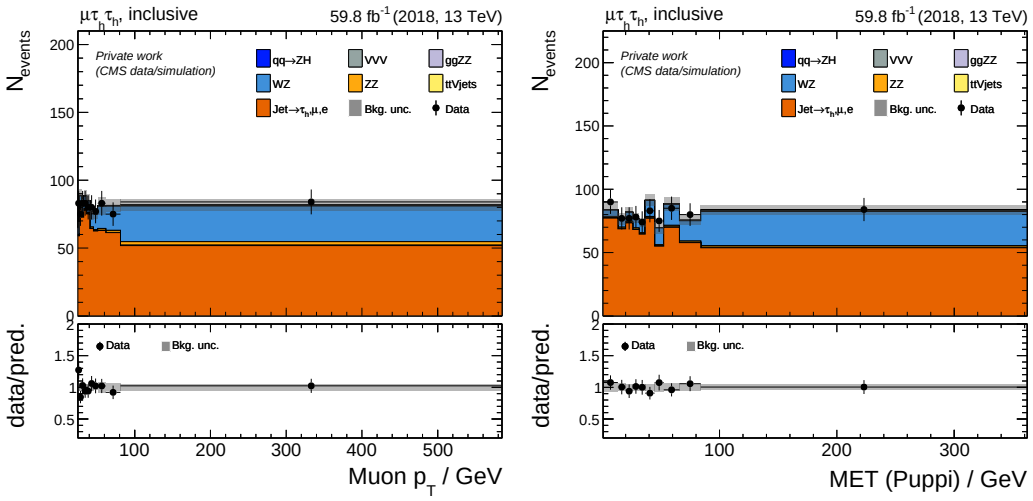

Figure 4.22.: Post-fit distributions of $p_{\mathrm{T}}(\mu)$ (left) and $p_{\mathrm{T}}^{\mathrm{miss}}$ (right) in the $\mu\tau_{\mathrm{h}}\tau_{\mathrm{h}}$ final state in the 2018 run period after introducing dedicated systematic uncertainties affecting the shape of the distributions.

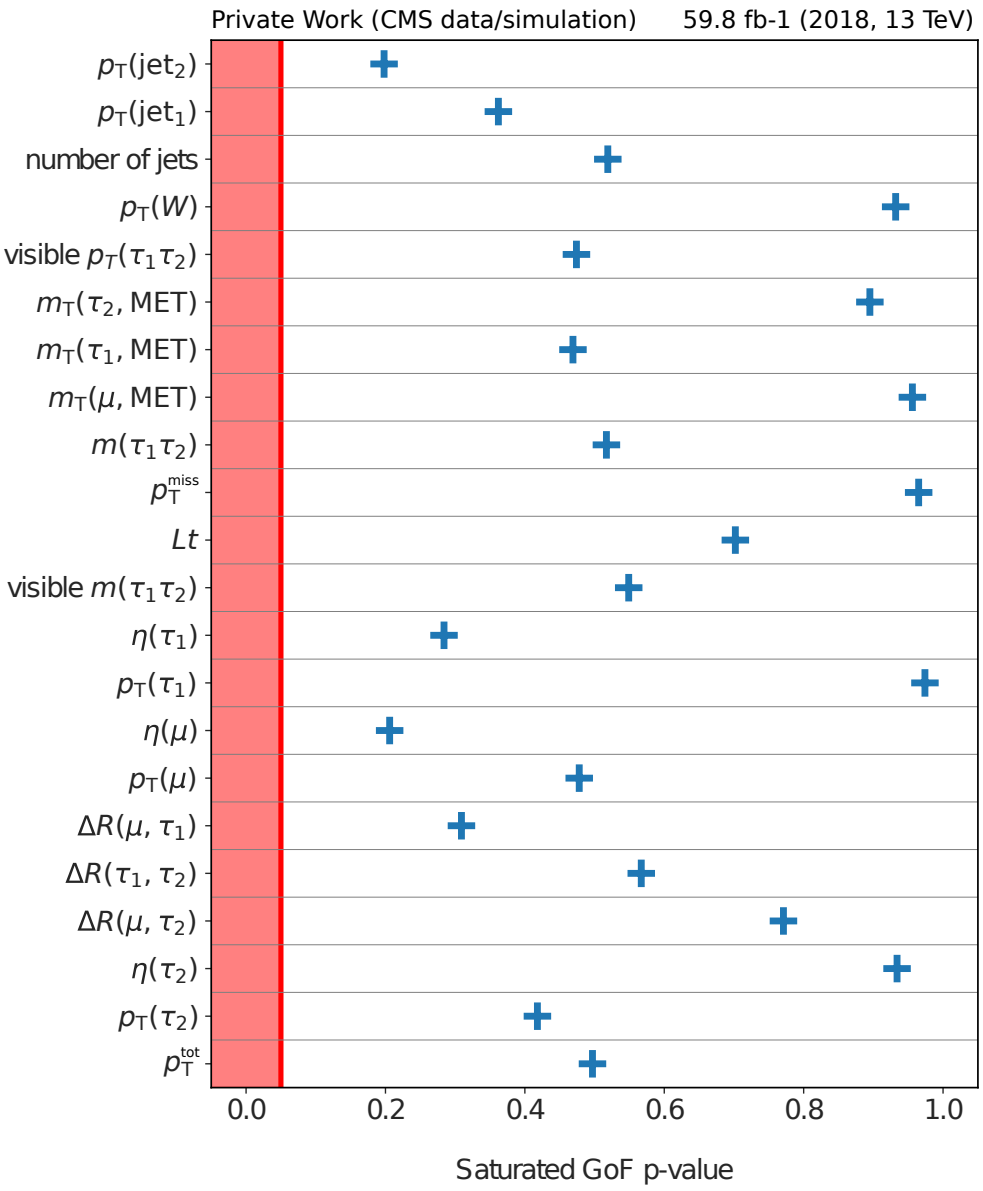

Figure 4.23.: Distribution of the results of the 1D GoF tests of all individual NN input variables for the $\mu\tau_h\tau_h$ final state in the 2018 run period. The red area marks the region $p < 5\,\%$, which is considered the boundary for failed tests. No variable fails the saturated GoF test in this final state and run period.

4.4. Statistical Inference and Results

4.4.1. Statistical Inference

After the event classification, three NN output categories are obtained enriched in certain processes: two background control categories, F_{F} and WZ, and one signal category, WH. Each event is assigned to the category in which it obtains the highest NN score y_i. This score also serves as the final discriminant for signal extraction. For three categories, the minimal possible score is 1/3 and the maximum is 1.0.

In addition, the y_i distributions are separated according to the charge of the light lepton associated with the W boson. This allows sensitivity to $\sigma(\mathrm{W^+H})$, $\sigma(\mathrm{W^-H})$, and A. In summary, six categories per final state and run period are included in the fit. For the statistical inference of the signal, the three di-ℓ final states are combined into $\ell\ell\tau_{\mathrm{h}}$ and the two di-τ_{h} final states into $\ell\tau_{\mathrm{h}}\tau_{\mathrm{h}}$. This ensures enough events in each bin of the distributions. In total, six categories in two final states and four run periods, result in 48 distributions, entering the fit. If a bin contains fewer than ten expected events, it is merged with an adjacent bin to ensure statistical stability. Merging starts from the bin with the highest y_i values and proceeds toward lower values. High-score bins correspond to events with a high probability of belonging to the target process of the category. In background categories, these bins form control regions that constrain background uncertainties in the fit. In the signal category, the highest-score bins have the largest signal-to-background ratio and thus dominate the sensitivity for the POIs, which are $\sigma(\mathrm{W^+H})$, $\sigma(\mathrm{W^-H})$, $\sigma(\mathrm{WH})$, and A. The cross sections, σ_j, can be interpreted in terms of a signal strengths given by

$$\mu_j = \frac{\sigma_j^{\mathrm{obs}}}{\sigma_j^{\mathrm{SM}}}, \tag{4.21}$$

with the SM expectation σ_j^{SM} for process j.

Summing over all signal processes j the categories enter a combined binned likelihood function defined by:

$$\mathcal{L}(d \mid \mu_j \cdot s_j(\vec{\theta}) + b(\vec{\theta})) = \prod_{i \in \mathrm{bins}} \mathcal{P}\left(n_i \mid \mu_j \cdot s_{ij}(\vec{\theta}) + b_i(\vec{\theta})\right) \times \prod_{k \in \mathrm{nuis}} C(\hat{\theta}_k \mid \theta_k)\,, \tag{4.22}$$

where $\mathcal{P}$ is the Poisson probability for observing n_i events in bin i, given the expected signal s_{ij} and background b_i yields, defined by:

$$\mathcal{P}\left(n_i \mid \mu_j \cdot s_{ij}(\vec{\theta}) + b_i(\vec{\theta})\right) = \frac{\left(\mu_j \cdot s_{ij}(\vec{\theta}) + b_i(\vec{\theta})\right)^{n_i}}{n_i!} \cdot \exp\left(-\left(\mu_j \cdot s_{ij}(\vec{\theta}) + b_i(\vec{\theta})\right)\right). \tag{4.23}$$

The signal is scaled by the signal strength modifier μ_j introduced in Equation 4.21. Both s_{ij} and b_i depend on nuisance parameters $\vec{\theta}$, which are constrained by prior probability density functions C.

The fit maximizes $\mathcal{L}$ to obtain the best-fit values for μ_j and $\vec{\theta}$, denoted as $\hat{\mu}_j$ and $\hat{\vec{\theta}}$. In the context of this thesis, three different fits with three different signal models are

performed. In the first and easiest model, s corresponds to the WH process inclusive in charge with the corresponding signal strength $\mu(\mathrm{WH})$. In the second model μ and s are 2D vectors for the $\mathrm{W^+H}$ and $\mathrm{W^-H}$ processes. The third model to obtain A is more complicated, as A has nonlinear dependencies on $\sigma(\mathrm{W^+H})$ and $\sigma(\mathrm{W^-H})$. Accordingly, the following substitutions are introduced to fit A:

$$\mu(\mathrm{W^+H}) = \frac{\sigma(\mathrm{WH}) \cdot (1 + A)}{2\sigma_{\mathrm{SM}}(\mathrm{W^+H})}, \tag{4.24}$$

$$\mu(\mathrm{W^-H}) = \frac{\sigma(\mathrm{WH}) \cdot (1 - A)}{2\sigma_{\mathrm{SM}}(\mathrm{W^-H})}. \tag{4.25}$$

Here the second fit model is parameterized by A and $\sigma(\mathrm{WH})$. Systematic uncertainties are encoded as nuisance parameters $\vec{\theta}$, affecting both signal and background estimates. Their treatment is a key part of the statistical inference and will be detailed in the following paragraphs.

4.4.2. Uncertainty Model

The systematic uncertainties considered for this analysis have three main sources: object reconstruction and identification, background modeling, and the limited statistical precision of the template distributions used for signal extraction. The template-statistics uncertainty is implemented for each bin of every template distribution individually. All other uncertainties induce correlated variations across bins and can take the form of simple normalization changes or more complex shape effects. Depending on their derivation, correlations may also be present across different run periods, between individual signal and background processes, or even among distinct uncertainties.

Uncertainties of Simulated Events

The main sources of uncertainties in simulated signal and background events originate from corrections to address differences between simulation and data. Corrections associated with the reconstruction and identification of physics objects—such as electrons, muons, jets, and τ_{h}—have been discussed in Section 3.2. This section provides a summary of the corresponding uncertainties. All systematic uncertainties related to simulation are treated as correlated across the final states if those final states share the same objects.

Identification and Isolation of electron and muon

For electron and muon identification, a global rate uncertainty of 2 % is applied in final states with those objects. For electrons in the endcap region ($|\eta| > 1.479$) and with $p_{\mathrm{T}} > 100\,\mathrm{GeV}$, the uncertainty is increased to 2.5 %. For the I_{rel} correction of electrons, a global rate uncertainty of 0.5 % is chosen, whereas the I_{rel} uncertainty on muons is negligible. Rate uncertainties are chosen rather than a shape-dependent uncertainty, as the identification and I_{rel} efficiencies show only a weak dependence on the p_{T} of the light lepton.

Single Electron and Muon Triggers

A rate uncertainty of 2 % for single muon trigger corrections and 3 % for single electron trigger corrections is applied.

Identification and Energy Scale of τ_h

In the $\ell\ell\tau_h$ final states, identification scale factors are determined in bins of p_T of the τ_h candidate, while in the $\ell\tau_h\tau_h$ final states, they are obtained in bins of the τ_h decay mode. The corresponding uncertainties, provided by CMS [60, 61], are propagated as uncorrelated shape variations for each p_T or decay mode bin. These uncertainties are typically of the order of 3 % and are mostly statistical in origin, which makes them uncorrelated between run periods. A yield uncertainty of 3 % is assigned to account for the use of a different D_e WP than those in the CMS measurement. For the τ_h energy scale, corrections are applied as a function of the τ_h decay mode. The associated uncertainties depend on the decay mode and the run period and are treated as shape-dependent.

Jet Energy Scale and Resolution

The calibration of jet energies in CMS is subject to multiple sources of systematic uncertainties, collectively referred to as jet energy scale (JES) uncertainties. In total, 27 individual sources are defined. In this analysis, they are grouped into 11 merged sources by combining strongly correlated components, reflecting the limited sensitivity of the measurement to jet energy variations. The uncertainty scheme covers the absolute JES calibration, the relative JES calibration between different detector regions, and statistical limitations of the JES measurements. Additional contributions arise from the dependence of the calibration on the jet flavor (b, c, gluon, or light quark), as well as from non-closure corrections that address residual discrepancies between simulation and data.

In simulation, the jet energy resolution is typically better than in data. To account for this difference, an additional smearing is applied to jet energies in simulated events, and an associated systematic uncertainty is introduced.

Top Quark p_T

For ttV events, a top-quark p_T reweighting is applied. The associated systematic variations are defined by either omitting the reweighting entirely or applying it twice to the corresponding events.

Identification of b jets

In this analysis, the DeepJet discriminant used for b jet identification is calibrated using shape-dependent corrections. This procedure introduces systematic uncertainties associated with both the purity of the b jet selection and the contamination from light-flavor jets. Additional contributions arise from statistical fluctuations in the determination of the calibration SFs for b and light-flavor jets. No dedicated SFs are measured for c jets. Instead, an uncertainty is assigned based on the b jet SF uncertainty. As the calibration depends on

the jet p_T, dedicated SFs are derived for each JES variation and are consistently applied in the JES uncertainty evaluation.

Pileup

During event simulation, the number of PU interactions is sampled from a Poisson distribution representing the expected PU profile of the data. Since the actual profile is not known at the time of simulation, the simulated events are subsequently reweighted using the measured PU distribution. The associated uncertainty of this method is estimated by varying the assumed inelastic pp cross section by ±4.6 %, following the CMS recommendation, and propagating the resulting effect to all analysis distributions. [93]

Luminosity

All simulated event yields are normalized to the integrated luminosity recorded during the four run periods. Individually, the 2016–2018 integrated luminosities carry uncertainties of 1.2–2.5 % and their combination for Run 2 yields a 1.6 % uncertainty. [66–68]

Background Cross Sections

Each simulated background process is normalized to a cross section derived from theoretical calculations. These cross sections carry uncertainties reflecting the precision of the underlying calculations. To account for this, systematic normalization uncertainties are included, combining contributions from scale variations, the choice of parton distribution functions (PDFs), and the strong coupling constant α_S. The specific values for each background process are 6 % for ttV, 7.5 % for VV and 10 % for VVV.

Statistical Uncertainties

The prediction of each simulated process is limited by the events produced, which affects the sensitivity of the results. To account for this limitation, statistical uncertainties on the simulated processes are introduced following the Barlow–Beeston approach [94]. This approach offers a simple yet robust way of incorporating statistical uncertainties into the model. Its impact is particularly relevant for this analysis, since the signal is concentrated in only a few bins where the background contribution is small. In this approach, each bin is assigned a Gaussian nuisance parameter that allows the predicted yields to fluctuate. The amount of fluctuation f in a bin is calculated via:

$$f = n_{\text{tot}} + x \cdot \epsilon_{\text{tot}}, \tag{4.26}$$

while n_{tot} is given by the sum over events of each simulated background process i

$$n_{\text{tot}} = \sum_{i}^{n} n_i. \tag{4.27}$$

The uncertainty ϵ_i for a given process is calculated via the quadratic sum of the event weights w_j:

$$\epsilon_i = \sqrt{\sum_j^{l_i} w_{i,j}^2}, \tag{4.28}$$

where l_i is the number of events from process i. From this, the total uncertainty ϵ_{tot} is given by the quadratic sum of all individual uncertainties:

$$\epsilon_{\text{tot}} = \sqrt{\sum_i^n \epsilon_i^2}. \tag{4.29}$$

Finally, the parameter x is determined by the fit.

Uncertainties specific to the Signal

Systematic uncertainties from the simulation of signal events are propagated to the signal prediction in the statistical model. These mainly originate from the limited precision of the matrix element (ME) calculation for the hard scattering processes. Two main sources are considered.

The first source is related to the choice of PDFs. Signal events are generated using the NNPDF3.1 set [77], which contains about 100 individual PDF replicas with varied parameters within their uncertainties. The nominal PDF is the mean of these replicas. Event weights are computed for each replica, and the standard deviation of these weights defines the PDF uncertainty.

The second source is associated with the renormalization (μ_R) and factorization (μ_F) scales used in the ME calculation. In `MadGraph5_aMC@NLO`, both scales are varied by factors of 2 and 0.5 to obtain up and down variations. The nominal choice is dynamically set for each event as

$$\mu_R = \mu_F = \sum_i m_{T,i}, \tag{4.30}$$

where $m_{T,i}$ denotes the transverse mass of each final state particle i. The envelope of the resulting distributions is then taken as the variation for the signal processes.

Uncertainties on the F_F method

Several systematic uncertainties influence the prediction of the reducible background. The first source arises from the estimation of the F_F^i in the DR_i whose topology differs from that of the SR, leading to a different background composition. In the $\ell\tau_h\tau_h$ final states, the background is predominantly composed of W+jets and Drell–Yan, similar to the composition in the DR. In the $\ell\ell\tau_h$ final states, the reducible background also contains a significant contribution from tt events. To account for these differences in composition between the measurement and signal regions, a 20 % yield uncertainty is applied. This uncertainty is fully correlated across run periods, as it reflects a systematic effect, but is uncorrelated between final states due to the fact that the background composition depends on the final state.

The second source of uncertainty originates from the limited statistics in the DR_i used to measure the F_F^i. To account for this, the F_F^i are varied up and down within their statistical uncertainties that can be seen in Figures 4.9 and 4.10. This variation is performed independently in each bin, resulting in shape-dependent uncertainties, since they alter all distributions in the SR_i in a non-uniform way.

Another systematic uncertainty arises from the subtraction of processes modeled by simulation during the F_F^i estimation, like VV or VVV. The prompt background contribution is varied by ±10 %, and the F_F^i for electron, muon, and τ_h are recalculated accordingly. This uncertainty is motivated by the simulated background cross section uncertainties, which are 10 % at most. This uncertainty is shape-dependent, as its impact is more pronounced at high electron and muon p_T.

In the $\ell\ell\tau_\mathrm{h}$ final states, a rate uncertainty of 3.5 % is assigned to the m_T selection requirement to increase the purity of the DR_i, described in Section 4.2.1. This accounts for variations in the F_F^i when changing the cut value. The uncertainty is determined by varying the m_T threshold from the nominal 40 GeV to 35 GeV and 45 GeV. Across all run periods and final states the F_F^i differ by 3.5 % from the nominal value at most. The uncertainty is taken as fully correlated between run periods and $\ell\ell\tau_\mathrm{h}$ final states.

Finally, a set of shape uncertainties is introduced to account for discrepancies between data and the F_F background prediction in a signal-like control region. These discrepancies were discovered during the GoF test procedure described in Section 4.3.2. Here two variables, which are highly relevant to the NN categorization, the (leading) light lepton p_T and $p_\mathrm{T}^\mathrm{miss}$, failed the GoF tests in multiple run periods and final states. To address the dis-agreement, a control region is introduced by requiring events to pass the loose but fail the medium DeepTau WP against jets. The NN signal category in this control region provides the most reliable estimate of the closure of the F_F method in the NN signal region. Dedicated F_F^i have been calculated for this region. These uncertainties are evaluated in the $p_\mathrm{T}^\mathrm{miss}$ and (leading) light lepton p_T distributions, separately for the $\ell\ell\tau_\mathrm{h}$ and $\ell\tau_\mathrm{h}\tau_\mathrm{h}$ final states. The distributions are shown in Figure 4.24. All simulated background contributions are subtracted from the data, and the ratio of the remaining data yield to the jet fake estimate is taken as the uncertainty. The 2016 run periods are combined to improve the statistical precision.

4.4.3. Results

Prior to extracting the POIs $\sigma(\mathrm{W^+H})$, $\sigma(\mathrm{W^-H})$, $\sigma(\mathrm{WH})$, and A, the 48 NN output distributions y_i that enter the fit are revalidated using GoF tests, as described in Section 4.3.1. All 48 distributions pass the GoF tests, showing that the good results obtained by the GoF tests of the input space translate to the NN output. As shown in Figure 4.25, only three distributions have values in the range $p = 5 - 10$ %, while for the remaining results it holds $p > 10$ %.

The best-fit values $\hat{\mu}_j, \hat{\vec{\theta}}$ are obtained by maximizing the likelihood in Equation 4.22. Figure 4.26 shows the fitted distributions of y_i in the $\ell\ell\tau_\mathrm{h}$ final state, while Figure 4.27 displays the corresponding distributions for the $\ell\tau_\mathrm{h}\tau_\mathrm{h}$ final state. The combined fit of both

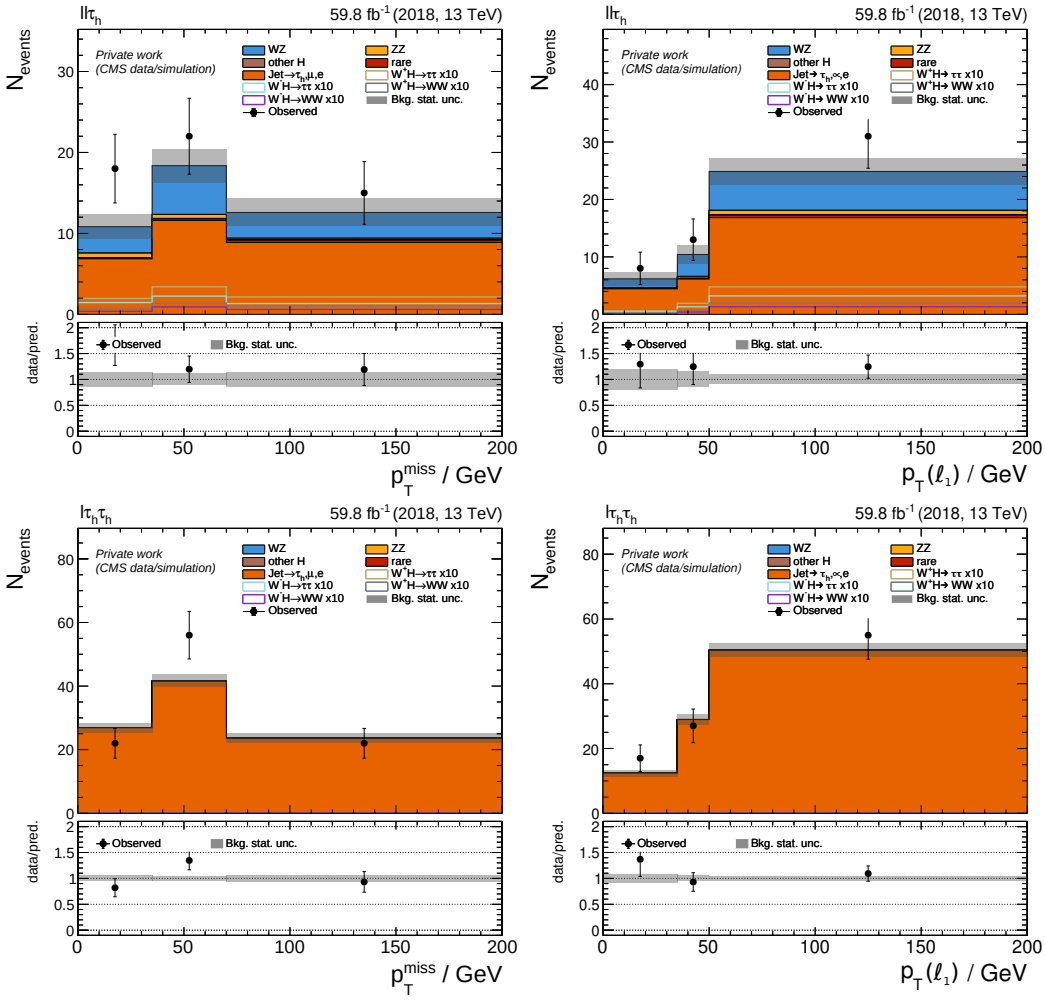

Figure 4.24.: Distributions of p_T^{miss} (left) and the (leading) light lepton p_T (right) of the $\ell\ell\tau_h$ (top) and $\ell\tau_h\tau_h$ (bottom) final states in the 2018 run period. The events are selected in a phase space very similar to the NN signal region, with the only difference being the DeepTau against jets WP.

final states is presented in Figure 4.28. For presentation purposes the distributions of all individual run periods have been combined into the full Run 2 dataset.

In the background categories, the agreement between data and simulation after the fit is excellent for both final states. In the signal categories, however, differences between the final states appear. The W^+H signal is observed in both the $\ell\ell\tau_h$ and $\ell\tau_h\tau_h$, while a W^-H signal is only present in the $\ell\ell\tau_h$ final state. Consequently, in the combined fit, a W^+H, but no W^-H contribution is found.

The measured values integrated over both final states and the full Run 2 dataset are summarized in Table 4.7. All results are compatible with the SM prediction within two standard deviations. As already suggested by the distributions, no W^-H signal is observed. Instead, the best-fit value of $\mu(W^-H)$ is negative and thus outside its physical boundaries. This is not problematic in itself, as the fit result still agrees with the SM expectation within the given uncertainties. However, the negative best-fit of $\mu(W^-H)$ impacts the

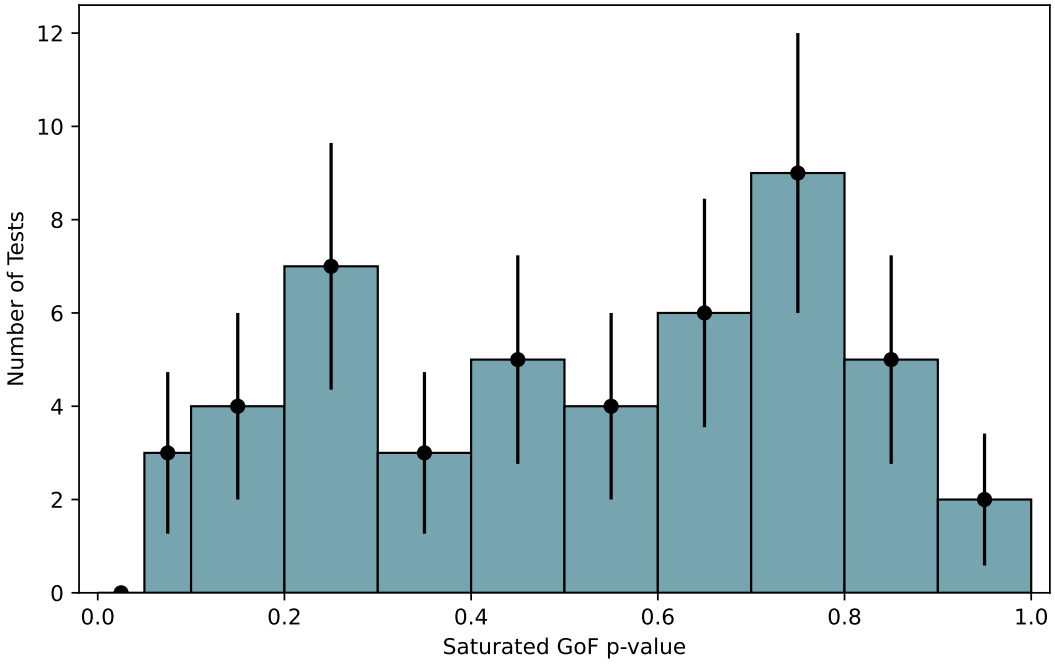

Figure 4.25.: GoF test results of the y_i distributions used for the extraction of the signal. In total, 48 y_i distributions are tested, resulting from three NN categories split by charge for two final states in four run periods. All categories yield results above $p = 5\,\%$ and therefore pass the test, showing the good modeling of the data by the estimation.

measurement of A. From the definition in Equation 2.13, A can take large values if the denominator is small, which is the case in the analysis due to the negative yield of W^-H. As a result, A is measured outside its physical boundaries ($A \in [-1, 1]$), including the upper uncertainty. This behavior is illustrated in the profile likelihood scans, which are used to derive the 68 % confidence intervals. In this procedure, the likelihood is evaluated as a function of a single POI μ_j, while all other signal parameters and nuisance parameters are fixed to the values that maximize the likelihood for the given μ_j. These values are denoted as $\{\hat{\vec{\mu}}_{\text{others}}, \hat{\vec{\theta}}\}$. The boundaries of the 68 % confidence interval are then defined by the parameter values μ_j that satisfy the condition

$$-2\,\Delta \ln \mathrm{L}(\mu_j) = 1, \qquad \text{with} \quad \Delta \ln \mathrm{L}(\mu_j) := \ln \frac{\mathcal{L}(\mu_j, \hat{\vec{\mu}}_{\text{others}}, \hat{\vec{\theta}})}{\mathcal{L}(\hat{\vec{\mu}}, \hat{\vec{\theta}})}. \tag{4.31}$$

This criterion corresponds to the standard 1-σ confidence interval under the asymptotic approximation, where the likelihood ratio test statistic is assumed to follow a χ^2 distribution. The 1D profile likelihood scans of A and $\sigma(\mathrm{WH})$, when used in the same fit model are given in Figure 4.29. When scanning A while profiling all other parameters—including $\sigma(\mathrm{WH})$—the profile departs significantly from a simple quadratic function. Since $\sigma(\mathrm{WH})$ is the denominator of A, the shape gets bent for $\sigma(\mathrm{WH}) \to 0\,\mathrm{pb}$, and an asymptotic behavior

Table 4.7.: The measured and expected values for the cross sections and signal strengths of W^+H, W^-H, and WH production, as well as A. The quoted uncertainties include both statistical and systematic contributions. For the cross sections and A the theoretical predictions and their uncertainties are given as well [43]. A and $\sigma(W^-H)$ are measured outside their physical boundaries. For A, the upper uncertainty is not reported because the fit reaches the boundary of the allowed parameter space. Taken from [65].

Quantity	Observed	Expected	Theory
$\sigma(W^+H)$ [pb]	$0.96^{+0.61}_{-0.58}$	$0.83^{+0.61}_{-0.58}$	0.83 ± 0.02
$\sigma(W^-H)$ [pb]	$-0.05^{+0.46}_{-0.44}$	$0.53^{+0.51}_{-0.49}$	0.53 ± 0.01
$\sigma(WH)$ [pb]	$0.96^{+0.86}_{-0.82}$	$1.36^{+0.90}_{-0.84}$	1.36 ± 0.03
A	$1.18^{+0.00}_{-0.75}$	$0.22^{+0.66}_{-0.56}$	0.22 ± 0.01
$\mu(W^+H)$	$1.16^{+0.74}_{-0.70}$	$1.00^{+0.73}_{-0.69}$	
$\mu(W^-H)$	$-0.15^{+0.87}_{-0.83}$	$1.00^{+0.96}_{-0.91}$	
$\mu(WH)$	$0.71^{+0.63}_{-0.60}$	$1.00^{+0.65}_{-0.62}$	

emerges, leading to very large uncertainties in the positive direction when $\sigma(WH)$ is allowed to float. By contrast, fixing $\sigma(WH)$ to its best-fit value removes the degeneracy, and the resulting 1D scan of A exhibits the expected near-parabolic behavior around the minimum. The 1D scan of $\sigma(WH)$ shows a visible feature at the physical boundary $\sigma(WH) = 0\,\text{pb}$. At that point A is not defined. In the fit model the signal contribution vanishes, and the likelihood reduces to the background-only model, which can be seen in Equations 4.24 and 4.25. Since A drops out entirely when at the boundary, the profiled curves with A floated or fixed must coincide there and yield the same value of $-2\Delta \ln L$.

These characteristics carry over to the 2D scan in the $A - \sigma(WH)$-plane shown on the left in Figure 4.30. Due to the arguments above, open confidence regions are produced: the contours do not close toward large $|A|$ because of the singularity at $\sigma(WH) = 0\,\text{pb}$ and the fact that A does not share the same values approaching $\sigma(WH) = 0\,\text{pb}$ from positive and negative direction. Along the boundary $\sigma(WH) = 0\,\text{pb}$, the surface is flat in A, reflecting again that the fit is effectively background-only there. Close to the singularity, the likelihood becomes highly sensitive to changes in $\sigma(WH)$. The best-fit point and the SM reference are indicated. Overall, the observed non-quadratic A profile, the pronounced peak in the $\sigma(WH)$ scan at the boundary, and the open 2D contours are all consistent with the mathematical structure of the parameterization and the presence of a boundary in $\sigma(WH)$.

The complementary 2D scan performed with the signal strengths for the two charge channels is shown in Fig. 4.30 (right). The contours are elliptical and centered close to the best-fit point, indicating a well-behaved, near-Gaussian likelihood in this parameterization. The tilt of the ellipse reveals a positive correlation between the POIs as expected from

nuisance parameters that scale both charge channels in a similar way (e.g., luminosity or common reconstruction efficiencies). The SM reference lies within the displayed confidence region, showing no significant deviation from SM expectations in either process. Unlike the $A-\sigma(\mathrm{WH})$ scan, no boundary effects are present here, and the contours close smoothly, since both parameters are directly observable rates in the fit model.

To report physically meaningful constraints on A and $\sigma(\mathrm{W^-H})$, we construct 95 % confidence intervals using the Feldman-Cousins (FC) [95] approach. This is required because both parameters are found outside their physical boundaries. The FC construction builds Neyman confidence belts with a likelihood–ratio ordering. For a set of hypothesized true values μ_j (either A or $\sigma(\mathrm{W^-H})$) within the physical region, pseudo-experiments are generated from the full likelihood. For each toy the profile likelihood ratio

$$q_{\mu_j} = -2\Delta \ln \mathrm{L}(\mu_j) \;=\; -2 \ln \frac{\mathcal{L}\left(\mu_j, \hat{\hat{\vec{\theta}}}(\mu_j)\right)}{\mathcal{L}\left(\hat{\mu}_j, \hat{\vec{\theta}}\right)} \tag{4.32}$$

is computed, where $\vec{\theta}$ denotes nuisance parameters, $\hat{\mu}_j, \hat{\vec{\theta}}$ the global maximizers for the particular toy dataset, and $\hat{\hat{\vec{\theta}}}(\mu_j)$ are the profiled values at fixed μ_j. In the FC construction, a critical value $c_{95}(\mu_j)$ for each μ_j is built, which is the 95$^{\text{th}}$ percentile of the toy distribution of q_{μ_j}. Finally, for the reported 95 % confidence interval, the set of μ_j-values is included for which the observed statistic satisfies $q^{\text{obs}}_{\mu_j} \leq c_{95}(\mu_j)$, which is equivalent to $P_{\mu_j} \equiv \mathrm{Prob}[q_{\mu_j} > q^{\text{obs}}_{\mu_j} | \mu_j] \geq 0.05$. In this approach one-sided limits are obtained:

$$\begin{aligned} \sigma(\mathrm{W^-H}) &< 0.88\,\mathrm{pb}, \\ A &> -0.09. \end{aligned} \tag{4.33}$$

In Figure 4.31 this scan in hypothetical values of μ_j with the FC method is shown for A and $\mu(\mathrm{W^-H})$.

The statistical model is probed via nuisance parameter shifts and their impacts on the POIs. For each nuisance parameter θ_k, the shift $(\hat{\theta}_k - \theta_{k,\mathrm{I}})/\sigma_{k,\mathrm{I}}$ with respect to the pre-fit initialization θ_{I} is computed. Large coherent shifts would indicate that the background model must be adjusted to describe the data and many such shifts would point to insatisfactory modeling. Figure 4.32 shows the shift distribution (black dots) for the fit to $\mu(\mathrm{WH})$ for the nuisance parameters that have the highest impact on the fit result. All nuisance parameters are within one standard deviation of the θ_{I}.

To evaluate impacts, two fits for each θ_k are performed: θ_k is fixed to its post-fit value shifted by $\pm\,\sigma_{k,\mathrm{P}}$, while all other nuisance parameters are profiled. The corresponding shifts of the POI μ_j,

$$\Delta\mu^{\pm}_{j,k} = \mu_j\big(\theta_k = \hat{\theta}_k \pm \sigma_{k,\mathrm{P}}\big) \;-\; \hat{\mu}_j, \tag{4.34}$$

define the positive and negative impacts displayed in the impact plot (the bar spans $[\Delta\mu^{-}_{j,k}, \Delta\mu^{+}_{j,k}]$). These impacts identify the nuisances with the largest effect on the measured value and illustrate correlations with the POI. For $\mu(\mathrm{WH})$ the nuisance parameter with the highest impact is related to the uncertainty in the VV cross section followed by uncertainties related to the F_{F} method to estimate the reducible background.

4.5. Towards improved Sensitivity

Several possible developments of this analysis could not be addressed in the scope of this work and are therefore left for future studies. These developments can be divided into technical refinements of the current analysis and broader developments that extend the physics reach of the analysis. The possible technical improvements were all considered as lower priority due to their limited contribution to the sensitivity and not followed in favor of a preliminary publication of the measurements, through the CMS Collaboration [65]. These tasks are:

- The use of double-lepton triggers would lower the p_{T} threshold of the selected light leptons and increase the overall signal acceptance. The expected gain in sensitivity is low.
- Inclusion of di-ℓ final states with opposite charge light leptons and a veto on the Z boson mass window. The expected gain in sensitivity is low.
- For the background modeling, a splitting of the WZ sample by charge would allow for a more precise treatment of asymmetries and their uncertainties.
- Tighter charge reconstruction requirements on light leptons could reduce misreconstruction effects, although this would require new scale factors to be derived.
- The reconstruction of $m(\tau\tau)$ could be improved by using an NN–based estimator, which may provide better resolution and discrimination power.
- The uncertainty model of the light lepton reconstruction, identification, and I_{rel} could be improved. This requires a measurement of the systematic and statistical uncertainties on the SFs derived within the Tag-and-Probe framework. This is work in progress.
- The uncertainty model of the F_{F} method could be refined. The motivation for the uncertainties on the (leading) light lepton p_{T} and $p_{\mathrm{T}}^{\mathrm{miss}}$ is based on failed GoF tests. An introduction of corrections could make those uncertainties obsolete.

Beyond these technical improvements, several broader developments could further enhance the physics reach of the analysis in the future. A natural extension is the inclusion of the ZH process, as the analysis strategy and uncertainty model would be similar. In addition, the measurement could be interpreted within the Simplified Template Cross Section [96] framework and combined with results from other production modes, such as ggF and VBF. In this context, the analysis would need to be differential in $p_{\mathrm{T}}(\mathrm{V})$ and it must be ensured that the phase spaces to analyze the different production modes are orthogonal to each other. Furthermore, an interpretation of the measurement in the context of the charm quark Yukawa coupling would require additional statistical precision and is therefore expected to benefit from the larger datasets of future LHC runs, as well as from combinations with other Higgs boson decay channels, such as WH(WW) and WH($\gamma\gamma$). Such combinations exploit correlations between systematic uncertainties and maximize the statistical power of the dataset.

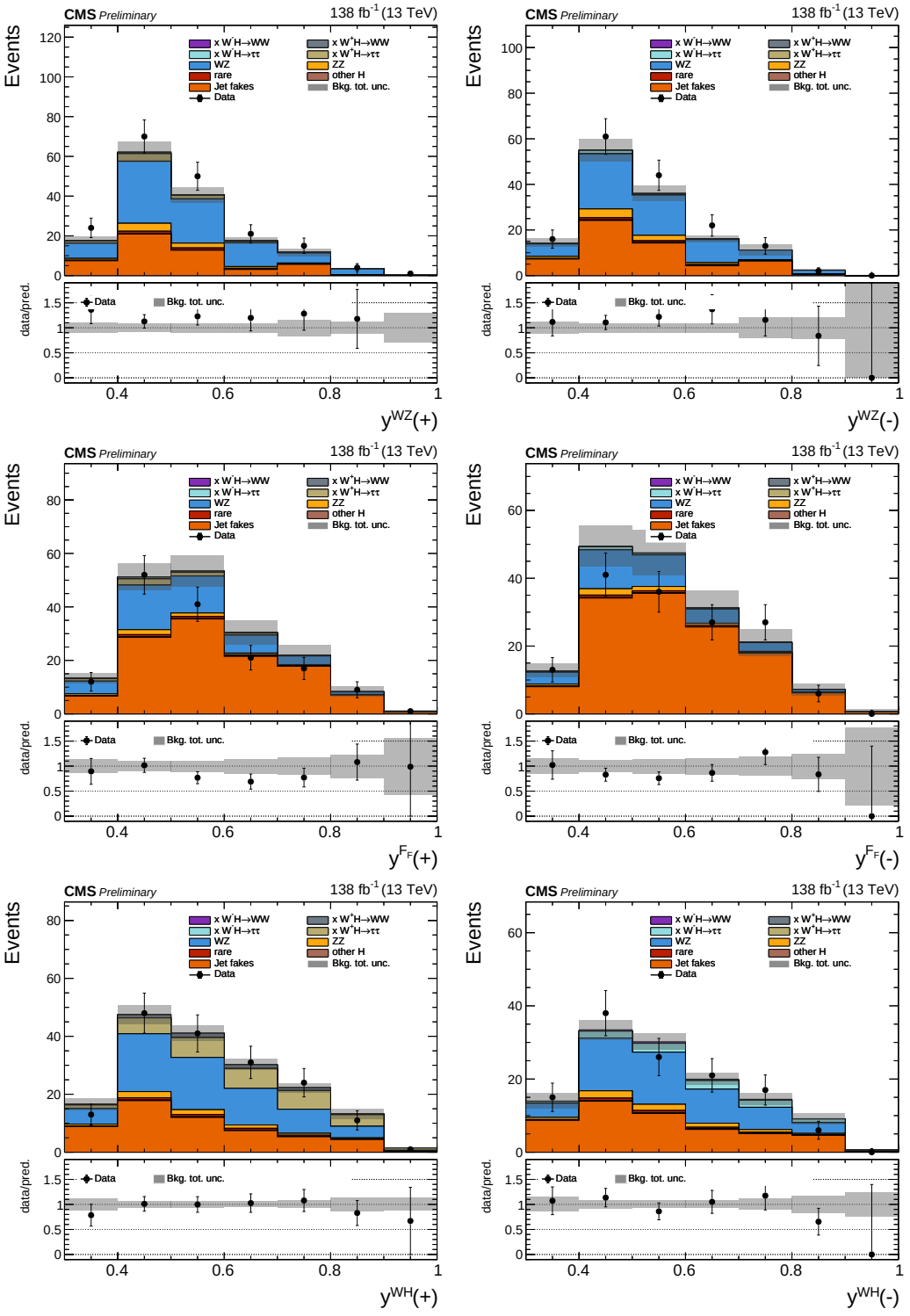

Figure 4.26.: Post-fit distributions of y_i of the three NN output categories split by charge of the light lepton associated with the W boson decay in the $\ell\ell\tau_h$ final state. The gray band corresponds to the post-fit statistical and systematic uncertainties. Taken from [65].

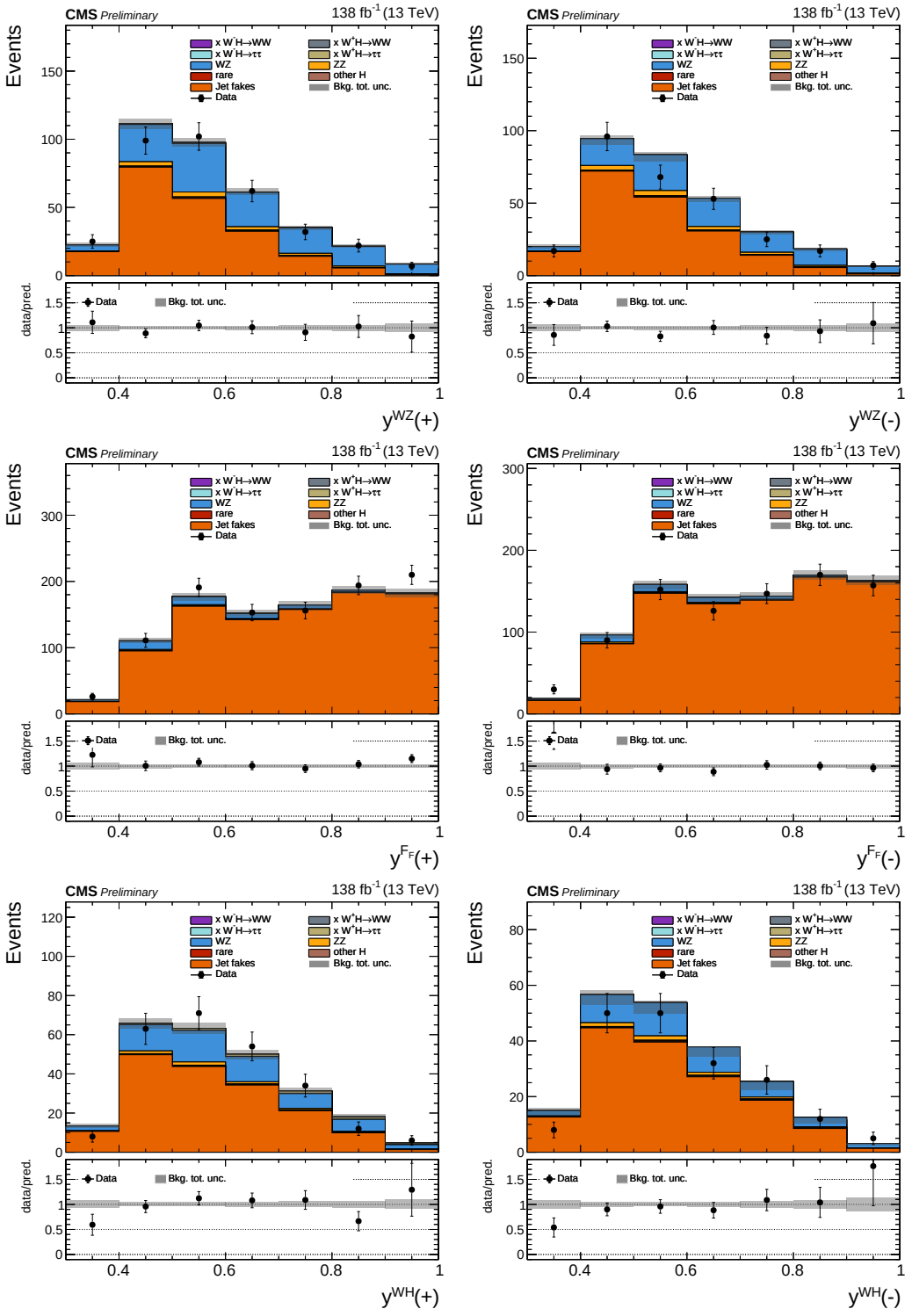

Figure 4.27.: Post-fit distributions of y_i of the three NN output categories split by charge of the light lepton associated with the W boson decay in the $\ell\tau_h\tau_h$ final state. The gray band corresponds to the post-fit statistical and systematic uncertainties. Taken from [65].

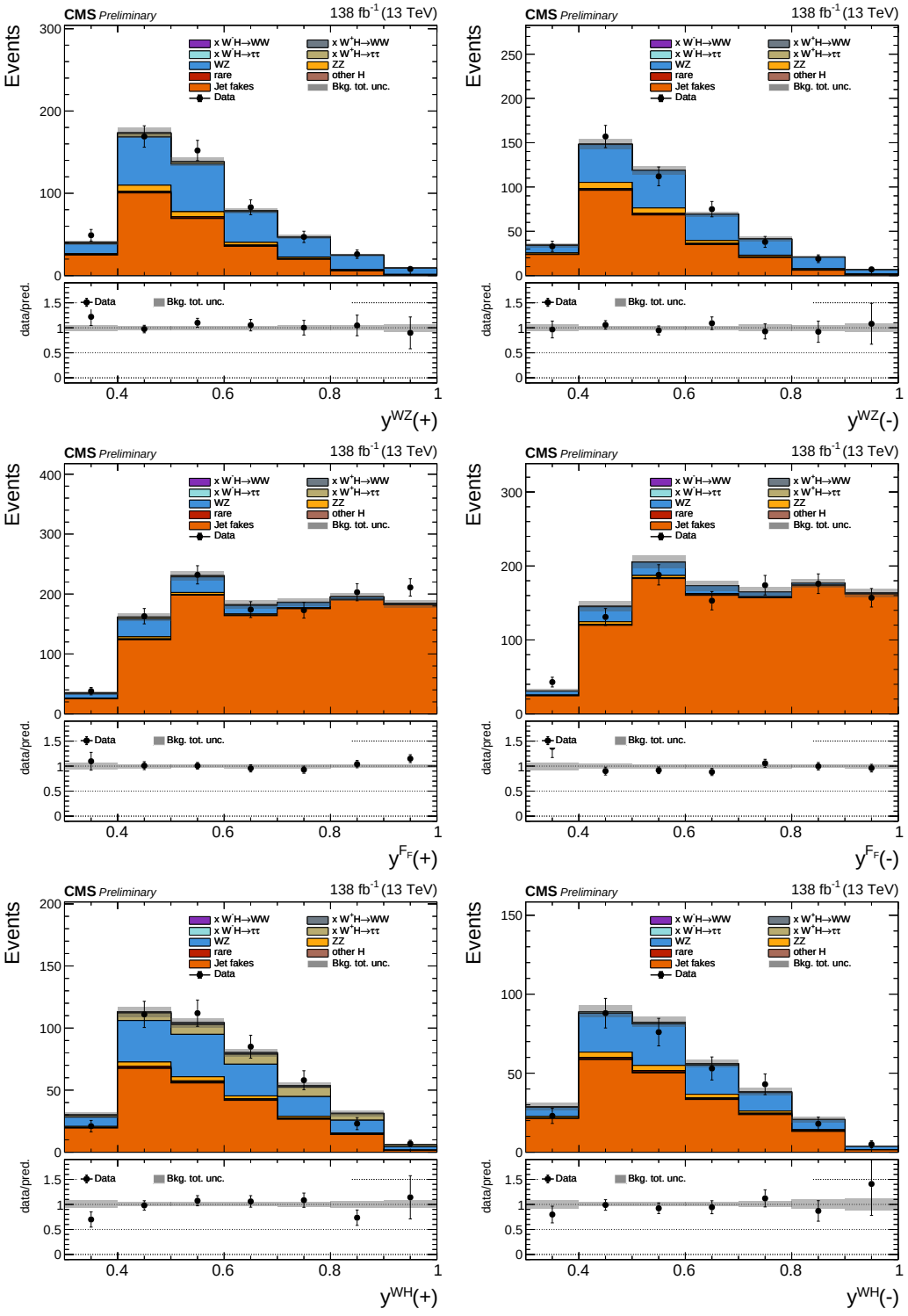

Figure 4.28.: Post-fit distributions of y_i of the three NN output categories split by charge of the W boson decay product candidate integrated over both final states. The gray band corresponds to the post-fit statistical and systematic uncertainties. Taken from [65].

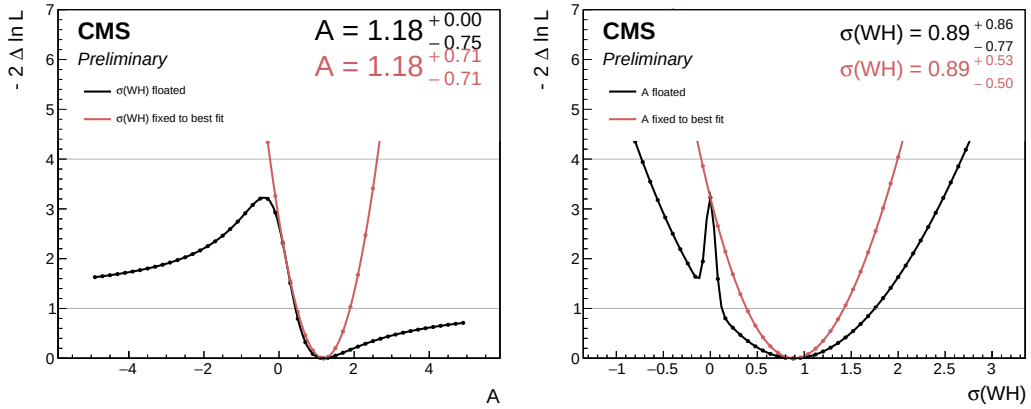

Figure 4.29.: Profile likelihood scan of A (left) and $\sigma(\mathrm{WH})$ (right). Both POIs scanned, either with the other POI fixed or floated. In the latter scenario boundary effects in both scans become visible. In the scan of A, the asymptotic behavior for small $\sigma(\mathrm{WH})$ is present, and in the scan of $\sigma(\mathrm{WH})$, the boundary of $\sigma(\mathrm{WH}) = 0\,\mathrm{pb}$ leads to a pronounced peak. Taken from [65].

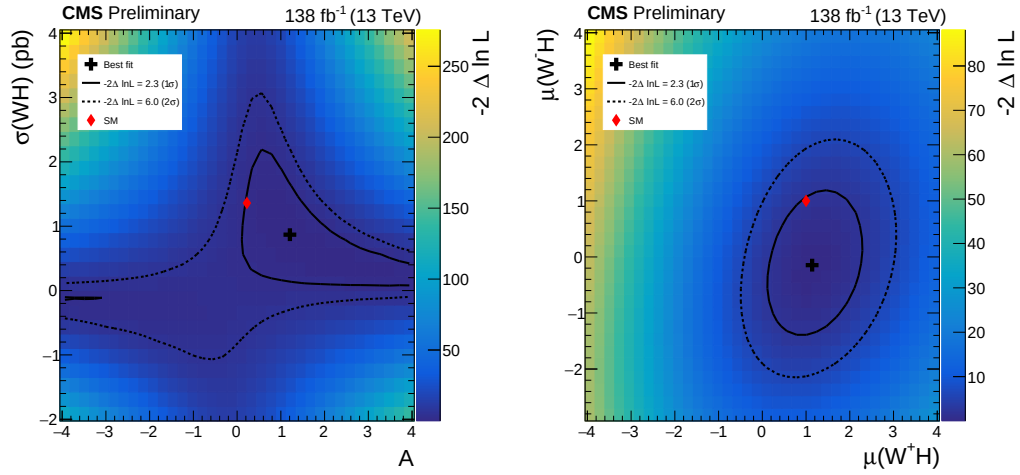

Figure 4.30.: Profile likelihood scans of the 2D fit models used to extract the POIs. On the left the scan for A-$\sigma(\mathrm{WH})$ is showing open contours due to the singularity in A. On the right, the scan for $\mu(\mathrm{W^+H})$-$\mu(\mathrm{W^-H})$ shows an elliptical contour. The best-fit and SM expectation are indicated. Taken from [65].

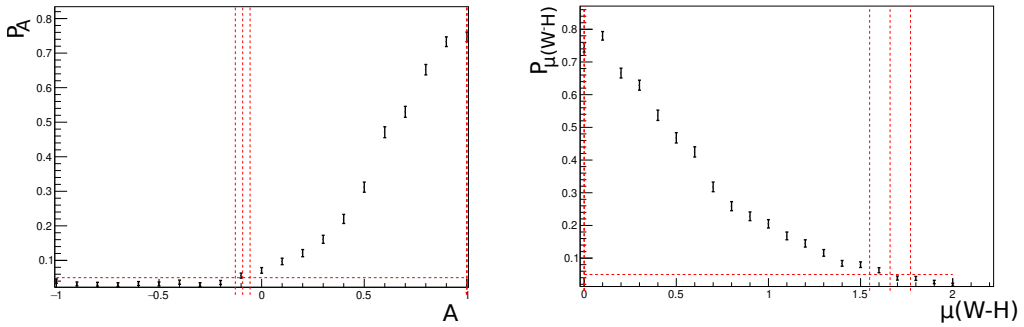

Figure 4.31.: Feldman-Cousins scan to compute confidence intervals for A (left) and $\mu(W^-H)$ (right), which are measured outside their physical boundaries. The y-axis shows $P_{\mu_j} \equiv \text{Prob}[q_{\mu_j} > q^{\text{obs}}_{\mu_j} | \mu_j]$ while the one-sided confidence interval is given by $P_{\mu_j} \geq 0.05$, with $\mu_j \in \{A, \mu(W^-H)\}$. The central vertical red dashed line indicates the nominal result, while the flanking dashed lines illustrate the uncertainty from the finite number of toy experiments.

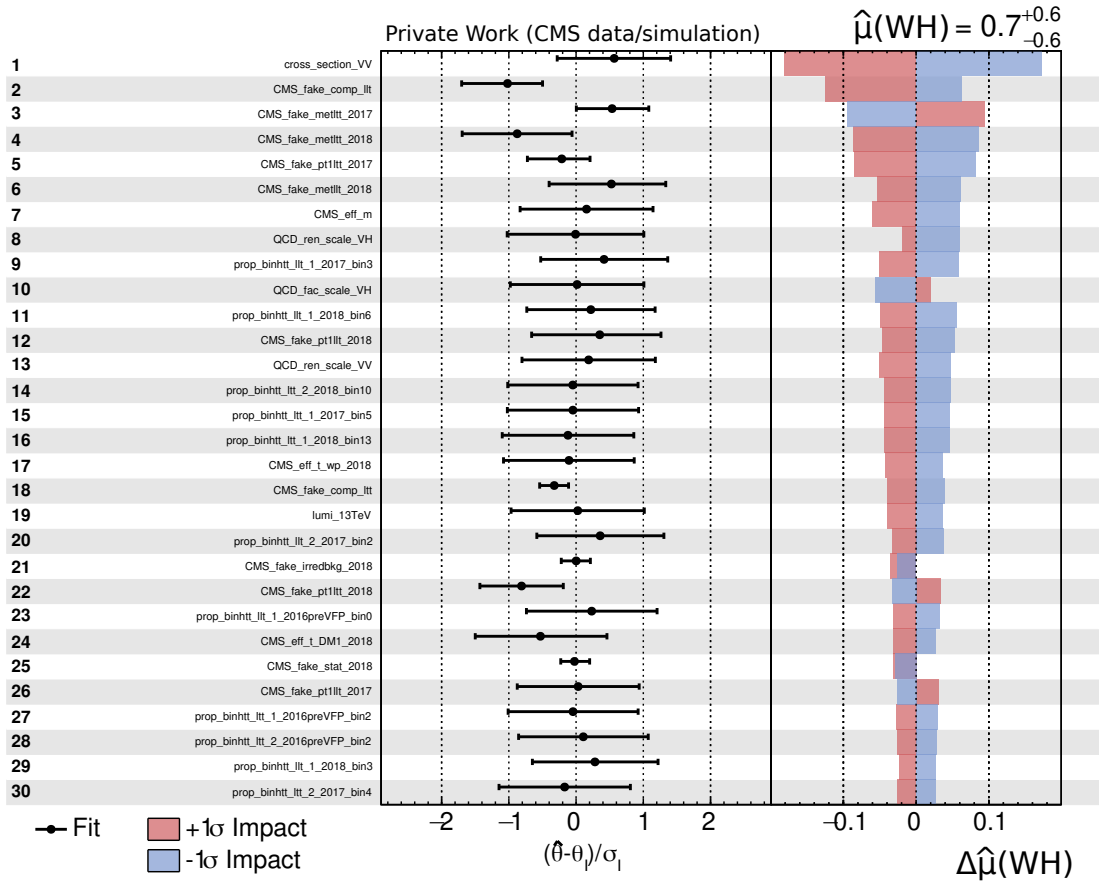

Figure 4.32.: Best-fit shifts and impacts of the most impactful nuisance parameters on the result of $\mu(WH)$. The black dots show the shifts $(\hat{\theta}-\theta_I)/\sigma_I$. The impacts of the individual nuisances are shown in the right column and calculated by keeping a single nuisance parameter fixed while profiling the others. The change in the POI defines the impact. The rounded result on the top corresponds to the result reported in Table 4.7.

5. Summary and Outlook

The Run 2 of the LHC has provided an unprecedented opportunity to study the properties of the Higgs boson in great detail. With the complete CMS dataset with an integrated luminosity of 138 fb^{-1} collected between 2016 and 2018, a measurement of the production cross sections and charge asymmetry of the associated WH process has been performed in the H$\rightarrow \tau\tau$ final state. The analysis focused on final states with at least one of the τ leptons decaying hadronically, and the associated W boson decaying into an electron or a muon.

The selected events were classified using a neural network into signal- and background-enriched categories. With extensive studies, the data description of the neural net input variables was studied. Each distribution was validated through goodness-of-fit tests, considering both one-dimensional and two-dimensional distributions. This procedure ensures that the background estimation provides an accurate description of the data within the assigned uncertainties. Special attention was given to variables with high discriminating power, where systematic effects could most strongly bias the classification. The validation confirmed that the chosen set of input features is robust and suitable for the event classification, thereby minimizing the risk of model-induced biases in the final measurement.

A simultaneous fit to the resulting categories allowed for the extraction of the cross section of the inclusive WH process, as well as the first measurements of $\mathrm{W^+H}$, $\mathrm{W^-H}$ and the associated charge asymmetry A. In the background-dominated categories, excellent agreement between data and the prediction was achieved, and uncertainties related to major background processes could be constrained. Backgrounds arising from jets misidentified as light leptons or hadronic τ lepton decays are estimated with the F_F method. This data-driven technique uses control regions enriched in misidentified objects to measure the probability of a jet being reconstructed as a light lepton or a hadroncially decaying τ lepton. The measured fake rates are then applied to events in the application regions to predict the jet-induced background in the signal regions. This reduces the reliance on simulation and provides a more accurate description of beam conditions and detector performance. In the signal categories, sensitivity to the separate production modes was obtained, leading to the independent measurement of the charge-dependent cross sections and their asymmetry. All results were found to be compatible with the Standard Model within uncertainties.

The presented measurement demonstrates that charge-sensitive observables in associated Higgs boson production can be probed with the current LHC data. The charge asymmetry provides a handle on the charm Yukawa coupling complementary to direct H $\rightarrow$ cc searches. This makes it a promising strategy for future analyses with larger datasets.

A natural next step beyond this work is the combination of the analysis with the complementary H $\rightarrow$ WW analysis. Both analyses share a similar final-state topology.

Their combination will increase the statistical power and help constrain systematic uncertainties more effectively. Furthermore, the Run 3 of the LHC is expected to deliver more than twice as much data compared to Run 2 at a higher center-of-mass energy of 13.6 TeV. The inclusion of this dataset will significantly improve the precision of the measurement and will allow for an enhanced sensitivity to possible deviations from the Standard Model, in particular in the study of charge asymmetry and charm quark Yukawa coupling effects.

Bibliography

[1] F. Englert and R. Brout. Broken Symmetry and the Mass of Gauge Vector Mesons. *Phys. Rev. Lett.* 13 (1964), p. 321. DOI: 10.1103/PhysRevLett.13.321.

[2] Peter W. Higgs. Broken symmetries, massless particles and gauge fields. *Phys. Lett.* 12 (1964), p. 132. DOI: 10.1016/0031-9163(64)91136-9.

[3] Peter W. Higgs. Broken Symmetries and the Masses of Gauge Bosons. *Phys. Rev. Lett.* 13 (1964), p. 508. DOI: 10.1103/PhysRevLett.13.508.

[4] G. S. Guralnik, C. R. Hagen, and T. W. B. Kibble. Global Conservation Laws and Massless Particles. *Phys. Rev. Lett.* 13 (1964), p. 585. DOI: 10.1103/PhysRevLett.13.585.

[5] Peter W. Higgs. Spontaneous Symmetry Breakdown without Massless Bosons. *Phys. Rev.* 145 (1966), p. 1156. DOI: 10.1103/PhysRev.145.1156.

[6] T. W. B. Kibble. Symmetry breaking in non-abelian gauge theories. *Phys. Rev.* 155 (1967), p. 1554. DOI: 10.1103/PhysRev.155.1554.

[7] The ATLAS Collaboration. The ATLAS Experiment at the CERN Large Hadron Collider. *Journal of Instrumentation* 3.08 (Aug. 2008), S08003. DOI: 10.1088/1748-0221/3/08/S08003. URL: https://dx.doi.org/10.1088/1748-0221/3/08/S08003.

[8] The CMS Collaboration. The CMS experiment at the CERN LHC. *Journal of Instrumentation* 3.08 (Aug. 2008), S08004. DOI: 10.1088/1748-0221/3/08/S08004. URL: https://dx.doi.org/10.1088/1748-0221/3/08/S08004.

[9] Lyndon Evans and Philip Bryant. LHC Machine. *Journal of Instrumentation* 3.08 (Aug. 2008), S08001. DOI: 10.1088/1748-0221/3/08/S08001. URL: https://dx.doi.org/10.1088/1748-0221/3/08/S08001.

[10] The CMS Collaboration. Observation of a new boson at a mass of 125 GeV with the CMS experiment at the LHC. *Physics Letters B* 716.1 (2012), pp. 30–61. DOI: https://doi.org/10.1016/j.physletb.2012.08.021. URL: https://www.sciencedirect.com/science/article/pii/S0370269312008581.

[11] The ATLAS Collaboration. Observation of a new particle in the search for the Standard Model Higgs boson with the ATLAS detector at the LHC. *Physics Letters B* 716.1 (2012), pp. 1–29. DOI: https://doi.org/10.1016/j.physletb.2012.08.020. URL: https://www.sciencedirect.com/science/article/pii/S037026931200857X.

[12] The CMS Collaboration. Measurement of the inclusive and differential Higgs boson production cross sections in the leptonic WW decay mode at $\sqrt{s} = 13$ TeV. *JHEP* 03 (2021), p. 003. DOI: 10.1007/JHEP03(2021)003. arXiv: 2007.01984 [hep-ex].

[13] The ATLAS Collaboration. Measurements of differential cross sections of Higgs boson production through gluon fusion in the $H \to WW^* \to e\nu\mu\nu$ final state at $\sqrt{s}$ = 13 TeV with the ATLAS detector. *Eur. Phys. J. C* 83 (2023), p. 774. DOI: 10.1140/epjc/s10052-023-11873-5. arXiv: 2301.06822 [hep-ex].

[14] The ATLAS Collaboration. Integrated and differential fiducial cross-section measurements for the vector boson fusion production of the Higgs boson in the $H \to WW^* \to e\nu\mu\nu$ decay channel at 13 TeV with the ATLAS detector. *Phys. Rev. D* 108 (2023), p. 072003. DOI: 10.1103/PhysRevD.108.072003. arXiv: 2304.03053 [hep-ex].

[15] The CMS Collaboration. Measurements of inclusive and differential cross sections for the Higgs boson production and decay to four-leptons in proton-proton collisions at $\sqrt{s}$ = 13 TeV. *JHEP* 08 (2023), p. 040. DOI: 10.1007/JHEP08(2023)040. arXiv: 2305.07532 [hep-ex].

[16] The ATLAS Collaboration. Higgs boson production cross-section measurements and their EFT interpretation in the 4ℓ decay channel at $\sqrt{s}$ =13 TeV with the ATLAS detector. *Eur. Phys. J. C* 80 (2020). [Erratum: Eur.Phys.J.C 81, 29 (2021), Erratum: Eur.Phys.J.C 81, 398 (2021)], p. 957. DOI: 10.1140/epjc/s10052-020-8227-9. arXiv: 2004.03447 [hep-ex].

[17] The ATLAS Collaboration. Measurements of the Higgs boson inclusive and differential fiducial cross sections in the 4ℓ decay channel at $\sqrt{s}$ = 13 TeV. *Eur. Phys. J. C* 80 (2020), p. 942. DOI: 10.1140/epjc/s10052-020-8223-0. arXiv: 2004.03969 [hep-ex].

[18] The CMS Collaboration. Measurement of the Higgs boson inclusive and differential fiducial production cross sections in the diphoton decay channel with pp collisions at $\sqrt{s}$ = 13 TeV. *JHEP* 07 (2023), p. 091. DOI: 10.1007/JHEP07(2023)091. arXiv: 2208.12279 [hep-ex].

[19] The ATLAS Collaboration. Measurement of the $H \to \gamma\gamma$ and $H \to ZZ^* \to 4\ell$ cross-sections in pp collisions at $\sqrt{s}$ = 13.6 TeV with the ATLAS detector. *Eur. Phys. J. C* 84 (2024), p. 78. DOI: 10.1140/epjc/s10052-023-12130-5. arXiv: 2306.11379 [hep-ex].

[20] The CMS Collaboration. Measurement of simplified template cross sections of the Higgs boson produced in association with W or Z bosons in the H → bb decay channel in proton-proton collisions at s=13 TeV. *Phys. Rev. D* 109 (2024), p. 092011. DOI: 10.1103/PhysRevD.109.092011. arXiv: 2312.07562 [hep-ex].

[21] The ATLAS Collaboration. Measurements of WH and ZH production with Higgs boson decays into bottom quarks and direct constraints on the charm Yukawa coupling in 13 TeV pp collisions with the ATLAS detector. *Journal of High Energy Physics* 2025.4 (Apr. 2025). DOI: 10.1007/jhep04(2025)075. URL: http://dx.doi.org/10.1007/JHEP04(2025)075.

[22] The CMS Collaboration. Measurements of $t\bar{t}H$ Production and the CP Structure of the Yukawa Interaction between the Higgs Boson and Top Quark in the Diphoton Decay Channel. *Phys. Rev. Lett.* 125 (2020), p. 061801. DOI: 10.1103/PhysRevLett.125.061801. arXiv: 2003.10866 [hep-ex].

[23] The CMS Collaboration. Measurement of the Higgs boson production rate in association with top quarks in final states with electrons, muons, and hadronically decaying tau leptons at $\sqrt{s} = 13$ TeV. *Eur. Phys. J. C* 81 (2021), p. 378. DOI: 10.1140/epjc/s10052-021-09014-x. arXiv: 2011.03652 [hep-ex].

[24] The ATLAS Collaboration. Observation of Higgs boson production in association with a top quark pair at the LHC with the ATLAS detector. *Phys. Lett. B* 784 (2018), p. 173. DOI: 10.1016/j.physletb.2018.07.035. arXiv: 1806.00425 [hep-ex].

[25] Measurement of the associated production of a top-antitop-quark pair and a Higgs boson decaying into a $b\bar{b}$ pair in pp collisions at $\sqrt{s} = 13$ TeV using the ATLAS detector at the LHC. *The European Physical Journal C* 85.2 (Feb. 2025). DOI: 10.1140/epjc/s10052-025-13740-x. URL: http://dx.doi.org/10.1140/epjc/s10052-025-13740-x.

[26] The CMS Collaboration. Measurements of Higgs boson production in the decay channel with a pair of τ leptons in proton–proton collisions at $\sqrt{s} = 13$ TeV. *Eur. Phys. J. C* 83 (2023), p. 562. DOI: 10.1140/epjc/s10052-023-11452-8. arXiv: 2204.12957 [hep-ex].

[27] Differential cross-section measurements of Higgs boson production in the $H \to \tau^+\tau^-$ decay channel in pp collisions at $\sqrt{s} = 13$ TeV with the ATLAS detector. *Journal of High Energy Physics* 2025.3 (Mar. 2025). DOI: 10.1007/jhep03(2025)010. URL: http://dx.doi.org/10.1007/JHEP03(2025)010.

[28] Albert M Sirunyan et al. Evidence for Higgs boson decay to a pair of muons. *JHEP* 01 (2021), p. 148. DOI: 10.1007/JHEP01(2021)148. arXiv: 2009.04363 [hep-ex].

[29] ATLAS Collaboration. Evidence for the dimuon decay of the Higgs boson in pp collisions with the ATLAS detector. 2025. arXiv: 2507.03595 [hep-ex]. URL: https://arxiv.org/abs/2507.03595.

[30] The CMS Collaboration. Search for Higgs Boson Decay to a Charm Quark-Antiquark Pair in Proton-Proton Collisions at s=13 TeV. *Phys. Rev. Lett.* 131 (2023), p. 061801. DOI: 10.1103/PhysRevLett.131.061801. arXiv: 2205.05550 [hep-ex].

[31] The CMS Collaboration. Search for Higgs Boson and Observation of Z Boson through their Decay into a Charm Quark-Antiquark Pair in Boosted Topologies in Proton-Proton Collisions at s=13 TeV. *Phys. Rev. Lett.* 131 (2023), p. 041801. DOI: 10.1103/PhysRevLett.131.041801. arXiv: 2211.14181 [hep-ex].

[32] The CMS Collaboration. Search for Higgs boson decay to a charm quark-antiquark pair via ttH production. Tech. rep. Geneva: CERN, 2025. URL: https://cds.cern.ch/record/2929444.

[33] The ATLAS Collaboration. Direct constraint on the Higgs-charm coupling from a search for Higgs boson decays into charm quarks with the ATLAS detector. *Eur. Phys. J. C* 82 (2022), p. 717. DOI: 10.1140/epjc/s10052-022-10588-3. arXiv: 2201.11428 [hep-ex].

[34] S. L. Glashow. Partial-symmetries of weak interactions. *Nuclear Physics* 22.4 (1961), pp. 579–588. DOI: https://doi.org/10.1016/0029-5582(61)90469-2. URL: https://www.sciencedirect.com/science/article/pii/0029558261904692.

[35] A. Salam and J.C. Ward. Electromagnetic and weak interactions. *Physics Letters* 13.2 (1964), pp. 168–171. DOI: https://doi.org/10.1016/0031-9163(64)90711-5. URL: https://www.sciencedirect.com/science/article/pii/0031916364907115.

[36] S. Weinberg. A Model of Leptons. *Phys. Rev. Lett.* 19 (21 Nov. 1967), pp. 1264–1266. DOI: 10.1103/PhysRevLett.19.1264. URL: https://link.aps.org/doi/10.1103/PhysRevLett.19.1264.

[37] Wikipedia. Standard Model of Particle Physics. https://en.wikipedia.org/wiki/File:Standard_Model_of_Elementary_Particles.svg. Accessed: 2025-05-15. 2025.

[38] CERN. CERN Yellow Reports: Monographs, Vol 2 (2017): Handbook of LHC Higgs cross sections: 4. Deciphering the nature of the Higgs sector. en. 2017. DOI: 10.23731/CYRM-2017-002. URL: https://e-publishing.cern.ch/index.php/CYRM/issue/view/32.

[39] CMS Collaboration. Search for Higgs Boson Decay to a Charm Quark-Antiquark Pair in Proton-Proton Collisions at s=13 TeV. *Phys. Rev. Lett.* 131 (2023), p. 061801. DOI: 10.1103/PhysRevLett.131.061801. arXiv: 2205.05550 [hep-ex].

[40] CMS Collaboration. Search for Higgs Boson and Observation of Z Boson through their Decay into a Charm Quark-Antiquark Pair in Boosted Topologies in Proton-Proton Collisions at s=13 TeV. *Phys. Rev. Lett.* 131 (2023), p. 041801. DOI: 10.1103/PhysRevLett.131.041801. arXiv: 2211.14181 [hep-ex].

[41] CMS Collaboration. Search for Higgs boson decay to a charm quark-antiquark pair via ttH production. Tech. rep. Geneva: CERN, 2025. URL: https://cds.cern.ch/record/2929444.

[42] ATLAS Collaboration. Direct constraint on the Higgs-charm coupling from a search for Higgs boson decays into charm quarks with the ATLAS detector. *Eur. Phys. J. C* 82 (2022), p. 717. DOI: 10.1140/epjc/s10052-022-10588-3. arXiv: 2201.11428 [hep-ex].

[43] LHC Higgs Cross Section Working Group. Handbook of LHC Higgs cross sections: 4. Deciphering the nature of the Higgs sector. CERN Report CERN-2017-002-M. 2016. DOI: 10.23731/CYRM-2017-002. arXiv: 1610.07922 [hep-ph].

[44] Felix Yu. Phenomenology of enhanced light quark Yukawa couplings and the W±h charge asymmetry. *Journal of High Energy Physics* 2017.2 (Feb. 2017), p. 83. DOI: 10.1007/JHEP02(2017)083. URL: https://doi.org/10.1007/JHEP02(2017)083.

[45] The ALICE Collaboration. The ALICE experiment at the CERN LHC. *Journal of Instrumentation* 3.08 (Aug. 2008), S08002. DOI: 10.1088/1748-0221/3/08/S08002. URL: https://dx.doi.org/10.1088/1748-0221/3/08/S08002.

[46] The LHCb Collaboration. The LHCb Detector at the LHC. *Journal of Instrumentation* 3.08 (Aug. 2008), S08005. DOI: 10.1088/1748-0221/3/08/S08005. URL: https://dx.doi.org/10.1088/1748-0221/3/08/S08005.

[47] Tai Sakuma and Thomas McCauley. Detector and Event Visualization with SketchUp at the CMS Experiment. *Journal of Physics: Conference Series* 513.2 (June 2014), p. 022032. DOI: 10.1088/1742-6596/513/2/022032. URL: https://dx.doi.org/10.1088/1742-6596/513/2/022032.

[48] Izaak Neutelings. CMS coordinate system. https://tikz.net/axis3d_cms/. Accessed: 2025-07-23.

[49] CMS Collaboration. The CMS Phase-1 pixel detector upgrade. *Journal of Instrumentation* 16.02 (Feb. 2021), P02027. DOI: 10.1088/1748-0221/16/02/P02027. URL: https://dx.doi.org/10.1088/1748-0221/16/02/P02027.

[50] CMS Collaboration. The CMS trigger system. *Journal of Instrumentation* 12.01 (Jan. 2017), P01020. DOI: 10.1088/1748-0221/12/01/P01020. URL: https://dx.doi.org/10.1088/1748-0221/12/01/P01020.

[51] CMS Collaboration. Performance of the CMS Level-1 trigger in proton-proton collisions at $\sqrt{s} = 13$ TeV. *Journal of Instrumentation* 15.10 (Oct. 2020), P10017. DOI: 10.1088/1748-0221/15/10/P10017. URL: https://dx.doi.org/10.1088/1748-0221/15/10/P10017.

[52] CMS Collaboration. Particle-flow reconstruction and global event description with the CMS detector. *Journal of Instrumentation* 12.10 (Oct. 2017), P10003. DOI: 10.1088/1748-0221/12/10/P10003. URL: https://dx.doi.org/10.1088/1748-0221/12/10/P10003.

[53] The CMS Collaboration. Pileup mitigation at CMS in 13 TeV data. *Journal of Instrumentation* 15.09 (Sept. 2020), P09018. DOI: 10.1088/1748-0221/15/09/P09018. URL: https://dx.doi.org/10.1088/1748-0221/15/09/P09018.

[54] The CMS Collaboration. Performance of the CMS muon detector and muon reconstruction with proton-proton collisions at $\sqrt{s}$=13 TeV. *Journal of Instrumentation* 13.06 (June 2018), P06015. DOI: 10.1088/1748-0221/13/06/P06015. URL: https://dx.doi.org/10.1088/1748-0221/13/06/P06015.

[55] The CMS Collaboration. Performance of electron reconstruction and selection with the CMS detector in proton-proton collisions at $\sqrt{s}$=8 TeV. *Journal of Instrumentation* 10.06 (June 2015), P06005. DOI: 10.1088/1748-0221/10/06/P06005. URL: https://dx.doi.org/10.1088/1748-0221/10/06/P06005.

[56] W Adam et al. Reconstruction of electrons with the Gaussian-sum filter in the CMS tracker at the LHC. *Journal of Physics G: Nuclear and Particle Physics* 31.9 (July 2005), N9. DOI: 10.1088/0954-3899/31/9/N01. URL: https://dx.doi.org/10.1088/0954-3899/31/9/N01.

[57] Matteo Cacciari, Gavin P. Salam, and Gregory Soyez. The anti-kt jet clustering algorithm. *JHEP* 04 (2008), p. 063. DOI: 10.1088/1126-6708/2008/04/063. arXiv: 0802.1189 [hep-ex].

[58] The CMS Collaboration. Jet energy scale and resolution in the CMS experiment in pp collisions at 8 TeV. *Journal of Instrumentation* 12.02 (Feb. 2017), P02014. DOI: 10.1088/1748-0221/12/02/P02014. URL: https://dx.doi.org/10.1088/1748-0221/12/02/P02014.

[59] Particle Data Group et al. Review of Particle Physics. *Progress of Theoretical and Experimental Physics* 2022.8 (Aug. 2022), p. 083C01. DOI: 10.1093/ptep/ptac097. eprint: https://academic.oup.com/ptep/article-pdf/2022/8/083C01/49175539/ptac097.pdf. URL: https://doi.org/10.1093/ptep/ptac097.

[60] CMS Collaboration. Performance of reconstruction and identification of τ leptons decaying to hadrons and ν_τ in pp collisions at $\sqrt{s}$=13 TeV. *Journal of Instrumentation* 13.10 (Oct. 2018), P10005. DOI: 10.1088/1748-0221/13/10/P10005. URL: https://dx.doi.org/10.1088/1748-0221/13/10/P10005.

[61] CMS Collaboration. Identification of hadronic tau lepton decays using a deep neural network. *Journal of Instrumentation* 17.07 (July 2022), P07023. DOI: 10.1088/1748-0221/17/07/P07023. URL: https://dx.doi.org/10.1088/1748-0221/17/07/P07023.

[62] Daniele Bertolini et al. Pileup per particle identification. *Journal of High Energy Physics* 2014.10 (Oct. 2014), p. 59. DOI: 10.1007/JHEP10(2014)059. URL: https://doi.org/10.1007/JHEP10(2014)059.

[63] The CMS Collaboration. Identification of heavy-flavour jets with the CMS detector in pp collisions at 13 TeV. *Journal of Instrumentation* 13.05 (May 2018), P05011. DOI: 10.1088/1748-0221/13/05/P05011. URL: https://dx.doi.org/10.1088/1748-0221/13/05/P05011.

[64] E. Bols et al. Jet flavour classification using DeepJet. *Journal of Instrumentation* 15.12 (Dec. 2020), P12012. DOI: 10.1088/1748-0221/15/12/P12012. URL: https://dx.doi.org/10.1088/1748-0221/15/12/P12012.

[65] CMS Collaboration. Measurement of the charge asymmetry in WH production in the H$\longrightarrow \tau\tau$ decay channel. en. 2025. URL: https://cms-results.web.cern.ch/cms-results/public-results/preliminary-results/HIG-24-019/index.html.

[66] CMS Collaboration. Precision luminosity measurement in proton–proton collisions at $\sqrt{s} = 13\,\text{TeV}$ in 2015 and 2016 at CMS. *The European Physical journaltitle C* 81.9 (Sept. 2021), p. 800. DOI: 10.1140/epjc/s10052-021-09538-2. URL: https://doi.org/10.1140/epjc/s10052-021-09538-2.

[67] CMS Collaboration. CMS luminosity measurement for the 2017 data-taking period at $\sqrt{s} = 13$ TeV. Tech. rep. Geneva: CERN, 2018. URL: https://cds.cern.ch/record/2621960.

[68] CMS luminosity measurement for the 2018 data-taking period at $\sqrt{s} = 13$ TeV. Tech. rep. Geneva: CERN, 2019. URL: http://cds.cern.ch/record/2676164.

[69] The CMS Collaboration. Measurements of Higgs boson production in the decay channel with a pair of τ leptons in proton–proton collisions at $\sqrt{s} = 13$ TeV. *The European Physical journaltitle C* 83.7 (July 2023). DOI: 10.1140/epjc/s10052-023-11452-8. URL: http://dx.doi.org/10.1140/epjc/s10052-023-11452-8.

[70] Michał Czakon and Alexander Mitov. Top++: A program for the calculation of the top-pair cross-section at hadron colliders. *Computer Physics Communications* 185.11 (2014), pp. 2930–2938. DOI: https://doi.org/10.1016/j.cpc.2014.06.021. URL: https://www.sciencedirect.com/science/article/pii/S0010465514002264.

[71] The CMS Collaboration. Measurement of the $Z/\gamma^* \rightarrow \tau\tau$ cross section in pp collisions at $\sqrt{s} = 13$ TeV and validation of τ lepton analysis techniques. *The European Physical journaltitle C* 78.9 (Sept. 2018), p. 708. DOI: 10.1140/epjc/s10052-018-6146-9. URL: https://doi.org/10.1140/epjc/s10052-018-6146-9.

[72] The CMS Collaboration. Search for additional neutral MSSM Higgs bosons in the $\tau\ \tau$ final state in proton-proton collisions at $\sqrt{s} = 13$ TeV. *Journal of High Energy Physics* 2018.9 (Sept. 2018), p. 7. DOI: 10.1007/JHEP09(2018)007. URL: https://doi.org/10.1007/JHEP09(2018)007.

[73] Nikita Shadskiy. Search for resonant di-Higgs production in bb+$\tau\tau$ final states in pp collisions at $\sqrt{s} = 13$ TeV. PhD thesis. Karlsruhe Institute of Technology (KIT), 2025.

[74] Johan Alwall et al. MadGraph 5: going beyond. *Journal of High Energy Physics* 2011.6 (June 2011), p. 128. DOI: 10.1007/JHEP06(2011)128. URL: https://doi.org/10.1007/JHEP06(2011)128.

[75] Simone Alioli et al. A general framework for implementing NLO calculations in shower Monte Carlo programs: the POWHEG BOX. *Journal of High Energy Physics* 2010.6 (June 2010), p. 43. DOI: 10.1007/JHEP06(2010)043. URL: https://doi.org/10.1007/JHEP06(2010)043.

[76] Torbjörn Sjöstrand et al. An introduction to PYTHIA 8.2. *Computer Physics Communications* 191 (2015), pp. 159–177. DOI: https://doi.org/10.1016/j.cpc.2015.01.024. URL: https://www.sciencedirect.com/science/article/pii/S0010465515000442.

[77] Richard D. Ball et al. Parton distributions from high-precision collider data. *The European Physical journaltitle C* 77.10 (Oct. 2017), p. 663. DOI: 10.1140/epjc/s10052-017-5199-5. URL: https://doi.org/10.1140/epjc/s10052-017-5199-5.

[78] The CMS Collaboration. Extraction and validation of a new set of CMS PYTHIA8 tunes from underlying-event measurements. *Eur. Phys. J. C* 80 (2020), p. 4. DOI: 10.1140/epjc/s10052-019-7499-4. arXiv: 1903.12179 [hep-ex].

[79] GEANT4 Collaboration. Geant4—a simulation toolkit. *Nuclear Instruments and Methods in Physics Research Section A: Accelerators, Spectrometers, Detectors and Associated Equipment* 506.3 (2003), pp. 250–303. DOI: https://doi.org/10.1016/S0168-9002(03)01368-8. URL: https://www.sciencedirect.com/science/article/pii/S0168900203013688.

[80] The CMS Collaboration. A portrait of the Higgs boson by the CMS experiment ten years after the discovery. *Nature* 607.7917 (July 2022), pp. 60–68. DOI: 10.1038/s41586-022-04892-x. URL: https://doi.org/10.1038/s41586-022-04892-x.

[81] CERN cross section database. URL: https://xsecdb-xsdb-official.app.cern.ch/xsdb/ (visited on 04/06/2025).

[82] The CMS Collaboration. Measurements of inclusive W and Z cross sections in pp collisions at $\sqrt{s} = 7$ TeV. *Journal of High Energy Physics* 2011.1 (Jan. 2011), p. 80. DOI: 10.1007/JHEP01(2011)080. URL: https://doi.org/10.1007/JHEP01(2011)080.

[83] The CMS Collaboration. Jet energy scale and resolution in the CMS experiment in pp collisions at 8 TeV. *JINST* 12 (2017), P02014. DOI: 10.1088/1748-0221/12/02/P02014. arXiv: 1607.03663 [hep-ex].

[84] The CMS collaboration. Identification of heavy-flavour jets with the CMS detector in pp collisions at 13 TeV. *Journal of Instrumentation* 13.05 (May 2018), P05011. DOI: 10.1088/1748-0221/13/05/P05011. URL: https://dx.doi.org/10.1088/1748-0221/13/05/P05011.

[85] Diederik P. Kingma and Jimmy Ba. Adam: A Method for Stochastic Optimization. 2017. arXiv: 1412.6980 [cs.LG]. URL: https://arxiv.org/abs/1412.6980.

[86] Nitish Srivastava et al. Dropout: A Simple Way to Prevent Neural Networks from Overfitting. *Journal of Machine Learning Research* 15.56 (2014), pp. 1929–1958. URL: http://jmlr.org/papers/v15/srivastava14a.html.

[87] A. N. Tikhonov. Solution of incorrectly formulated problems and the regularization. *Soviet Math. Dokl. 4* (1963).

[88] Stefan Wunsch et al. Identifying the Relevant Dependencies of the Neural Network Response on Characteristics of the Input Space. *Computing and Software for Big Science* 2.1 (Sept. 2018), p. 5. DOI: 10.1007/s41781-018-0012-1. URL: https://doi.org/10.1007/s41781-018-0012-1.

[89] Robert D. Cousins. Generalization of Chisquare Goodness-of-Fit Test for Binned Data Using Saturated Models, with Application to Histograms. Accessed: 2025-08-24. 2013. URL: https://www.physics.ucla.edu/~cousins/stats/cousins_saturated.pdf.

[90] A. N. Kolmogorov. Sulla determinazione empirica di una legge di distribuzione. Italian. *Giornale dell'Istituto Italiano degli Attuari* 4 (1933), pp. 83–91.

[91] N. Smirnov. Table for Estimating the Goodness of Fit of Empirical Distributions. *The Annals of Mathematical Statistics* 19.2 (June 1948), pp. 279–281.

[92] T. W. Anderson and D. A. Darling. Asymptotic Theory of Certain "Goodness of Fit" Criteria Based on Stochastic Processes. *The Annals of Mathematical Statistics* 23.2 (June 1952), pp. 193–212. DOI: 10.1214/aoms/1177729437.

[93] The CMS Collaboration. Measurement of the inelastic proton-proton cross section at $\sqrt{s} = 13$ TeV. *Journal of High Energy Physics* 2018.7 (July 2018), p. 161. DOI: 10.1007/JHEP07(2018)161. URL: https://doi.org/10.1007/JHEP07(2018)161.

[94] Roger Barlow and Christine Beeston. Fitting using finite Monte Carlo samples. *Computer Physics Communications* 77.2 (1993), pp. 219–228. DOI: https://doi.org/10.1016/0010-4655(93)90005-W. URL: https://www.sciencedirect.com/science/article/pii/001046559390005W.

[95] Gary J. Feldman and Robert D. Cousins. Unified approach to the classical statistical analysis of small signals. *Phys. Rev. D* 57 (7 Apr. 1998), pp. 3873–3889. DOI: 10.1103/PhysRevD.57.3873. URL: https://link.aps.org/doi/10.1103/PhysRevD.57.3873.

[96] STXS Twiki. URL: https://twiki.cern.ch/twiki/bin/view/LHCPhysics/LHCHWGFiducialAndSTXS (visited on 10/07/2025).

A. Appendix

A.1. Inclusive Control Distributions

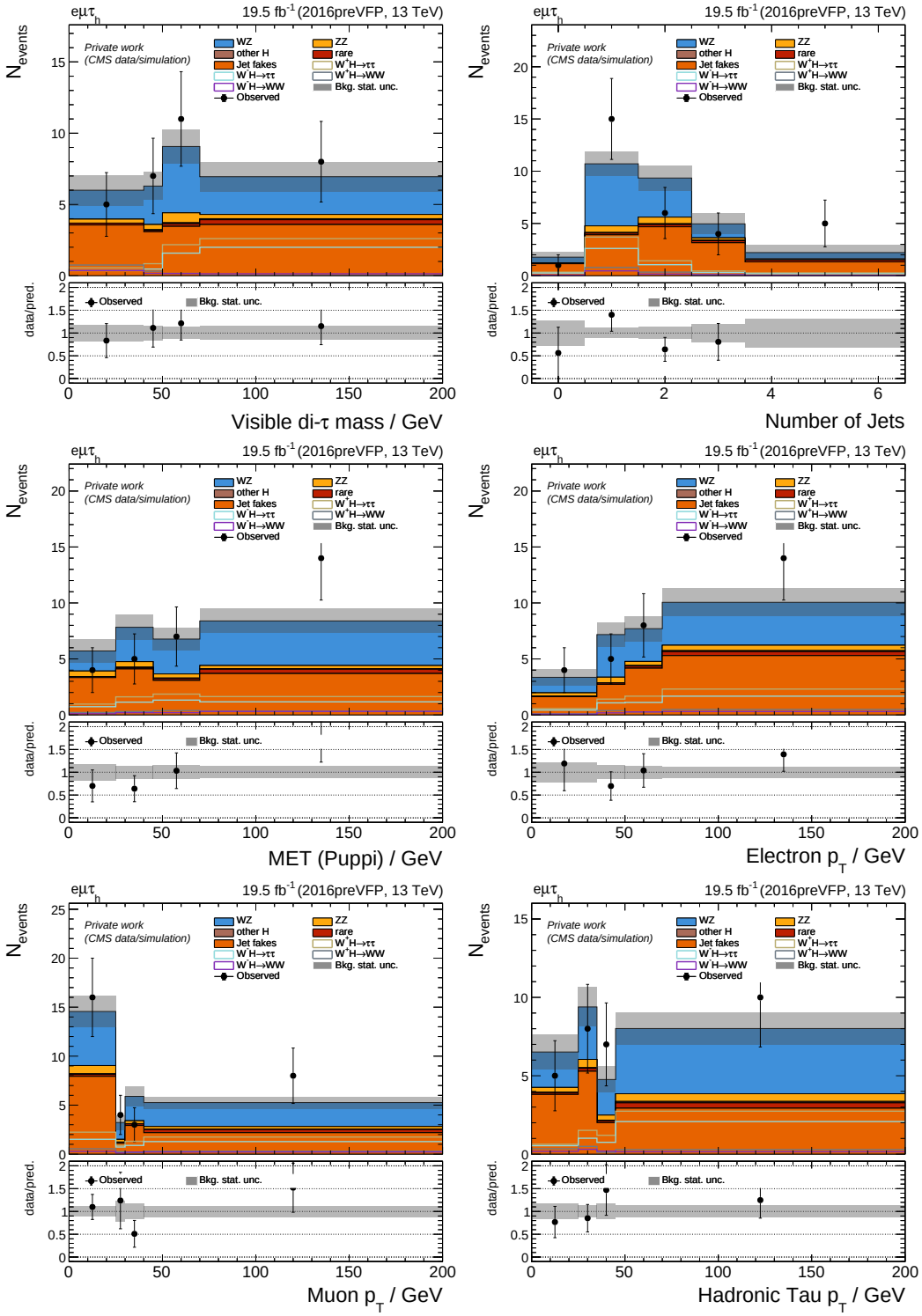

Figure A.1.: Inclusive control distributions of a selection of input variables for the NN training. Shown are statistical uncertainties only.

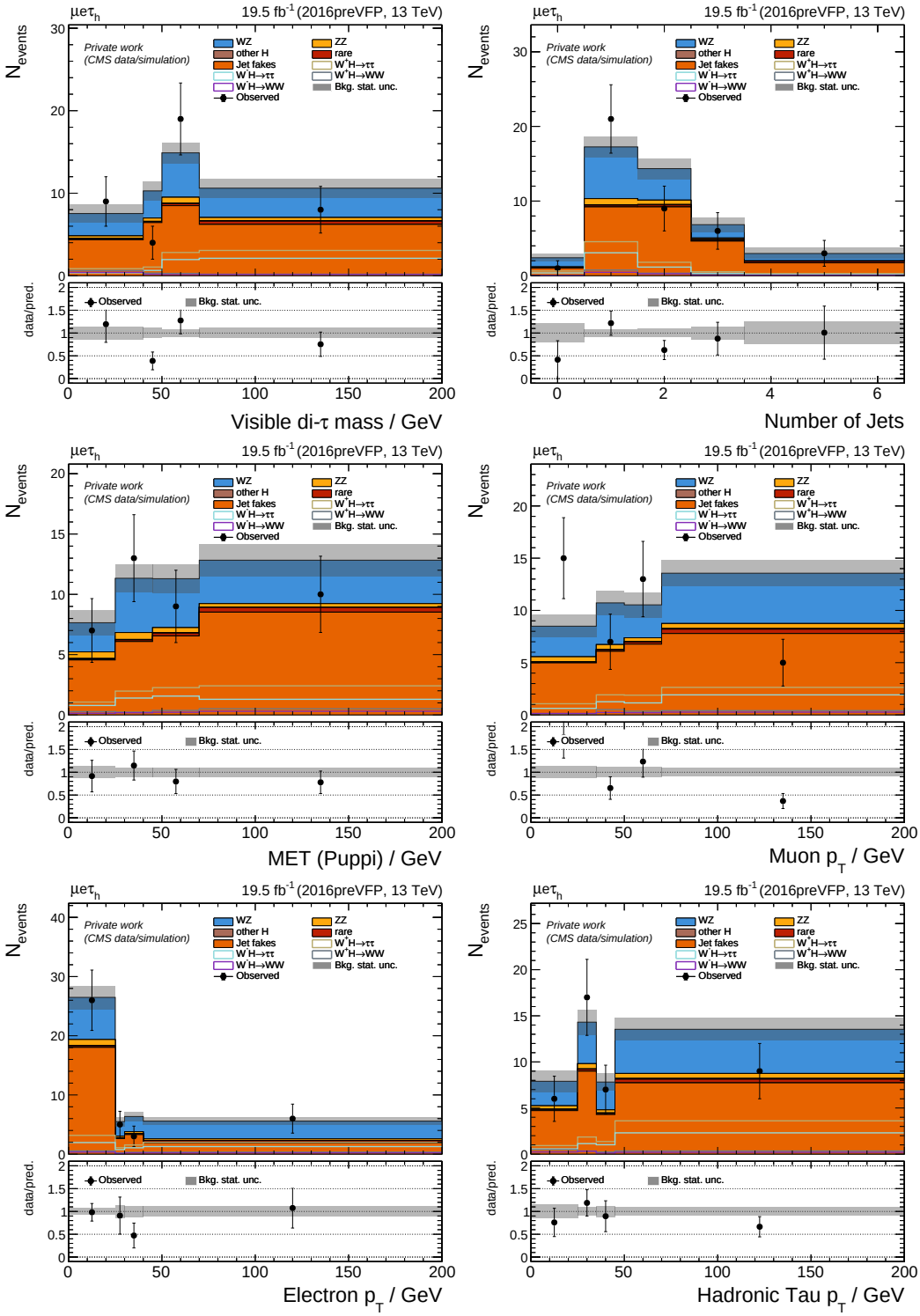

Figure A.2.: Inclusive control distributions of a selection of input variables for the NN training. Shown are statistical uncertainties only.

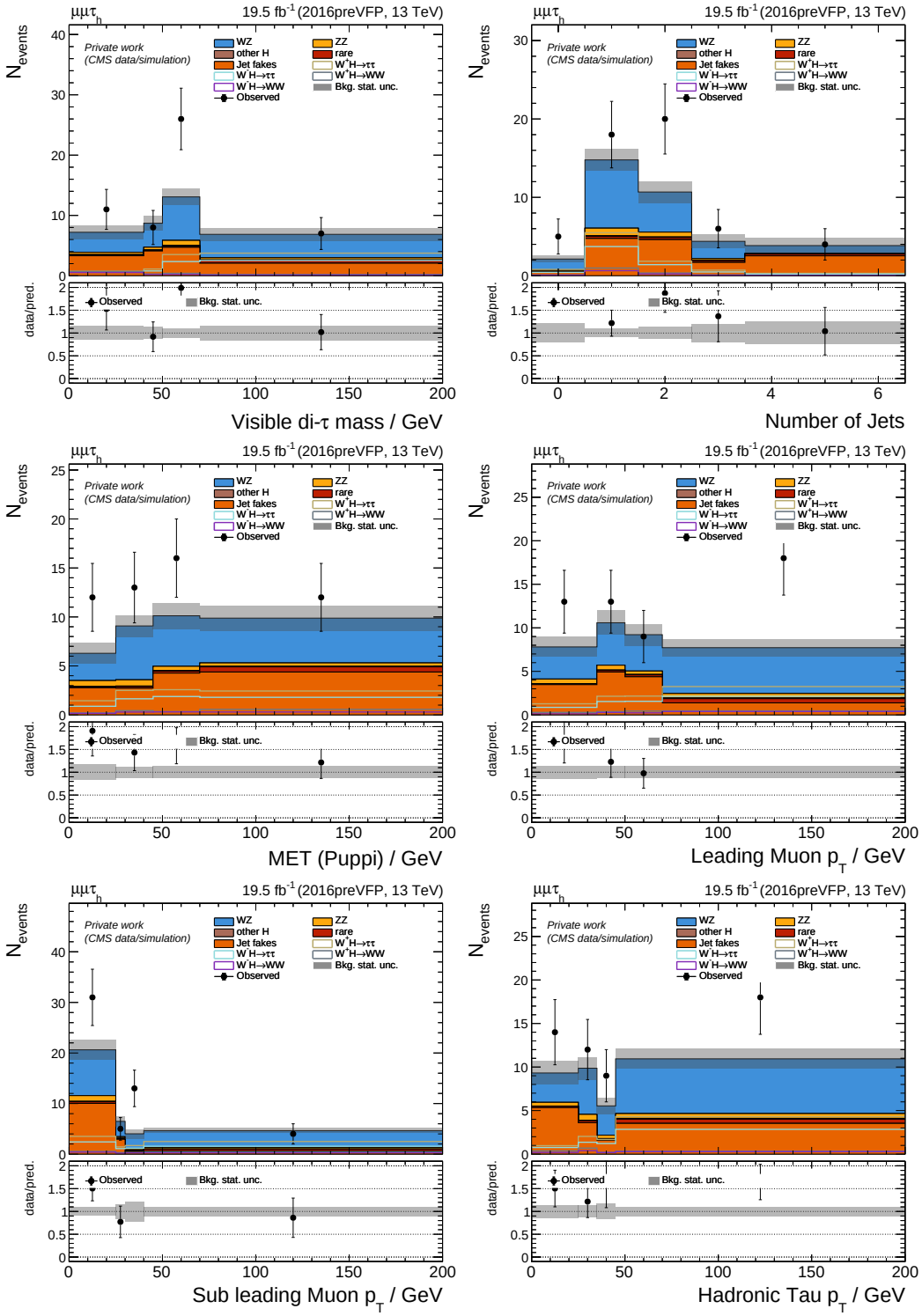

Figure A.3.: Inclusive control distributions of a selection of input variables for the NN training. Shown are statistical uncertainties only.

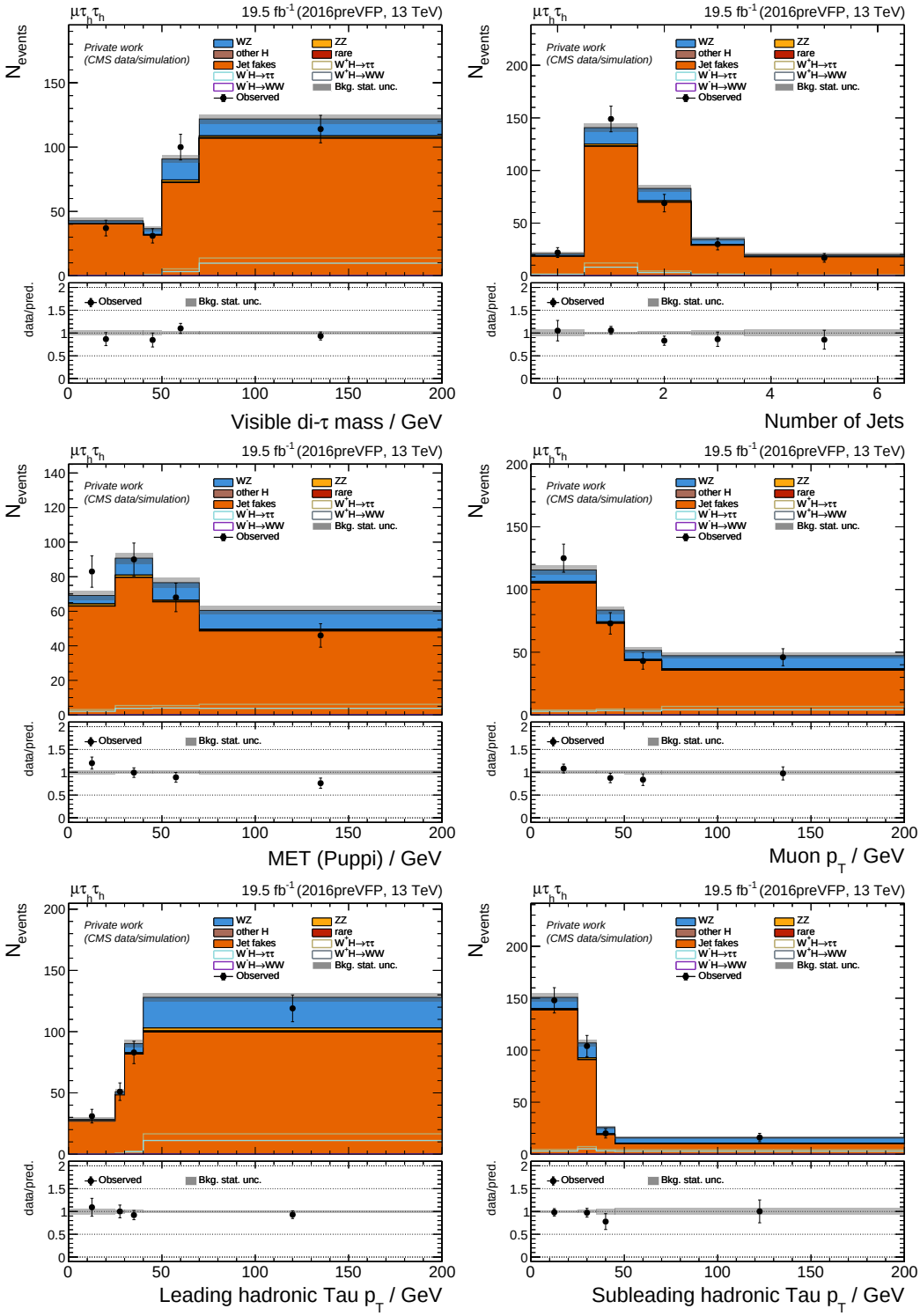

Figure A.4.: Inclusive control distributions of a selection of input variables for the NN training. Shown are statistical uncertainties only.

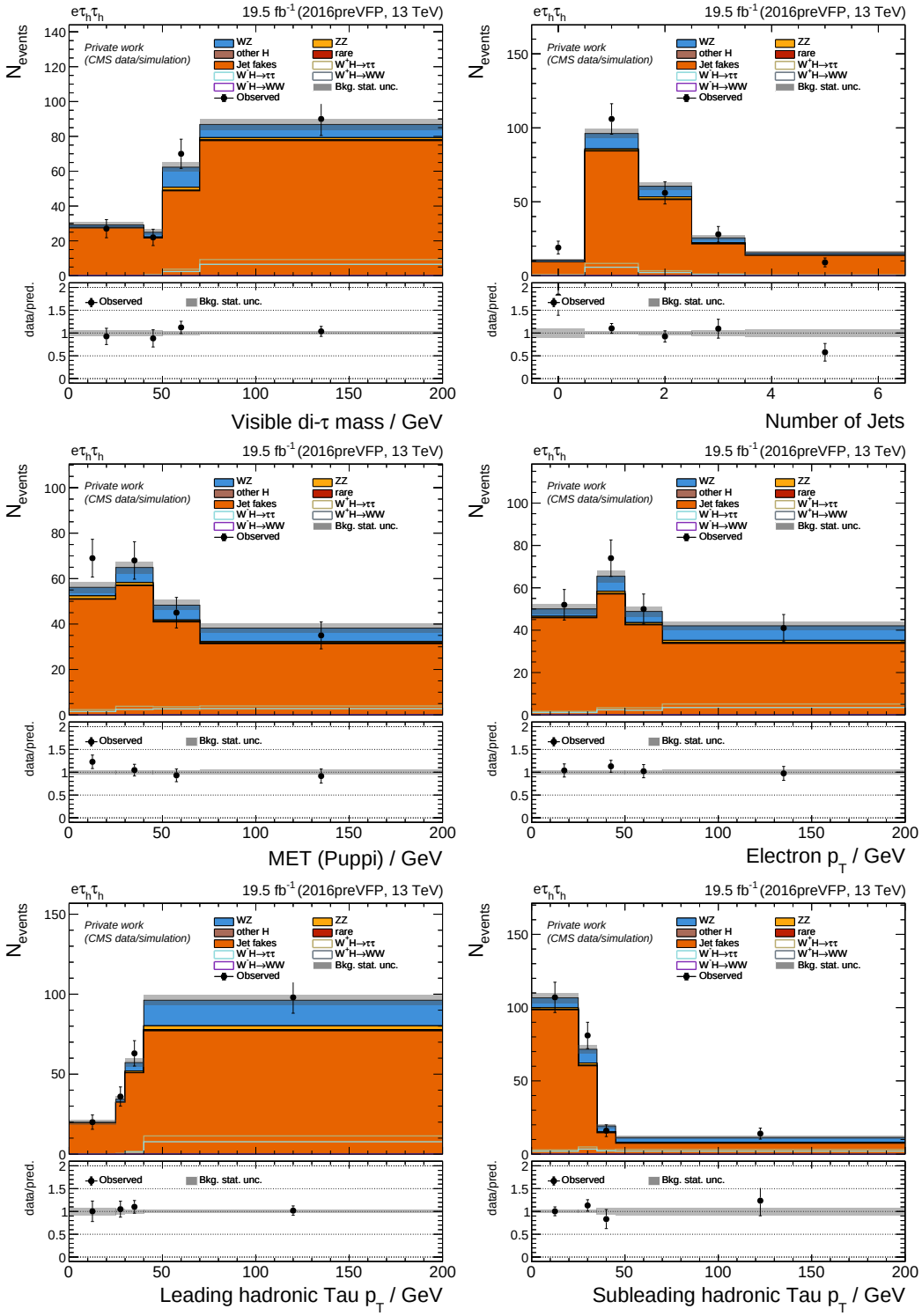

Figure A.5.: Inclusive control distributions of a selection of input variables for the NN training. Shown are statistical uncertainties only.

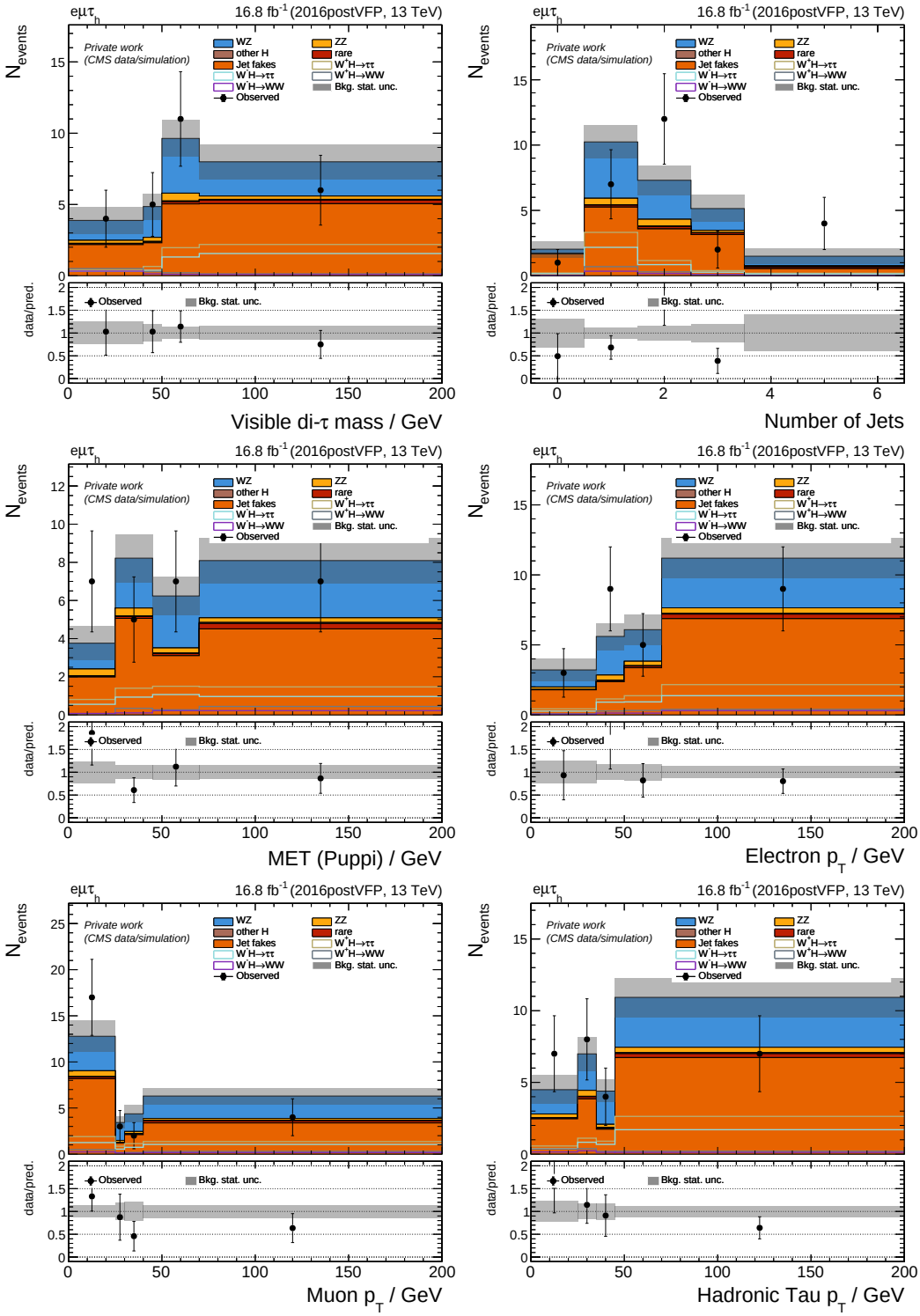

Figure A.6.: Inclusive control distributions of a selection of input variables for the NN training. Shown are statistical uncertainties only.

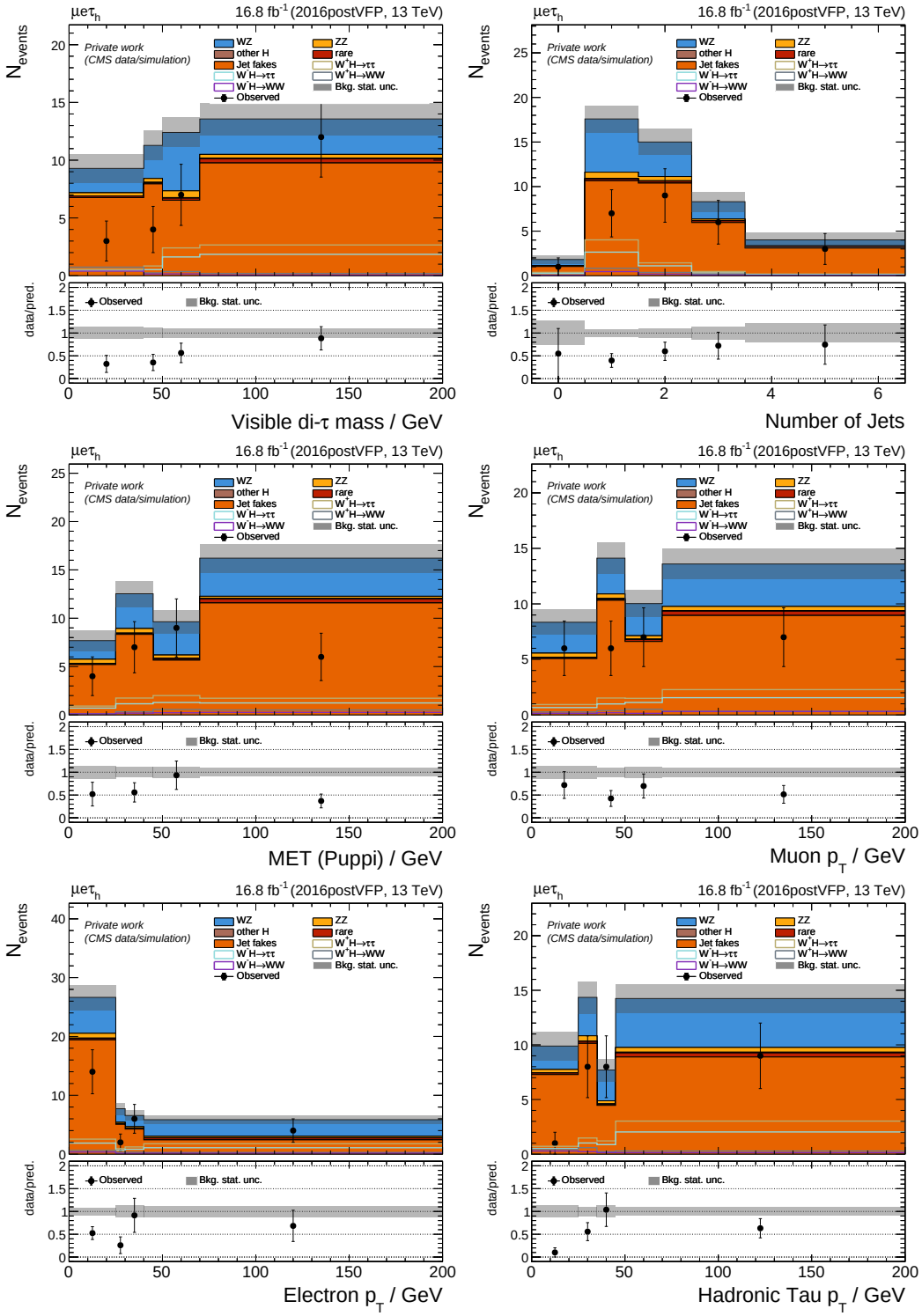

Figure A.7.: Inclusive control distributions of a selection of input variables for the NN training. Shown are statistical uncertainties only.

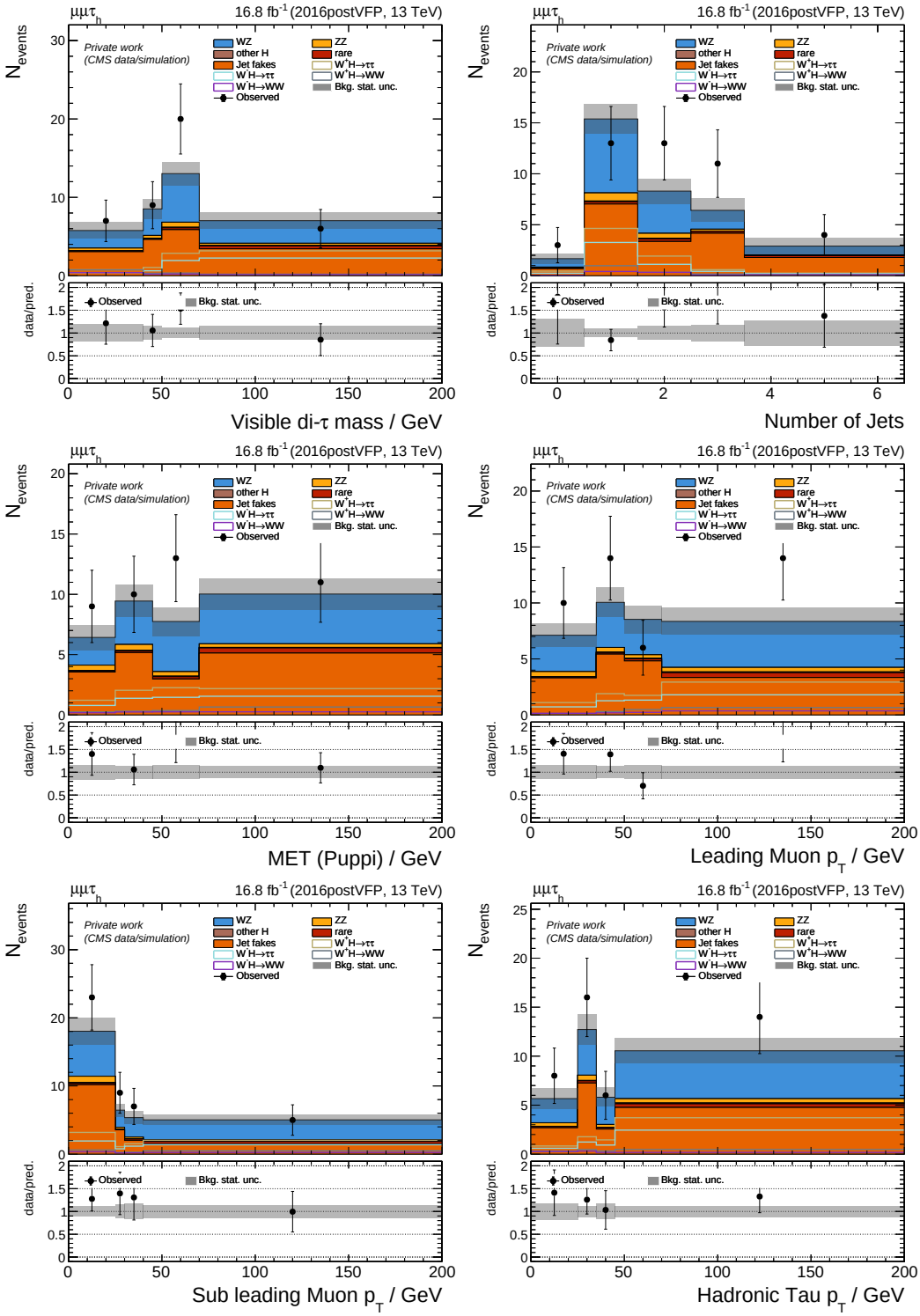

Figure A.8.: Inclusive control distributions of a selection of input variables for the NN training. Shown are statistical uncertainties only.

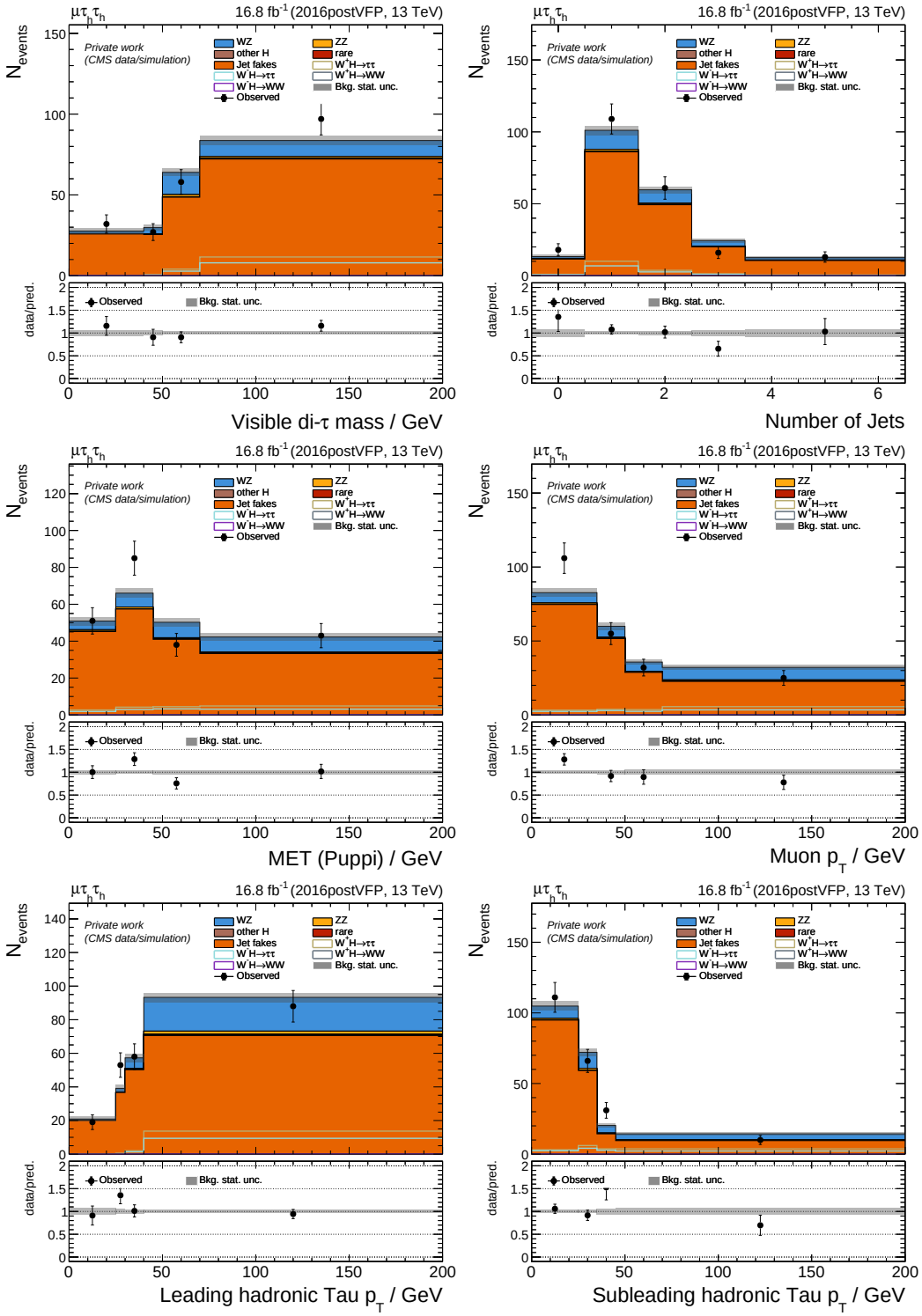

Figure A.9.: Inclusive control distributions of a selection of input variables for the NN training. Shown are statistical uncertainties only.

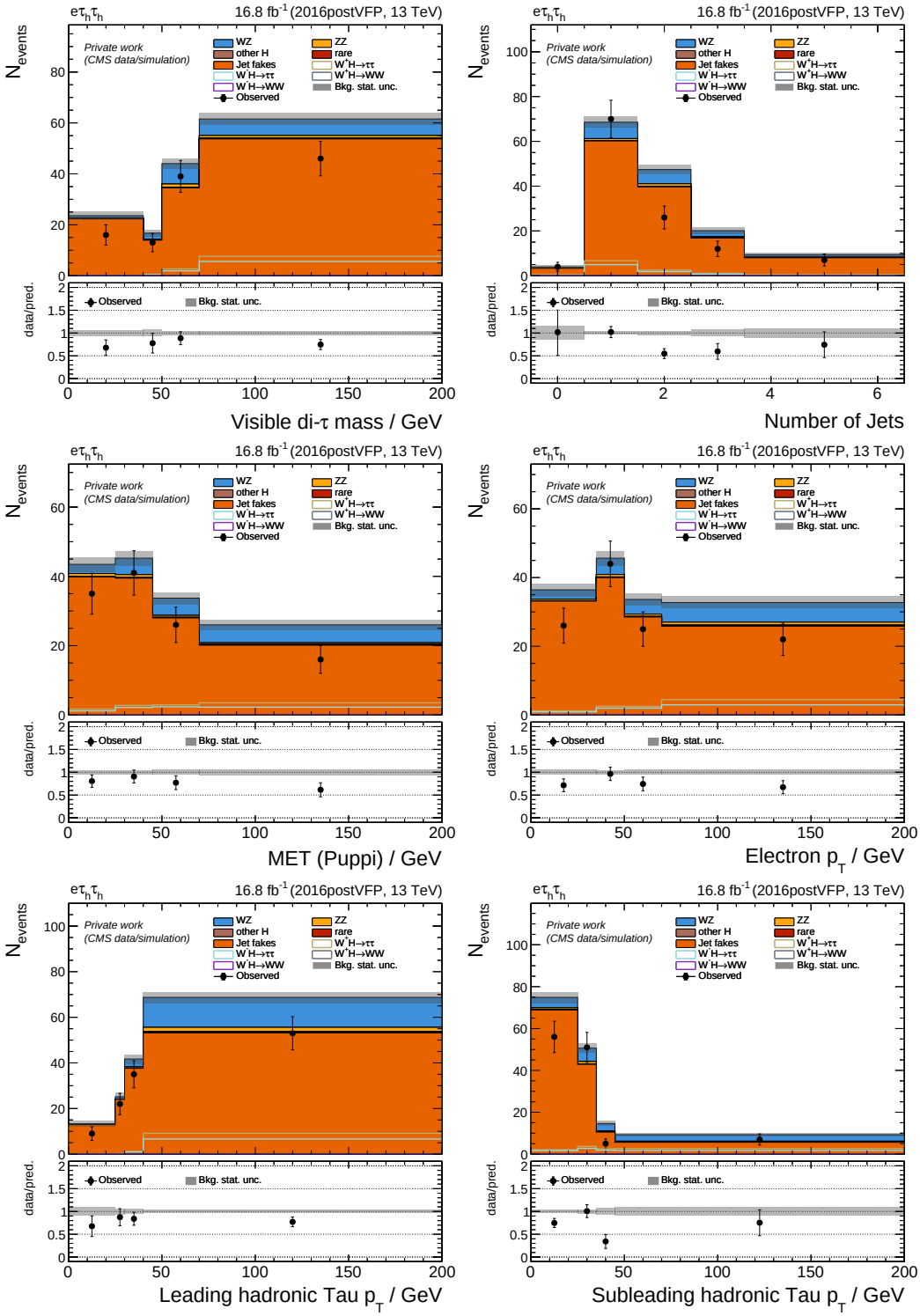

Figure A.10.: Inclusive control distributions of a selection of input variables for the NN training. Shown are statistical uncertainties only.

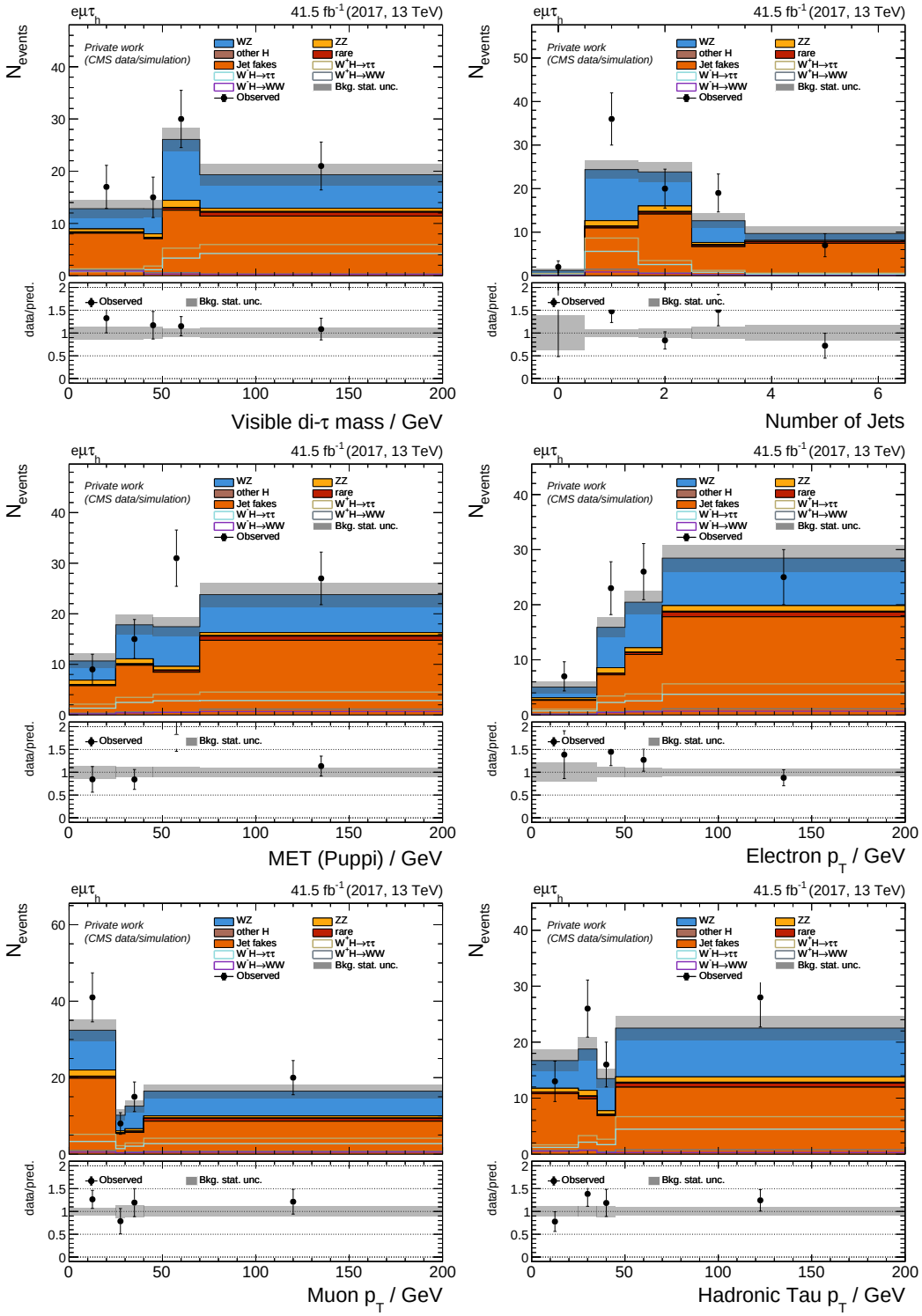

Figure A.11.: Inclusive control distributions of a selection of input variables for the NN training. Shown are statistical uncertainties only.

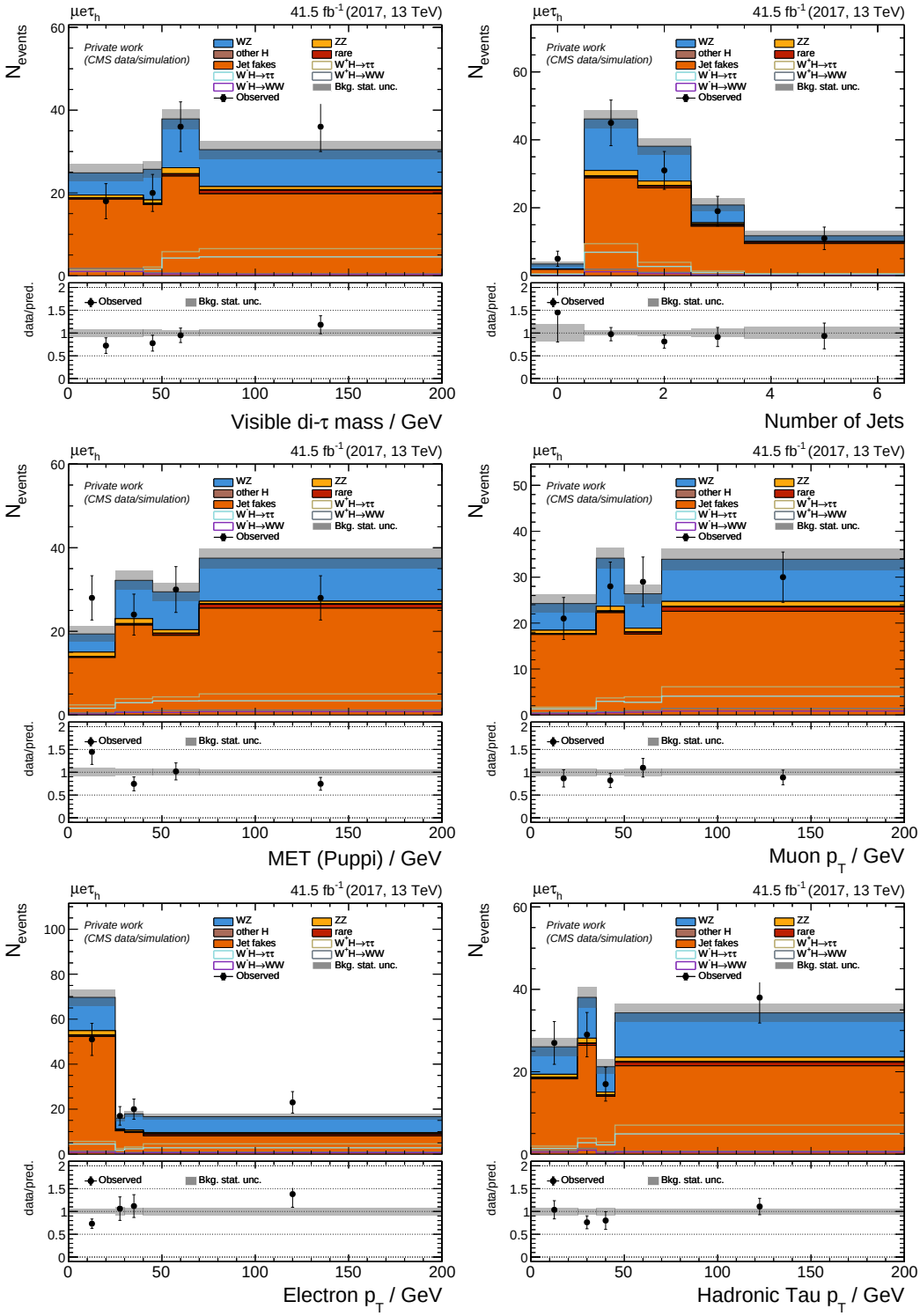

Figure A.12.: Inclusive control distributions of a selection of input variables for the NN training. Shown are statistical uncertainties only.

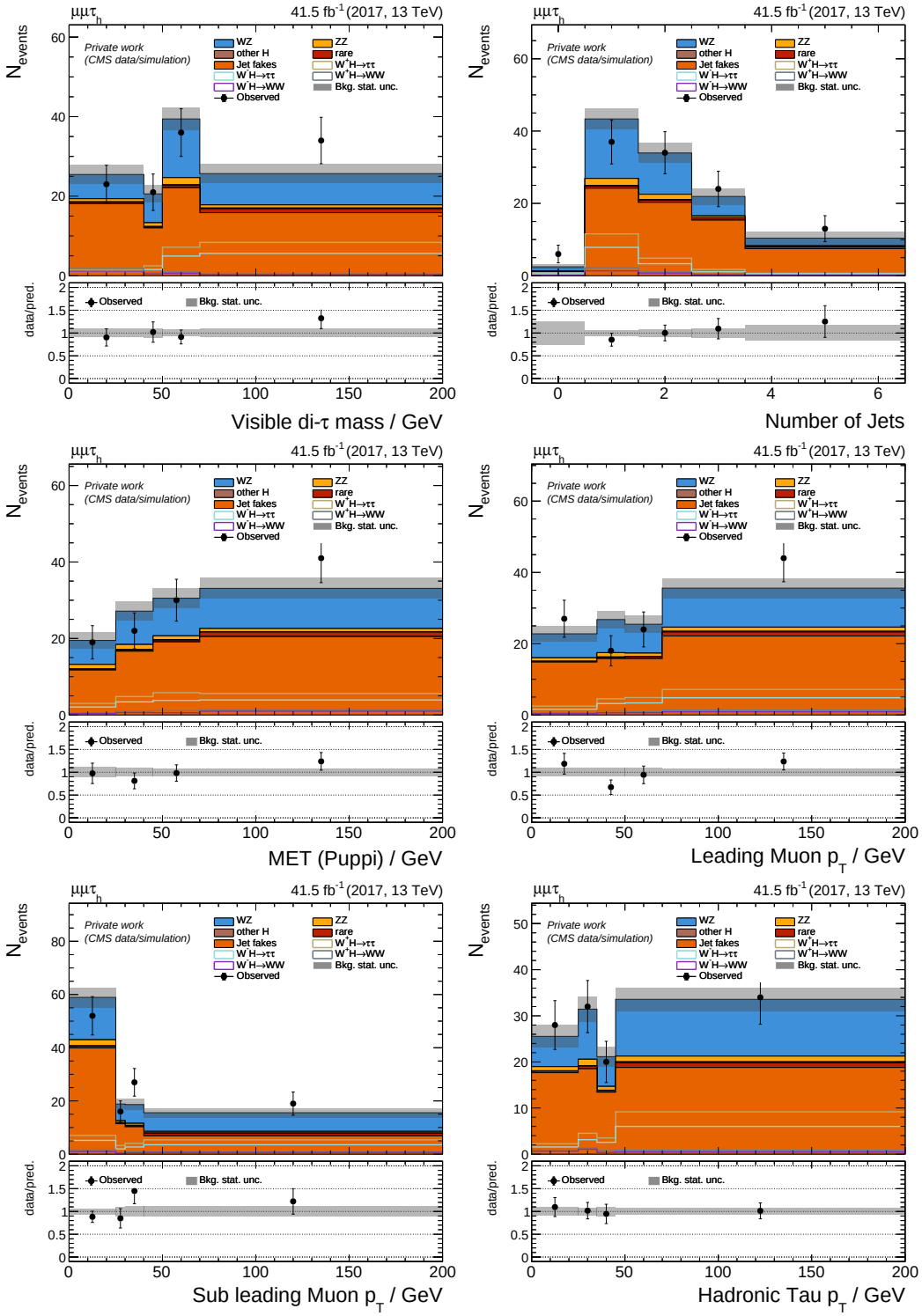

Figure A.13.: Inclusive control distributions of a selection of input variables for the NN training. Shown are statistical uncertainties only.

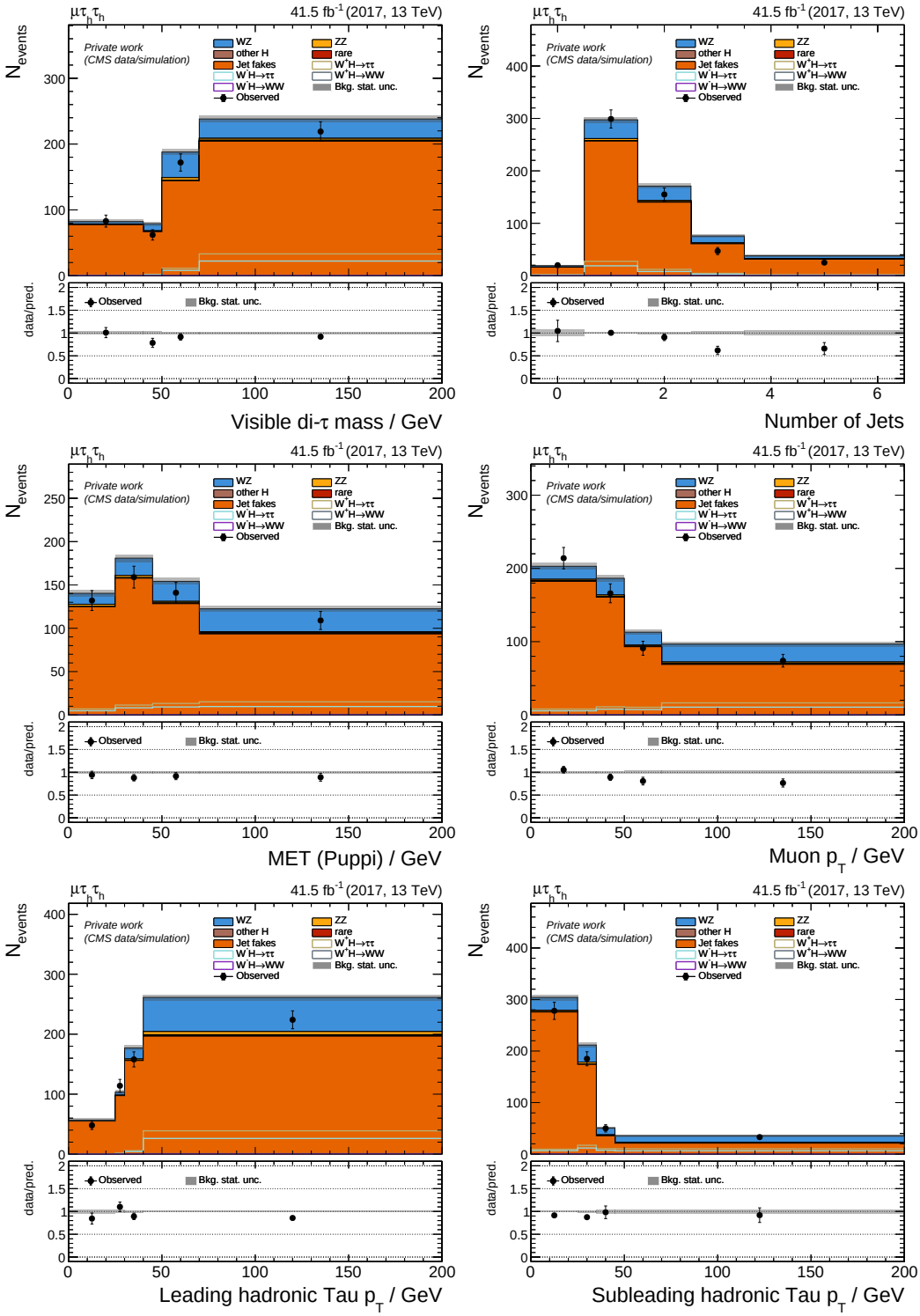

Figure A.14.: Inclusive control distributions of a selection of input variables for the NN training. Shown are statistical uncertainties only.

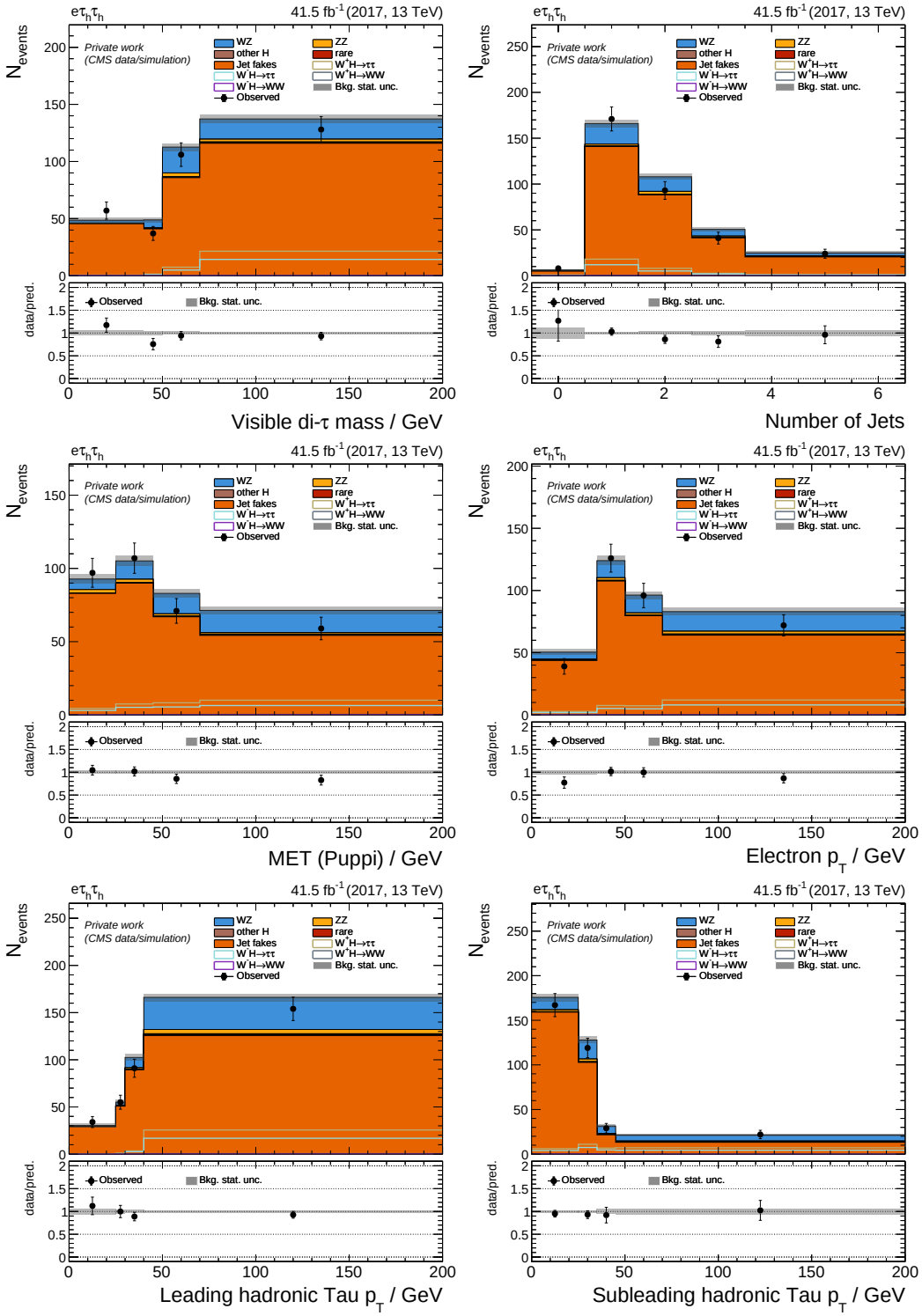

Figure A.15.: Inclusive control distributions of a selection of input variables for the NN training. Shown are statistical uncertainties only.

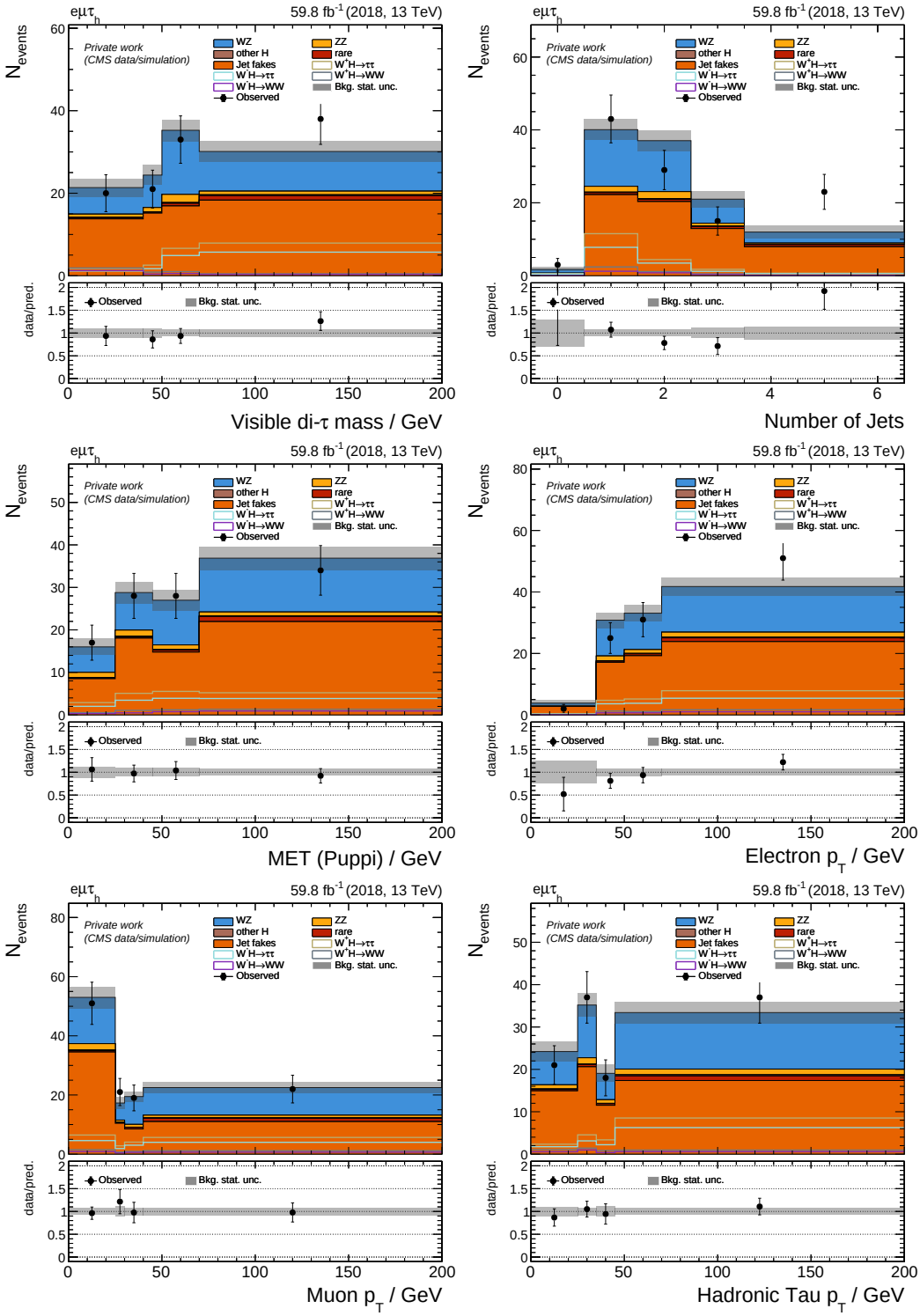

Figure A.16.: Inclusive control distributions of a selection of input variables for the NN training. Shown are statistical uncertainties only.

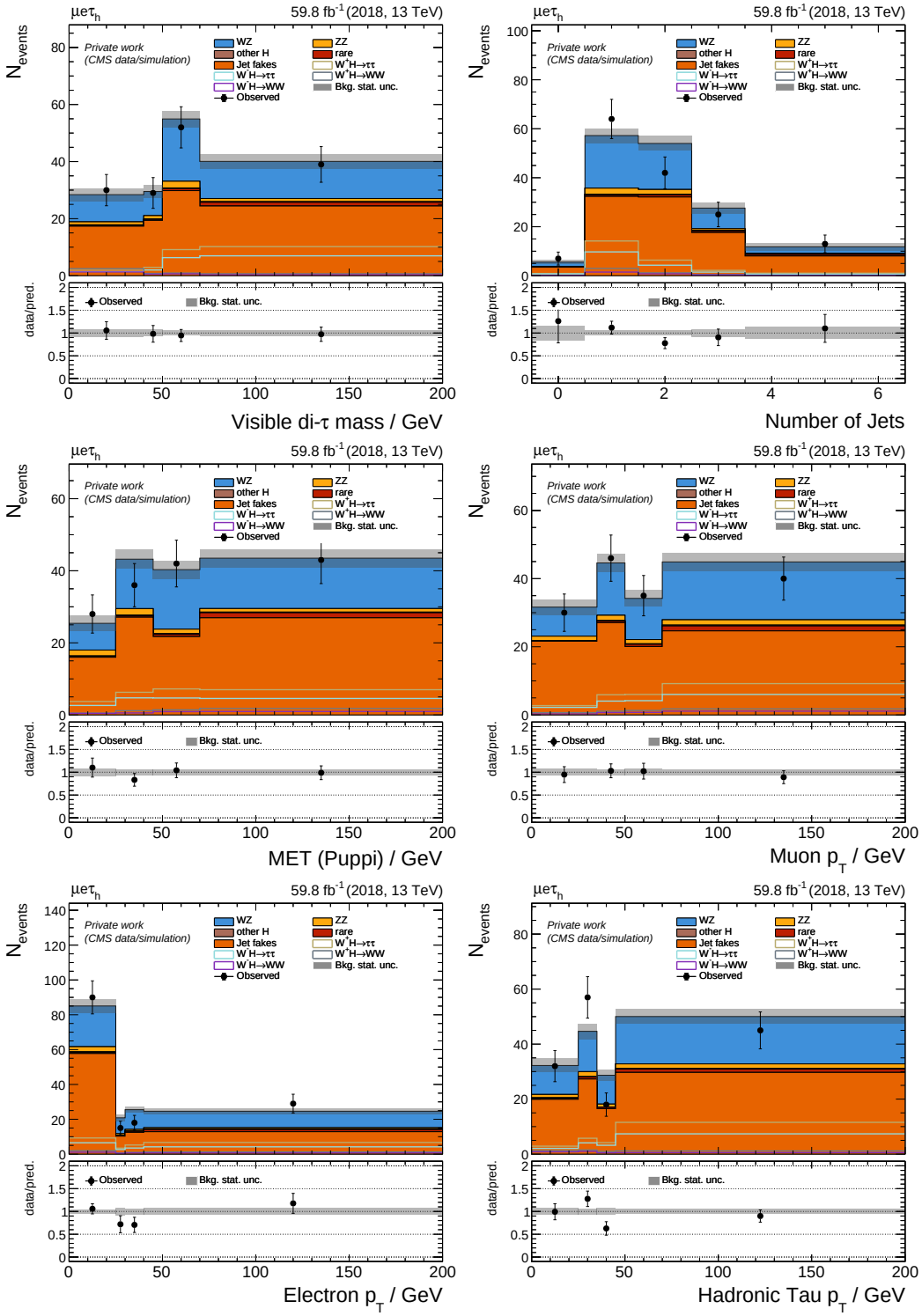

Figure A.17.: Inclusive control distributions of a selection of input variables for the NN training. Shown are statistical uncertainties only.

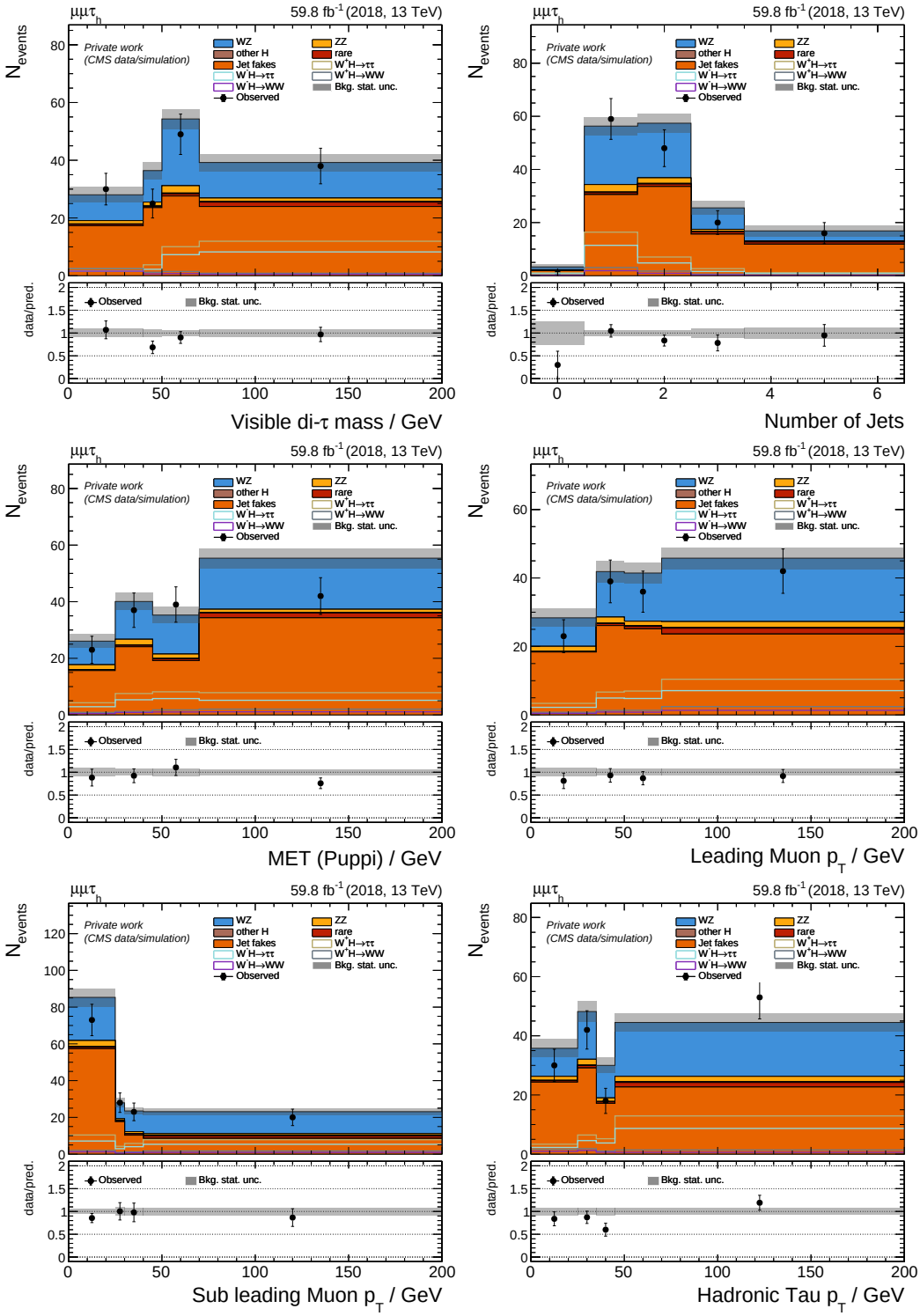

Figure A.18.: Inclusive control distributions of a selection of input variables for the NN training. Shown are statistical uncertainties only.

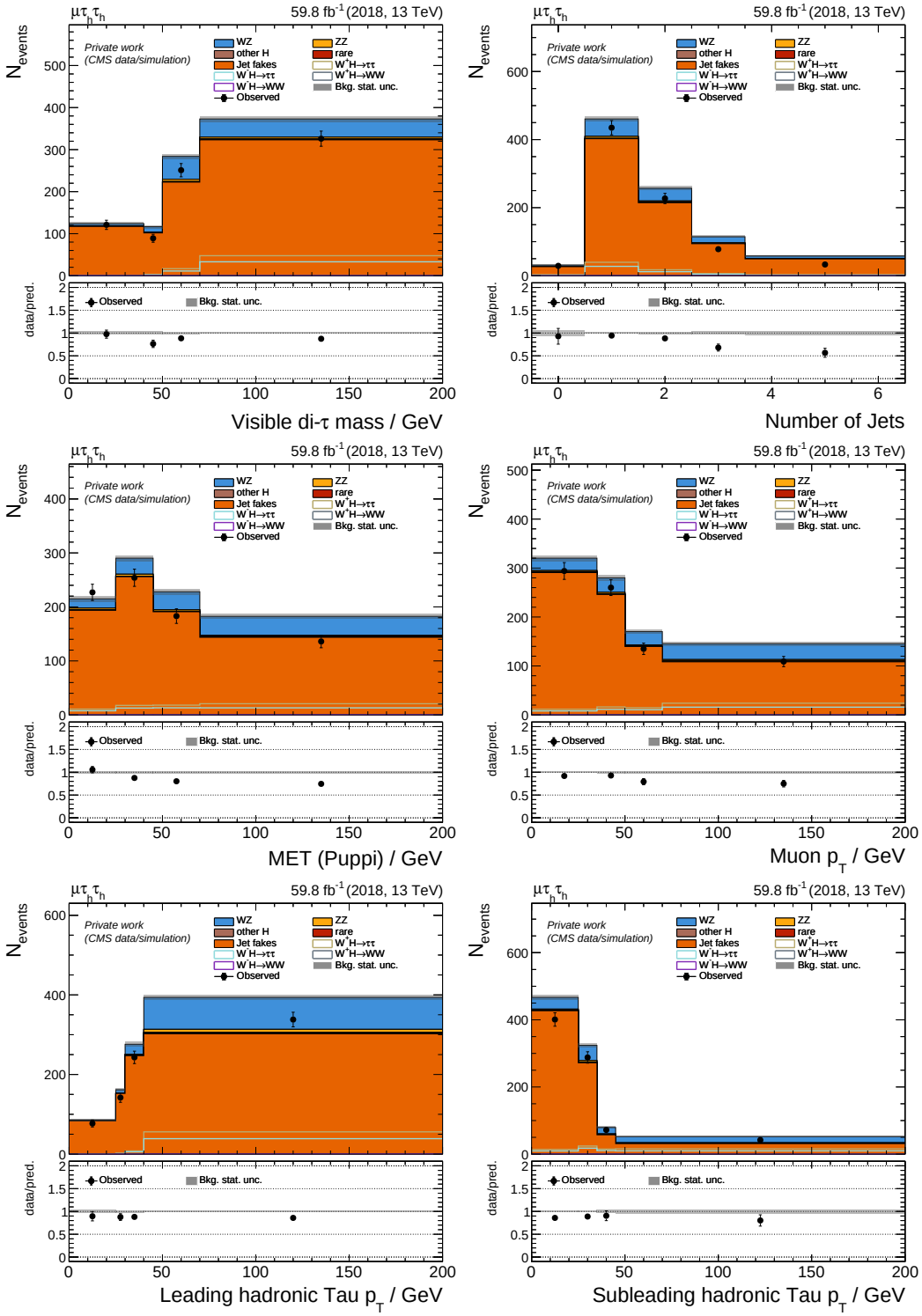

Figure A.19.: Inclusive control distributions of a selection of input variables for the NN training. Shown are statistical uncertainties only.

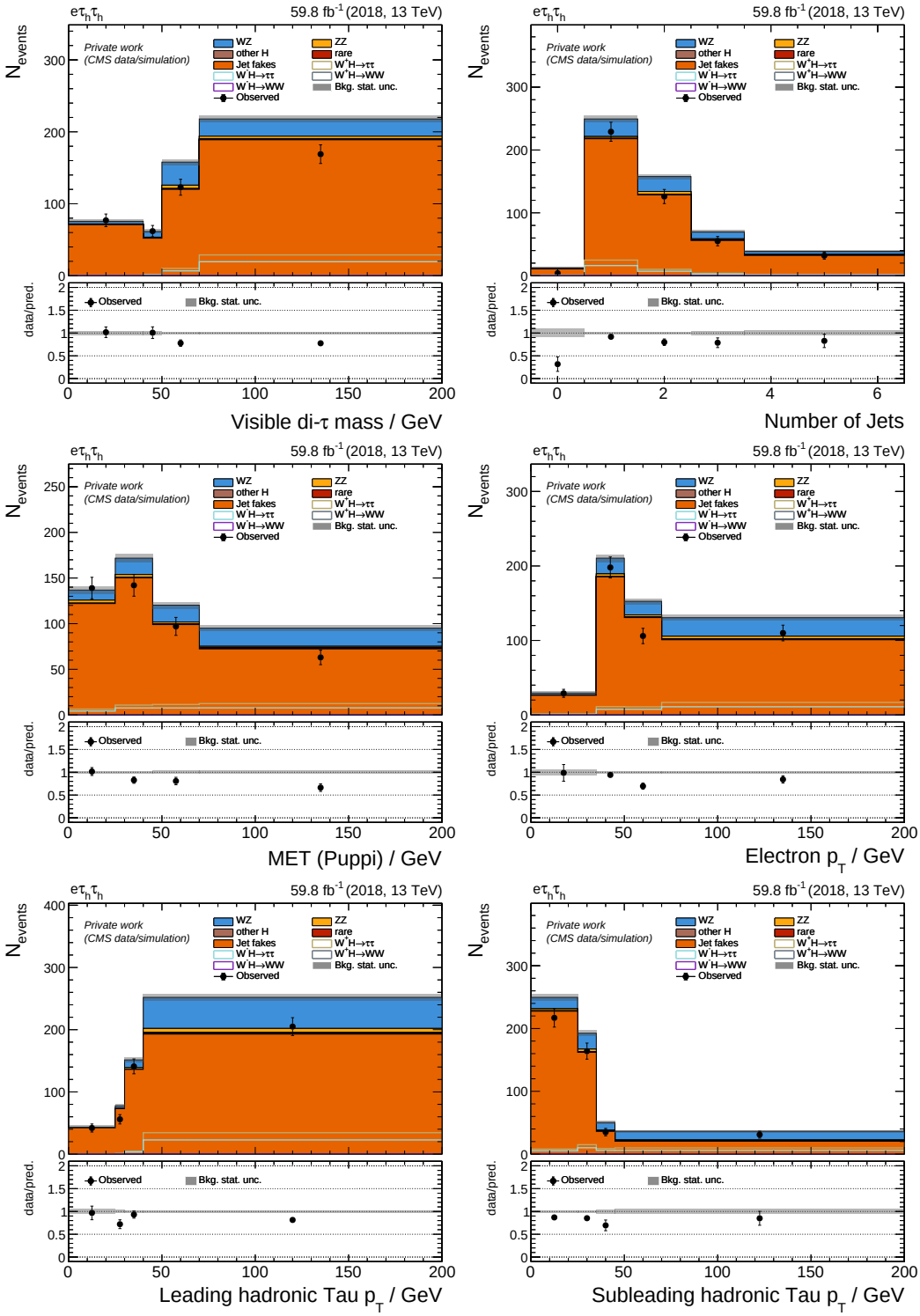

Figure A.20.: Inclusive control distributions of a selection of input variables for the NN training. Shown are statistical uncertainties only.

A.2. Goodness-of-Fit tests of the Neural Net Input Variables

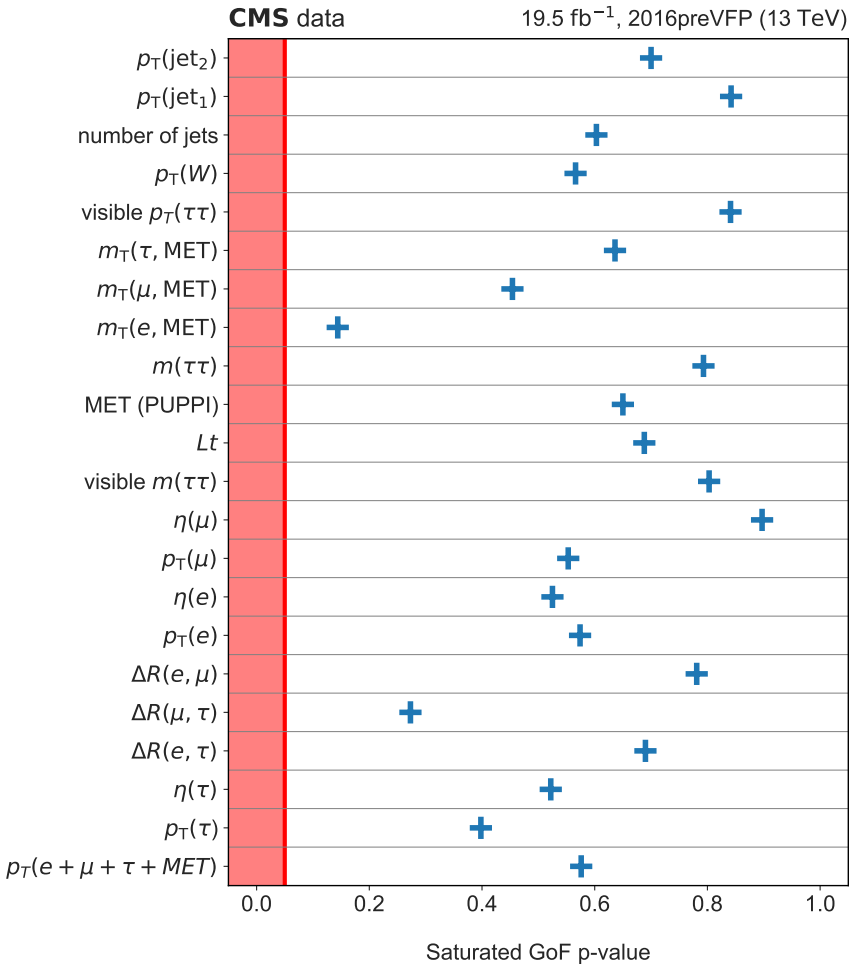

Figure A.21.: Results for the 1D GoF tests for the input variables used for the NN classification in the e$\mu\tau_h$ final state using 2016preVFP data.

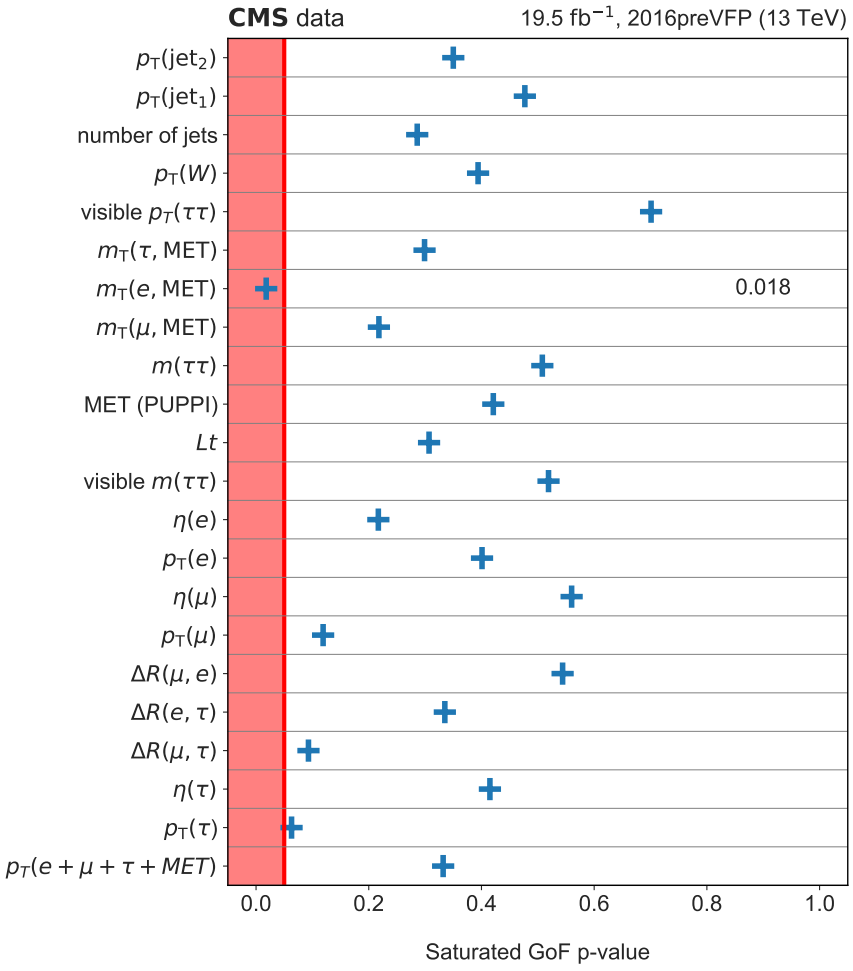

Figure A.22.: Results for the 1D GoF tests for the input variables used for the NN classification in the $\mu e \tau_h$ final state using 2016preVFP data.

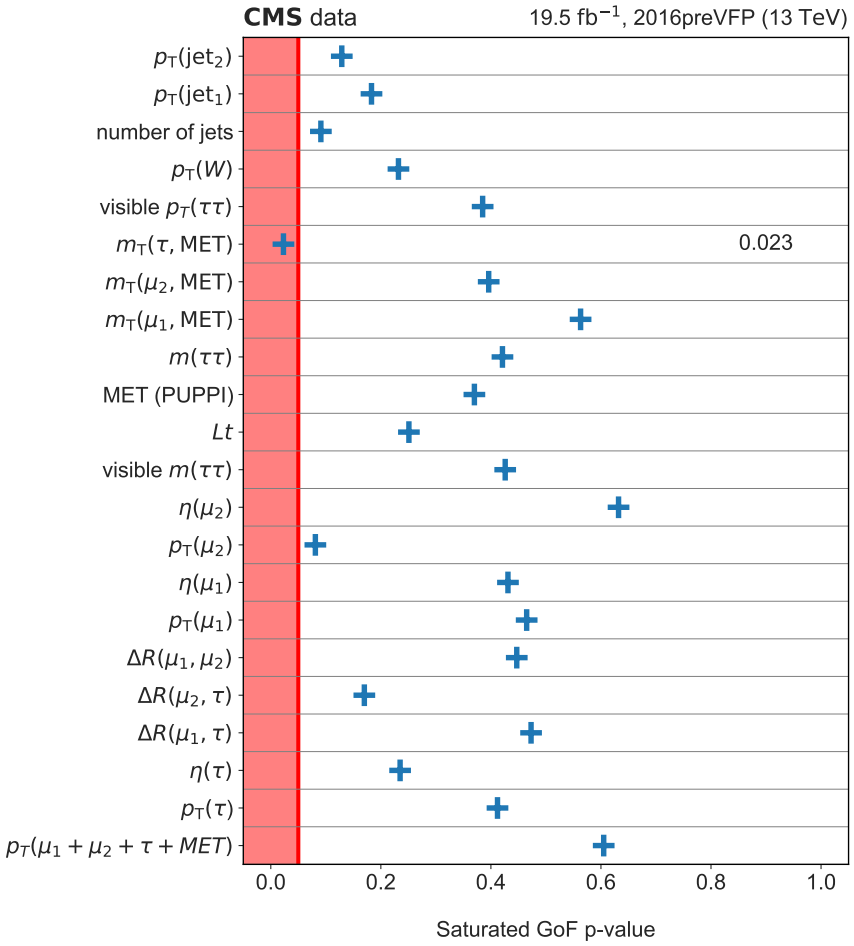

Figure A.23.: Results for the 1D GoF tests for the input variables used for the NN classification in the $\mu\mu\tau_h$ final state using 2016preVFP data.

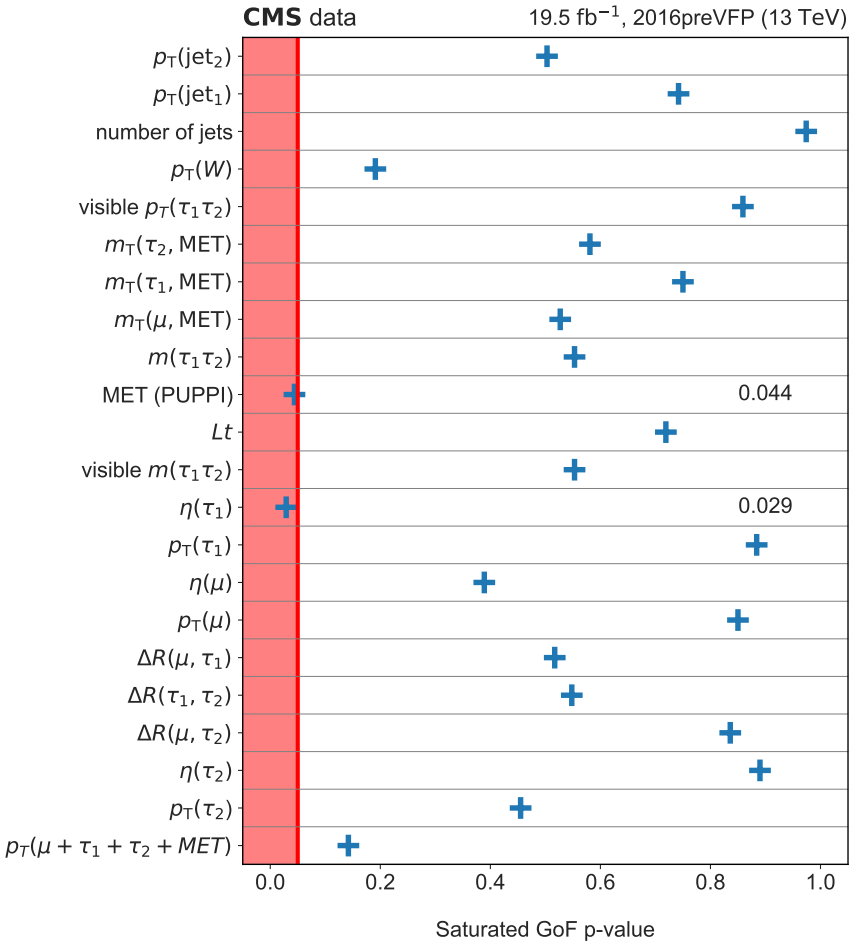

Figure A.24.: Results for the 1D GoF tests for the input variables used for the NN classification in the $\mu\tau_h\tau_h$ final state using 2016preVFP data.

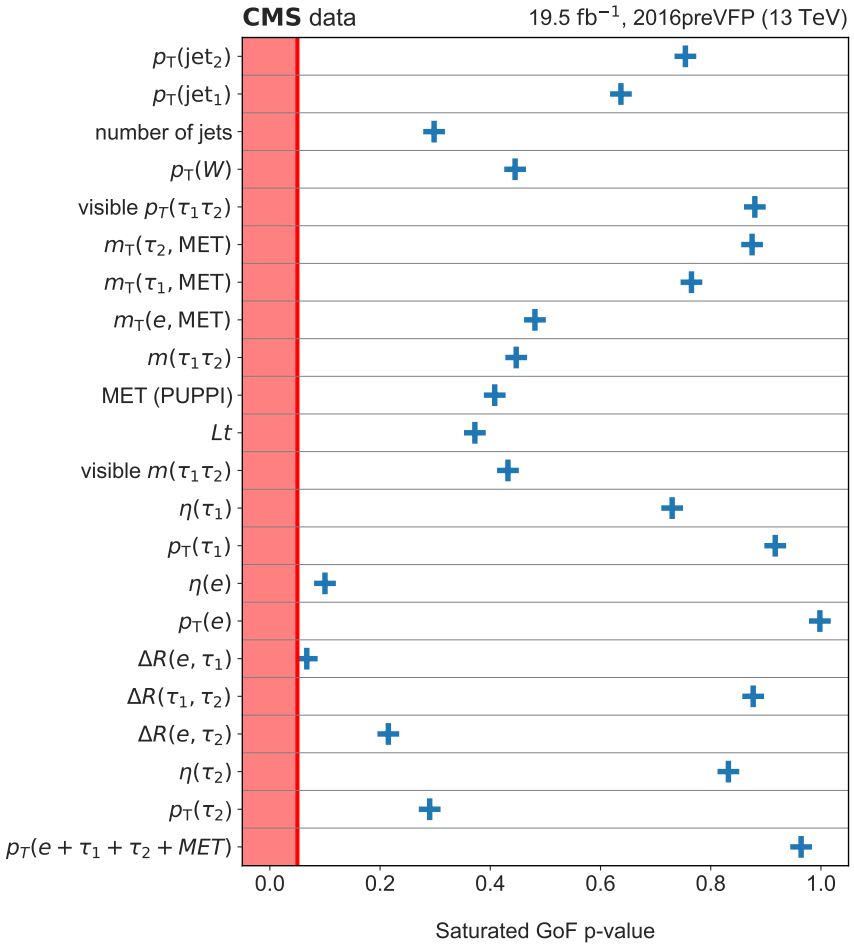

Figure A.25.: Results for the 1D GoF tests for the input variables used for the NN classification in the $e\tau_h\tau_h$ final state using 2016preVFP data.

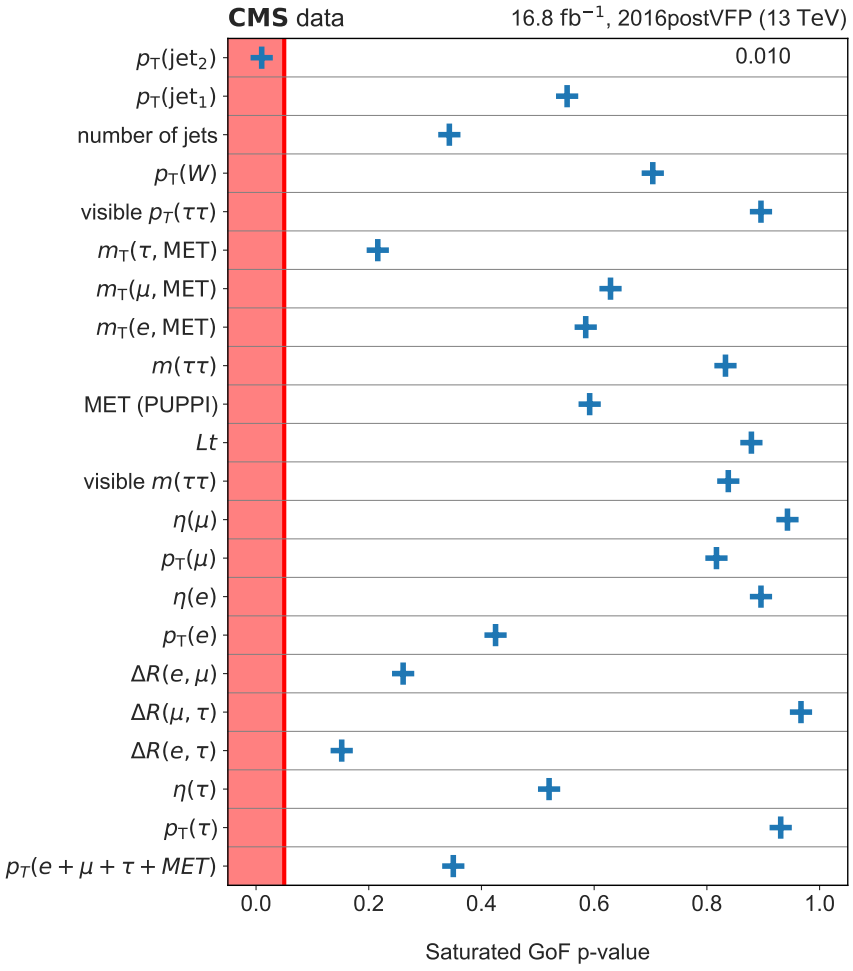

Figure A.26.: Results for the 1D GoF tests for the input variables used for the NN classification in the e$\mu\tau_h$ final state using 2016postVFP data.

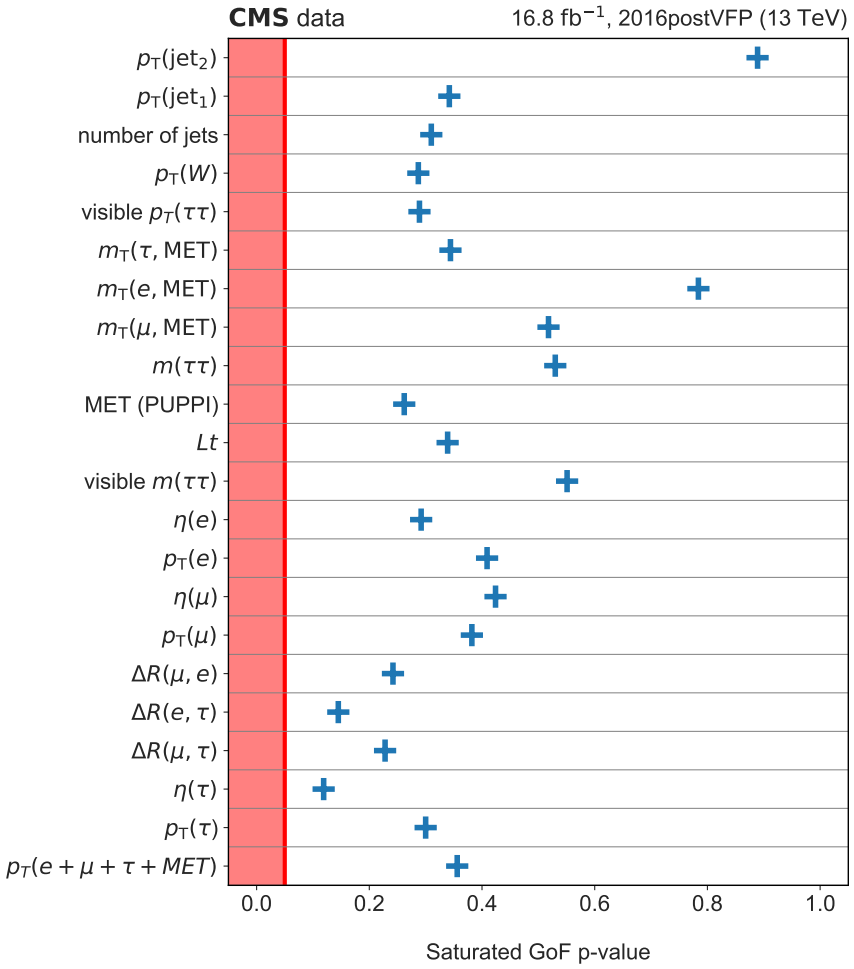

Figure A.27.: Results for the 1D GoF tests for the input variables used for the NN classification in the $\mu e \tau_h$ final state using 2016postVFP data.

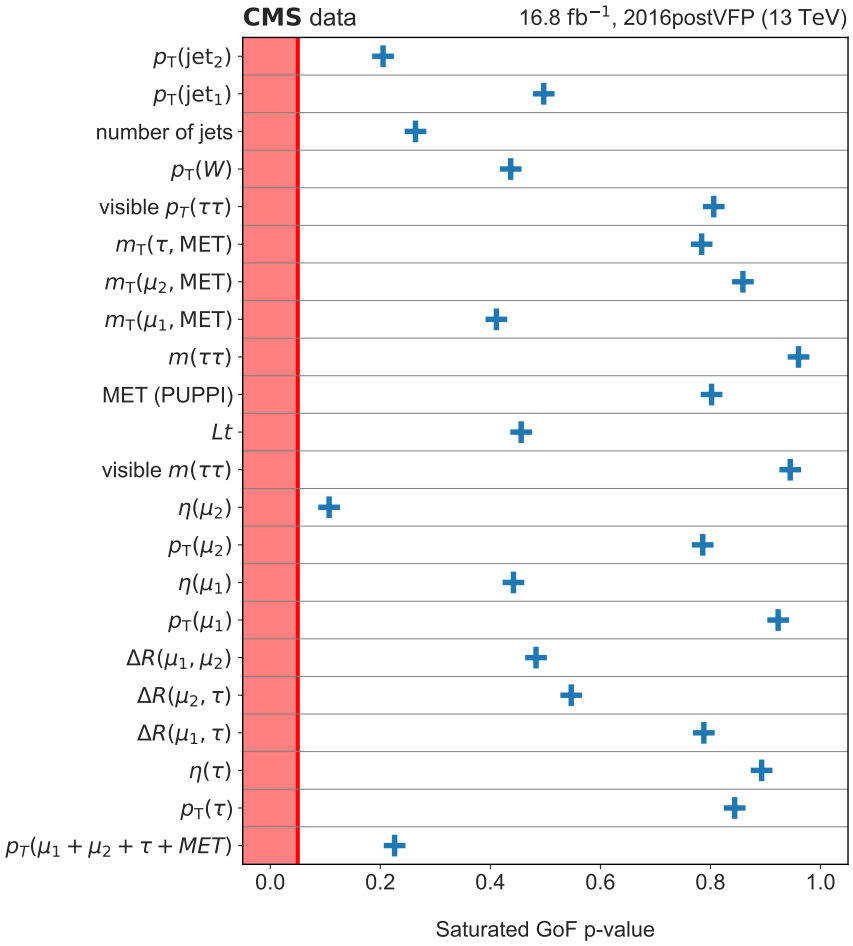

Figure A.28.: Results for the 1D GoF tests for the input variables used for the NN classification in the $\mu\mu\tau_h$ final state using 2016postVFP data.

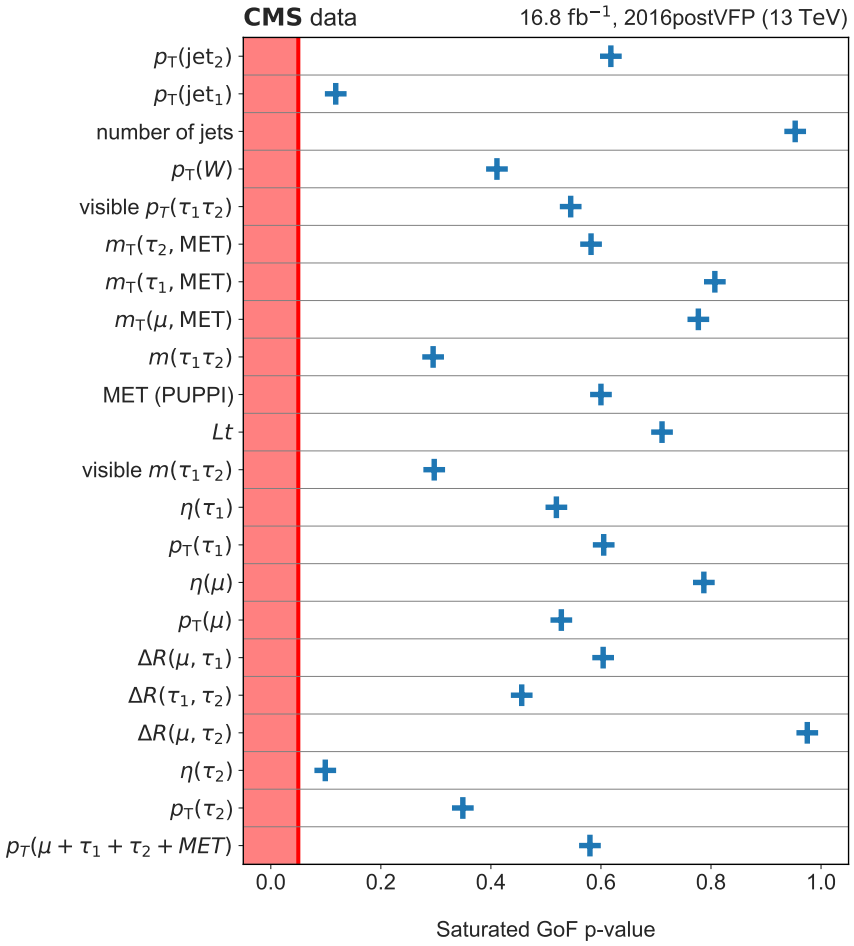

Figure A.29.: Results for the 1D GoF tests for the input variables used for the NN classification in the $\mu\tau_h\tau_h$ final state using 2016postVFP data.

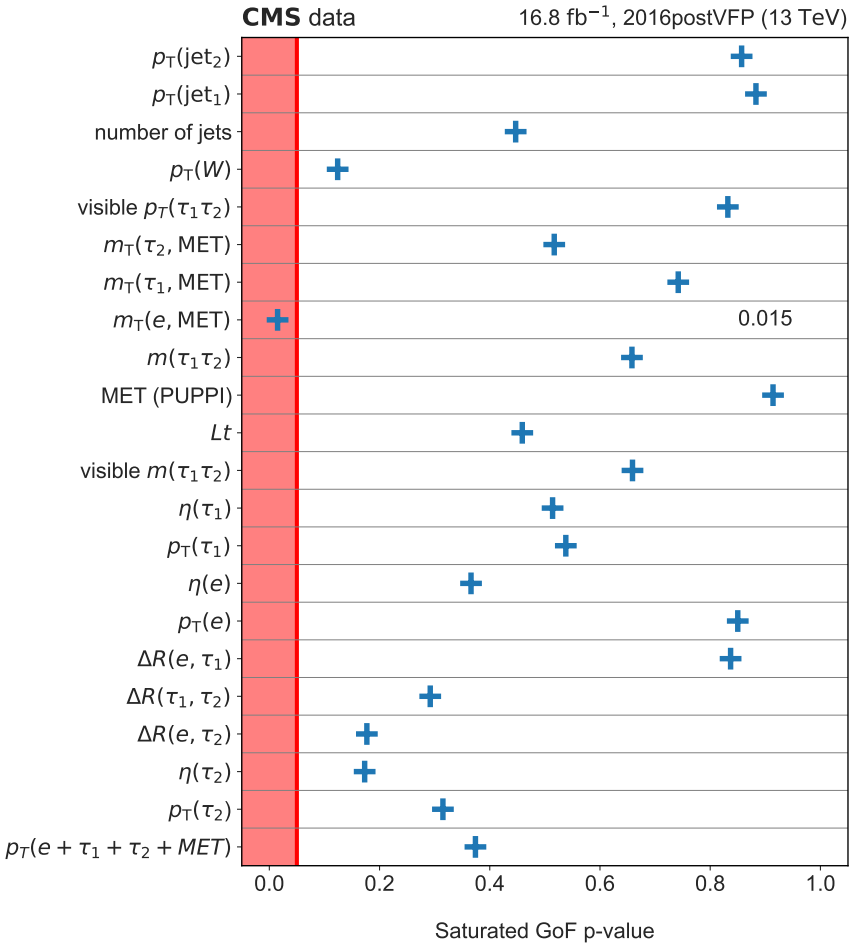

Figure A.30.: Results for the 1D GoF tests for the input variables used for the NN classification in the $e\tau_h\tau_h$ final state using 2016postVFP data.

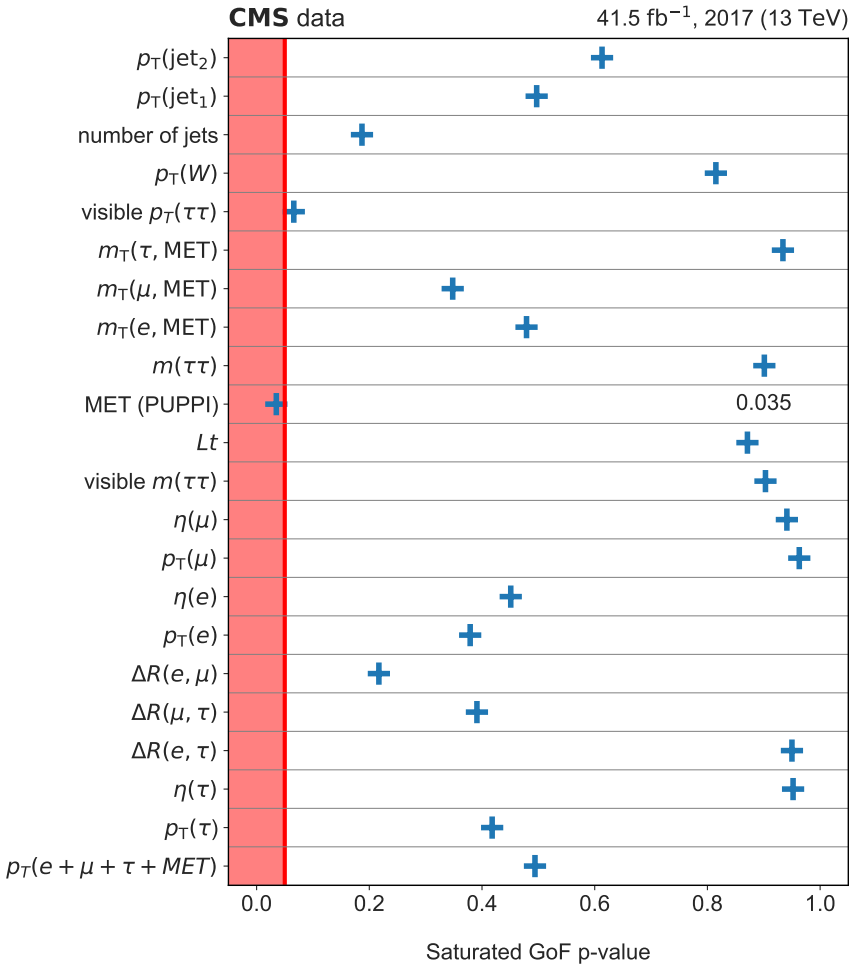

Figure A.31.: Results for the 1D GoF tests for the input variables used for the NN classification in the e$\mu\tau_h$ final state using 2017 data.

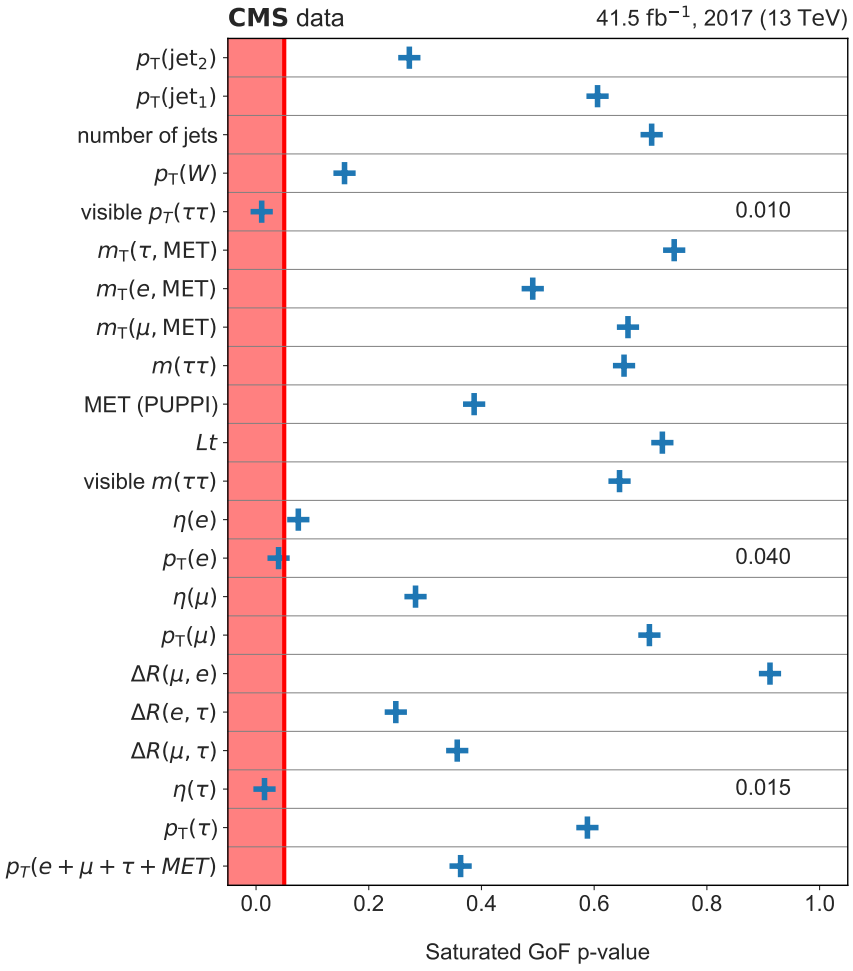

Figure A.32.: Results for the 1D GoF tests for the input variables used for the NN classification in the $\mu e \tau_h$ final state using 2017 data.

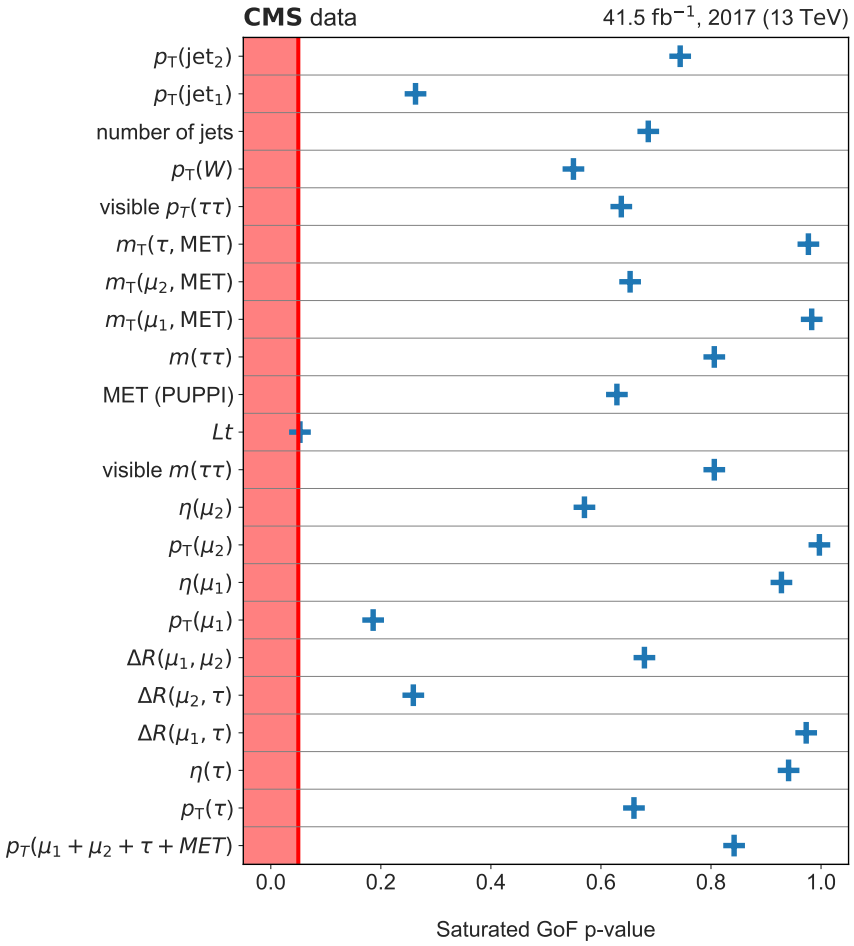

Figure A.33.: Results for the 1D GoF tests for the input variables used for the NN classification in the $\mu\mu\tau_h$ final state using 2017 data.

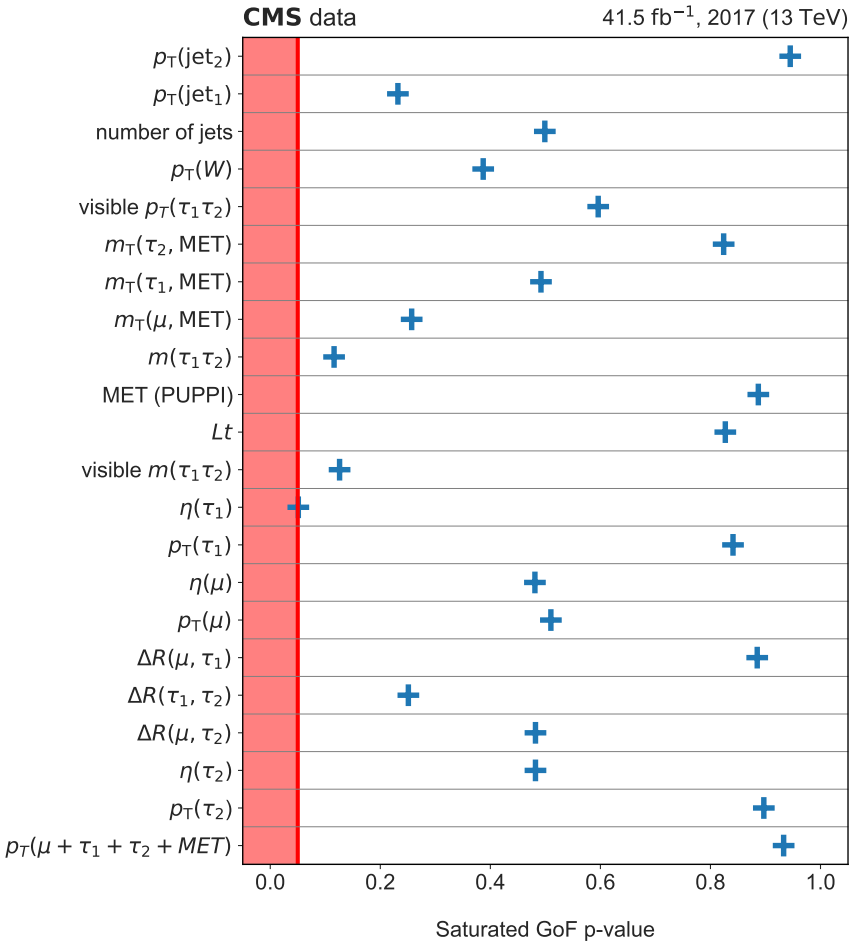

Figure A.34.: Results for the 1D GoF tests for the input variables used for the NN classification in the $\mu\tau_h\tau_h$ final state using 2017 data.

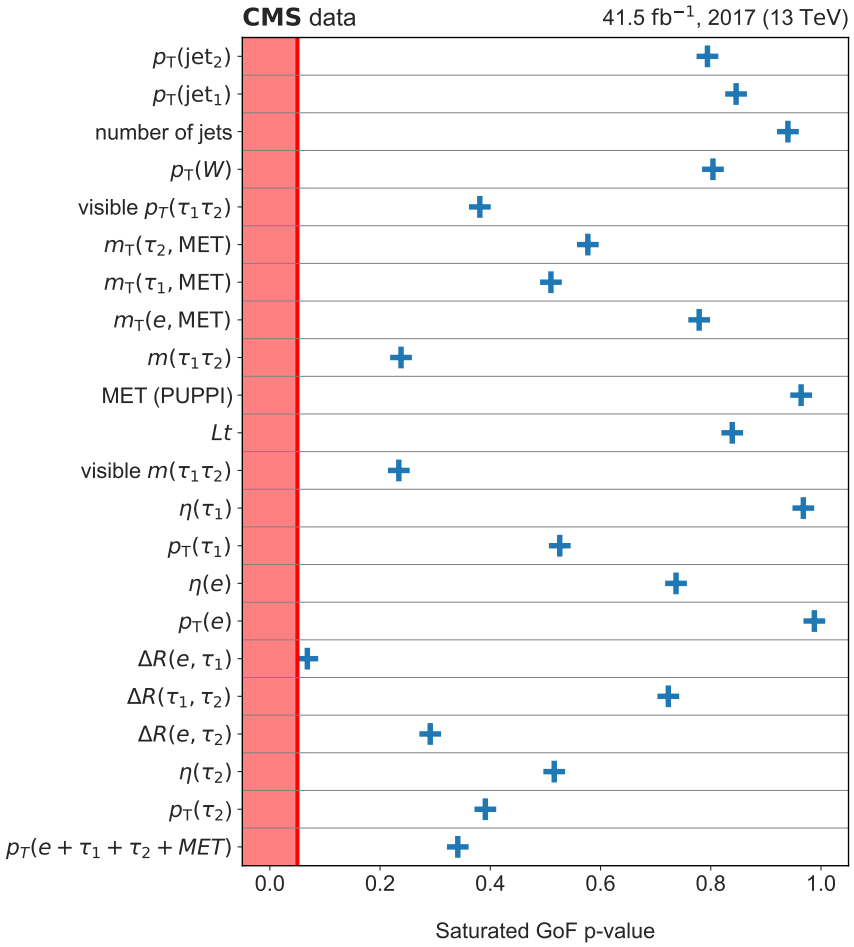

Figure A.35.: Results for the 1D GoF tests for the input variables used for the NN classification in the $e\tau_h\tau_h$ final state using 2017 data.

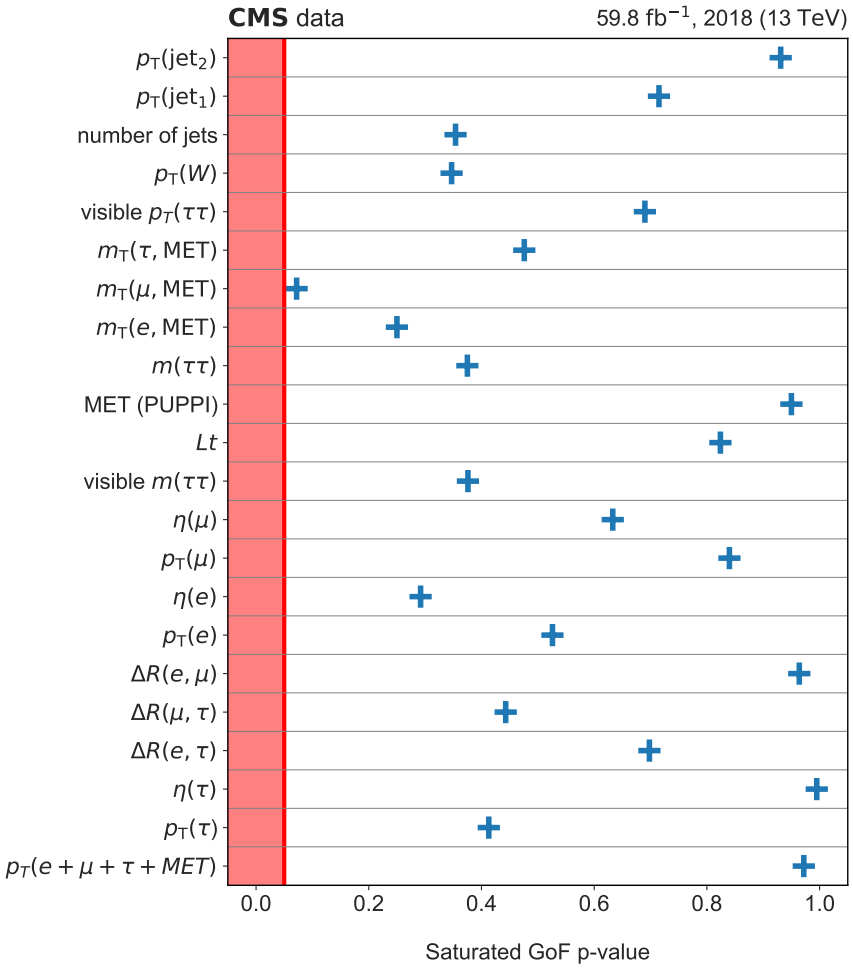

Figure A.36.: Results for the 1D GoF tests for the input variables used for the NN classification in the e$\mu\tau_h$ final state using 2018 data.

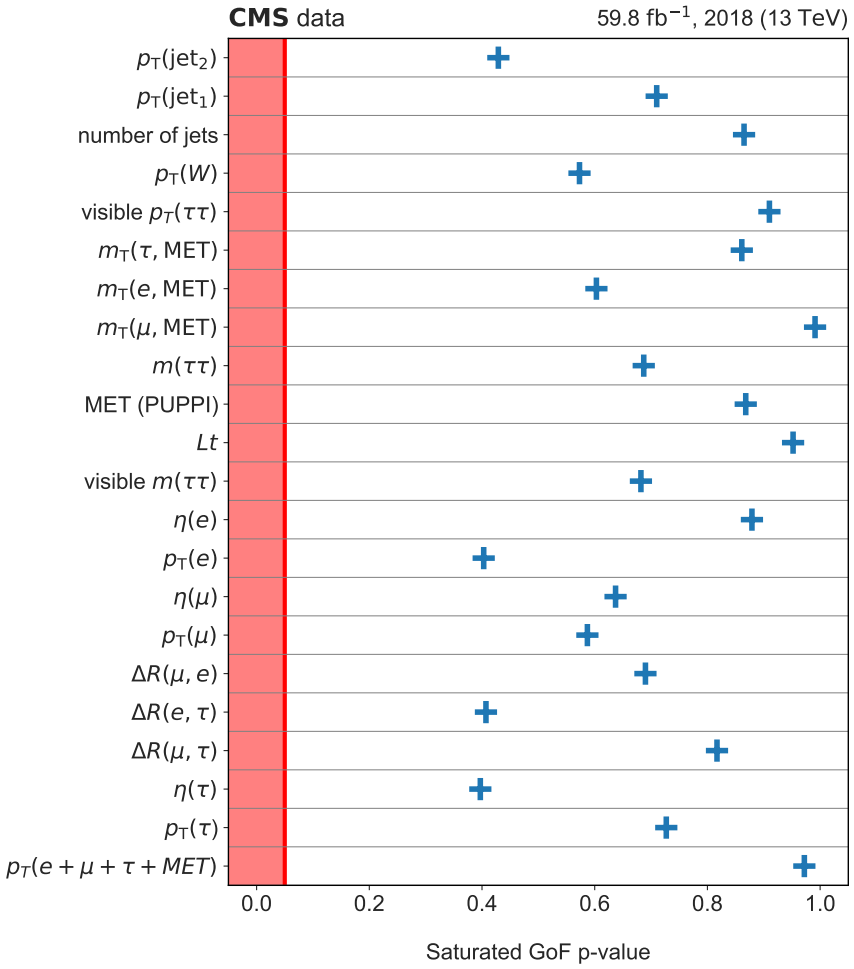

Figure A.37.: Results for the 1D GoF tests for the input variables used for the NN classification in the $\mu e \tau_h$ final state using 2018 data.

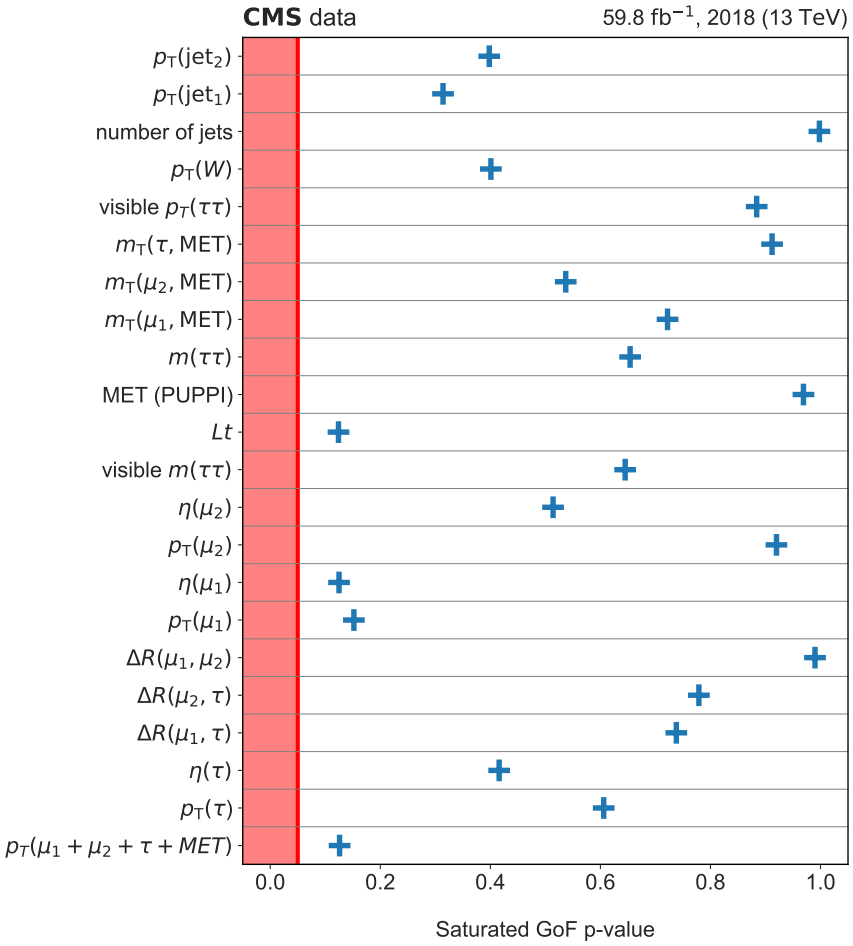

Figure A.38.: Results for the 1D GoF tests for the input variables used for the NN classification in the $\mu\mu\tau_h$ final state using 2018 data.

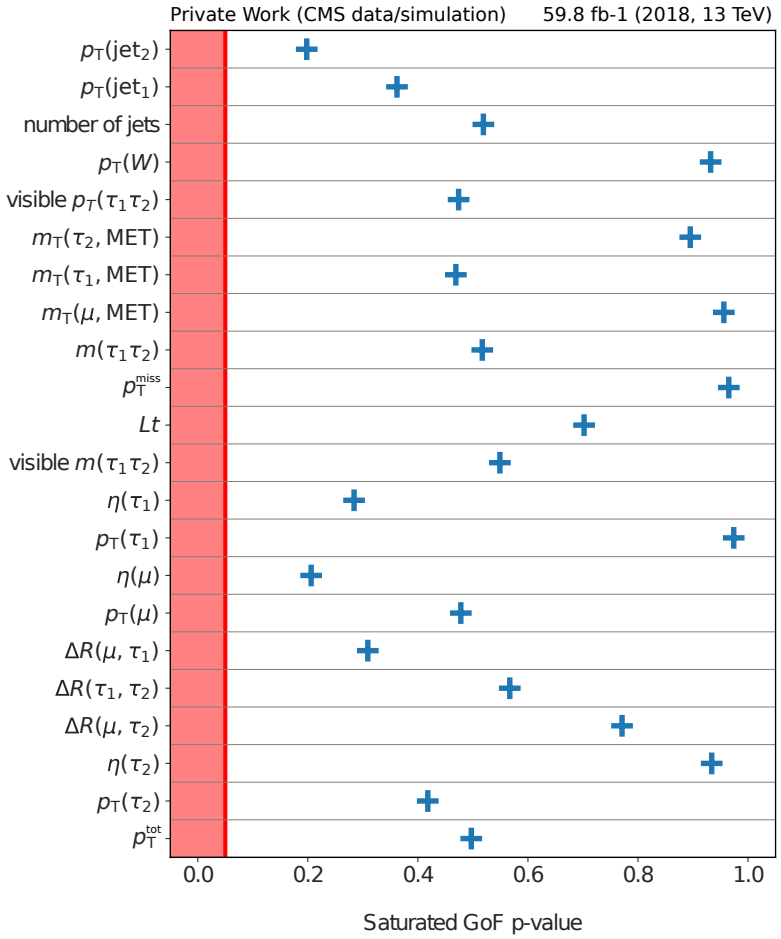

Figure A.39.: Results for the 1D GoF tests for the input variables used for the NN classification in the $\mu\tau_h\tau_h$ final state using 2018 data.

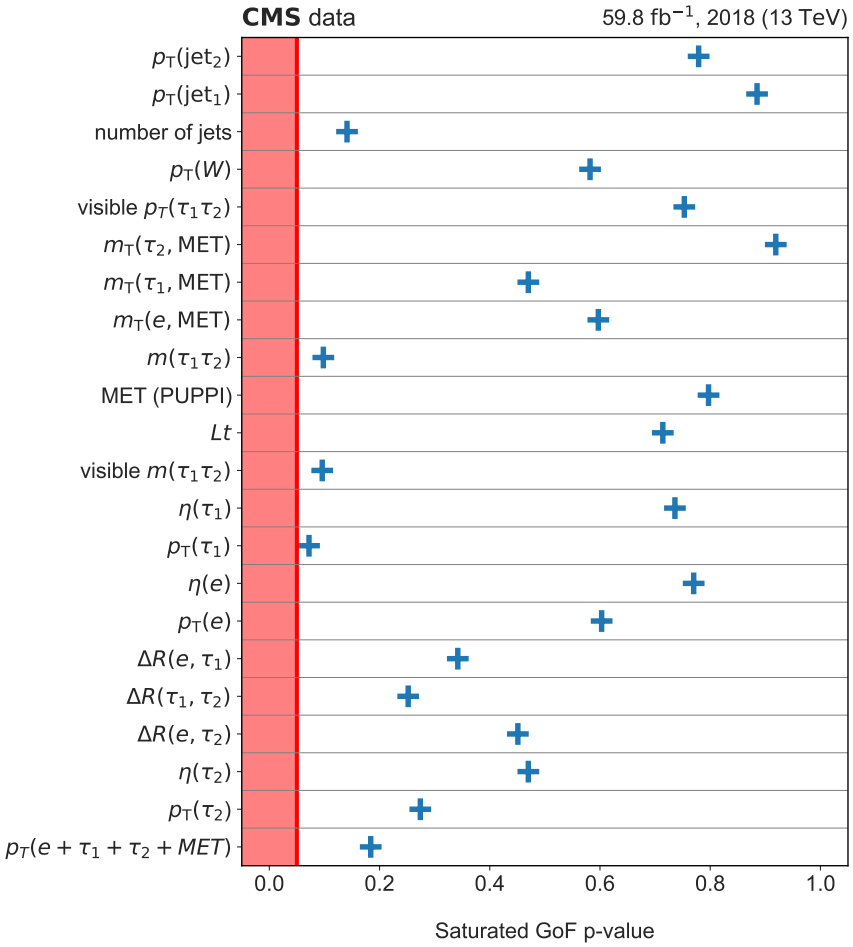

Figure A.40.: Results for the 1D GoF tests for the input variables used for the NN classification in the $e\tau_h\tau_h$ final state using 2018 data.

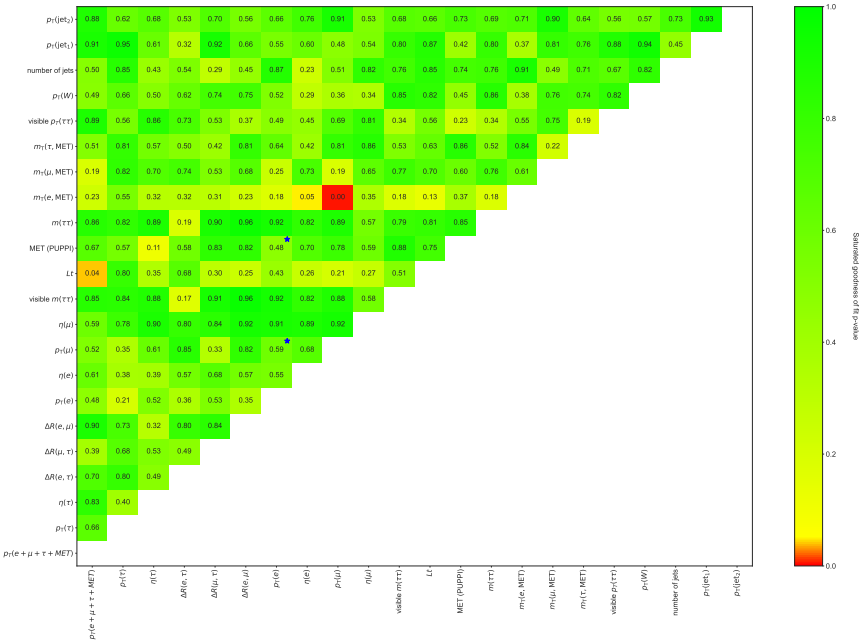

Figure A.41.: Results for the 2d GoF tests for the input variables used for the NN classification in the e$\mu\tau_h$ final state using 2016preVFP data.

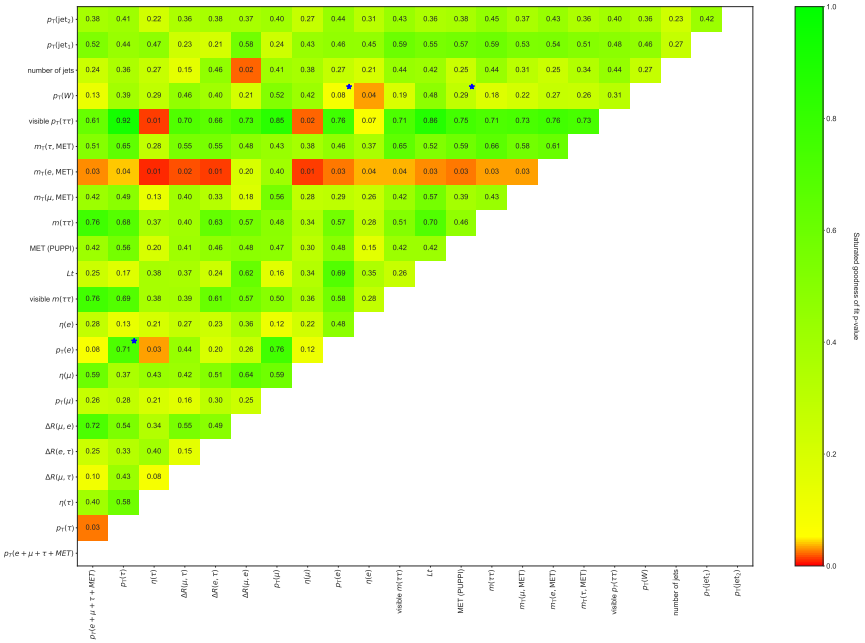

Figure A.42.: Results for the 2d GoF tests for the input variables used for the NN classification in the $\mu e \tau_h$ final state using 2016preVFP data.

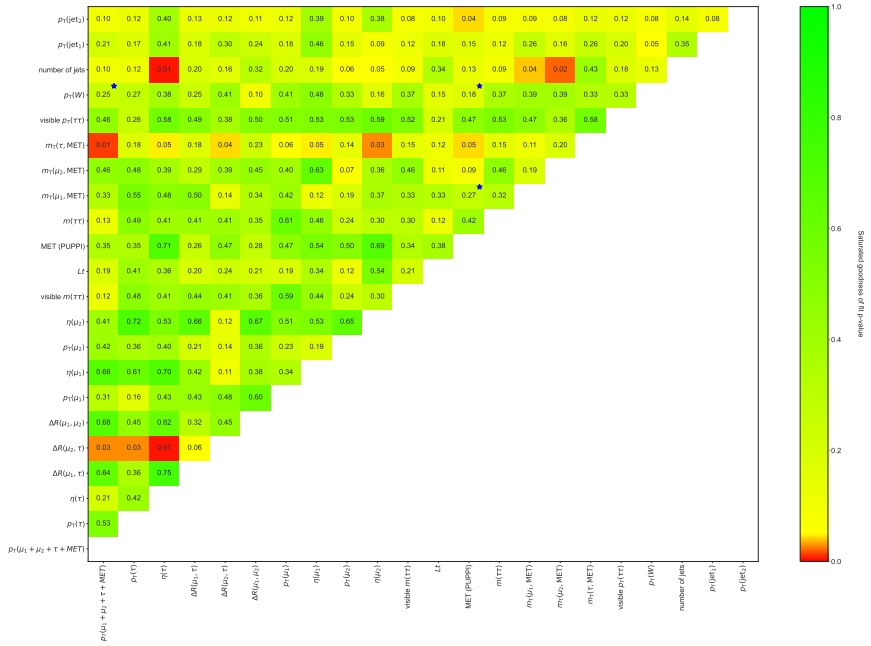

Figure A.43.: Results for the 2d GoF tests for the input variables used for the NN classification in the $\mu\mu\tau_h$ final state using 2016preVFP data.

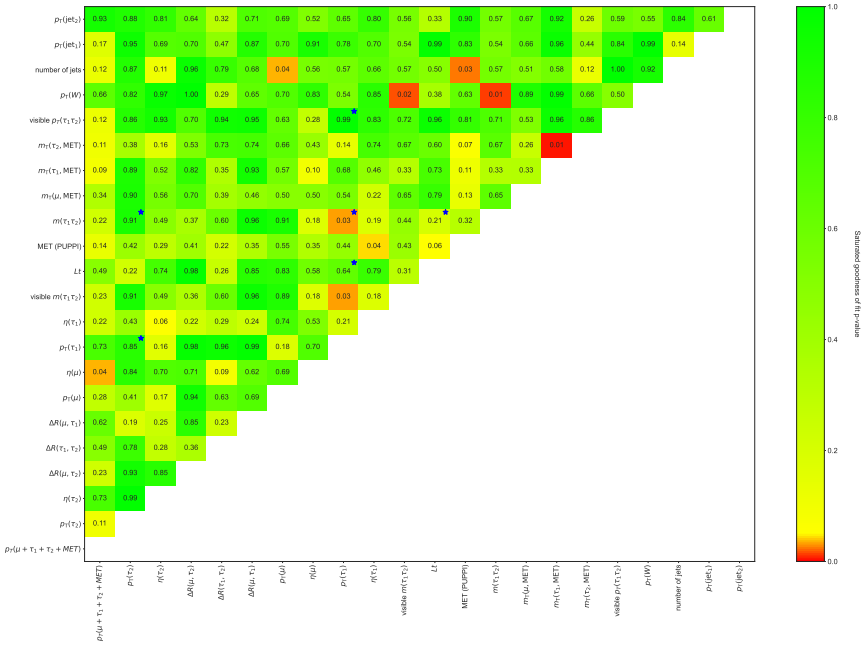

Figure A.44.: Results for the 2d GoF tests for the input variables used for the NN classification in the $\mu\tau_h\tau_h$ final state using 2016preVFP data.

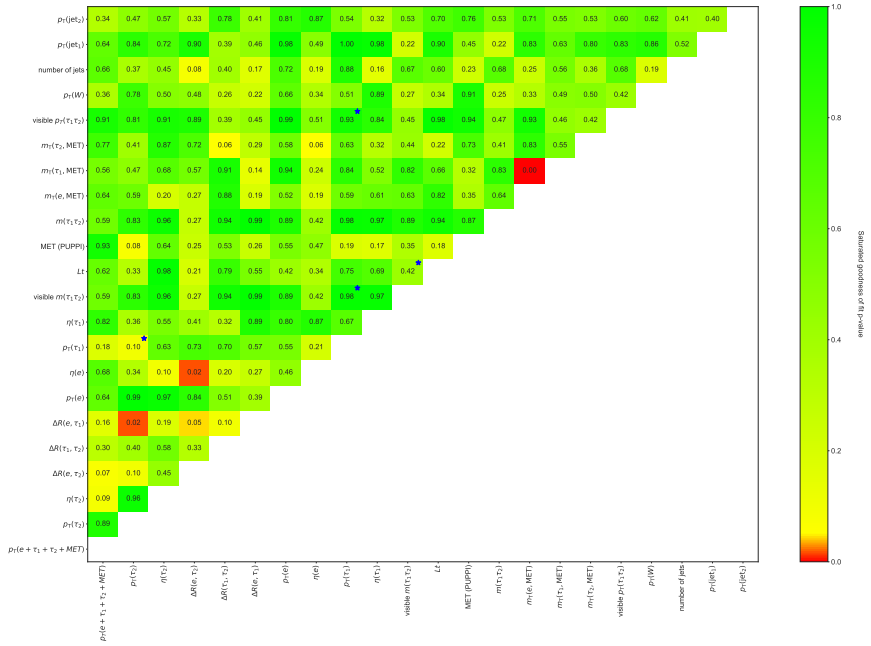

Figure A.45.: Results for the 2d GoF tests for the input variables used for the NN classification in the $e\tau_h\tau_h$ final state using 2016preVFP data.

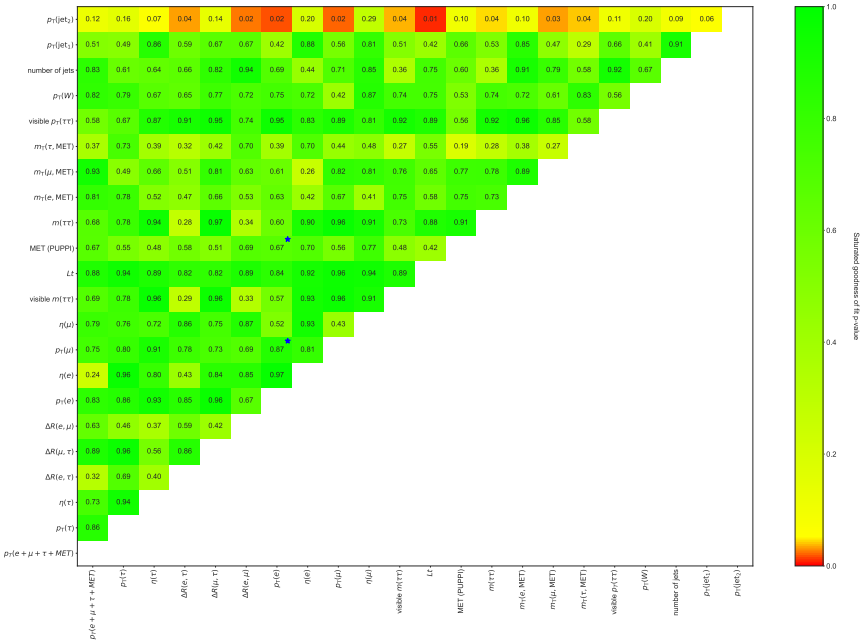

Figure A.46.: Results for the 2d GoF tests for the input variables used for the NN classification in the e$\mu\tau_\mathrm{h}$ final state using 2016postVFP data.

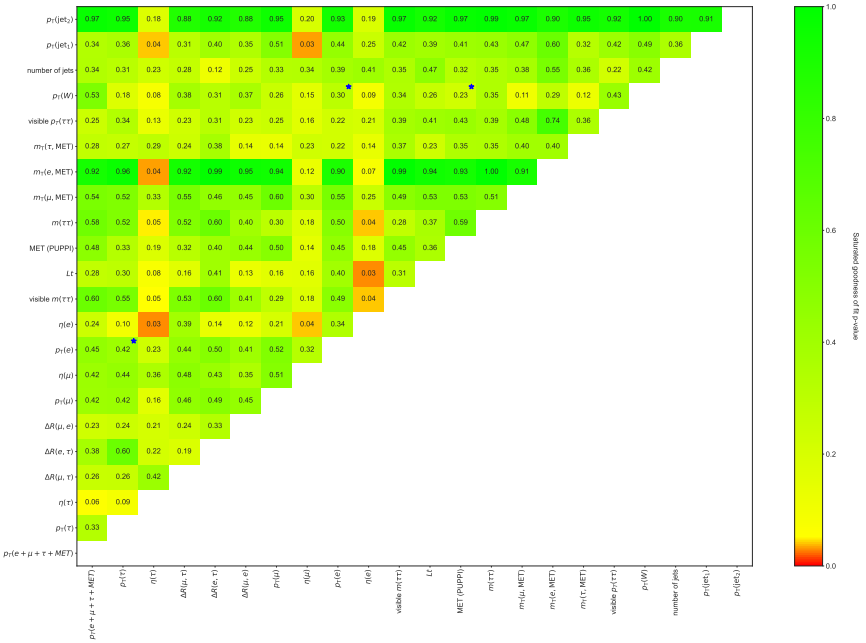

Figure A.47.: Results for the 2d GoF tests for the input variables used for the NN classification in the $\mu e \tau_h$ final state using 2016postVFP data.

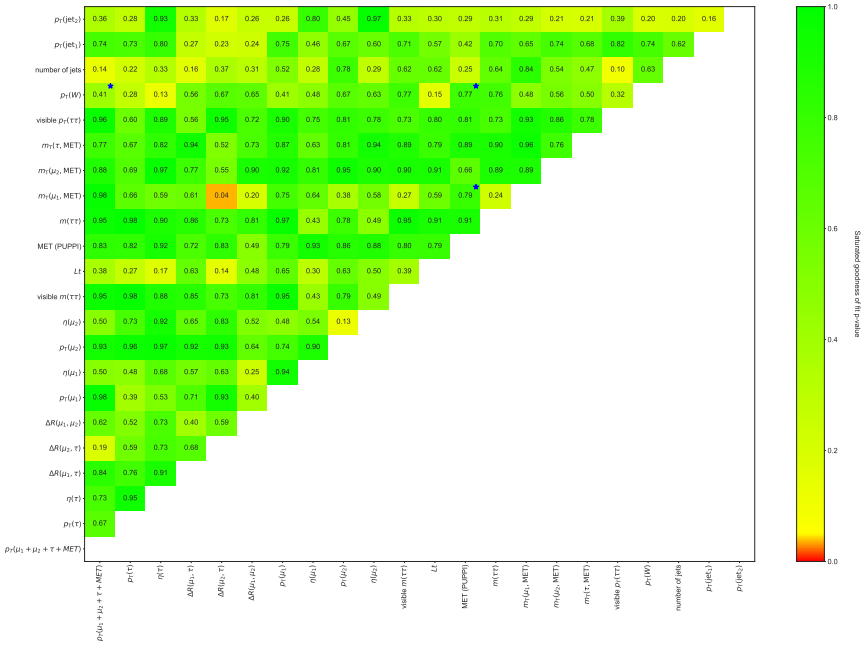

Figure A.48.: Results for the 2d GoF tests for the input variables used for the NN classification in the $\mu\mu\tau_h$ final state using 2016postVFP data.

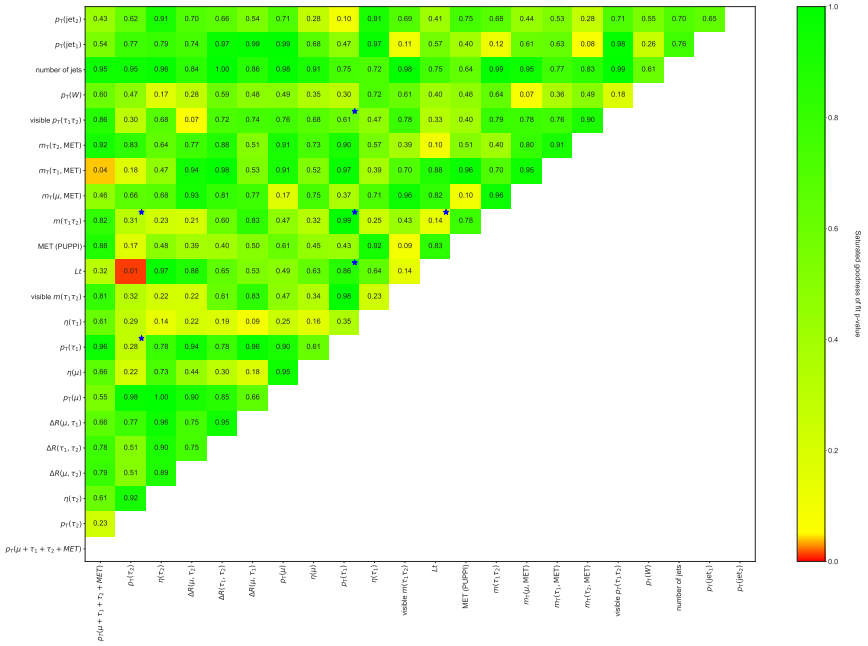

Figure A.49.: Results for the 2d GoF tests for the input variables used for the NN classification in the $\mu\tau_h\tau_h$ final state using 2016postVFP data.

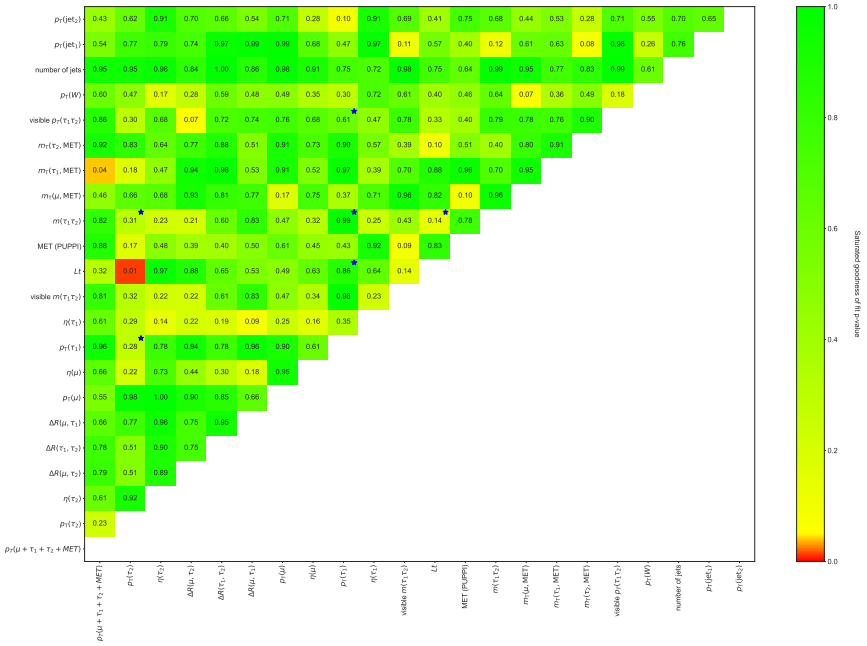

Figure A.50.: Results for the 2d GoF tests for the input variables used for the NN classification in the $\mu\tau_h\tau_h$ final state using 2016postVFP data.

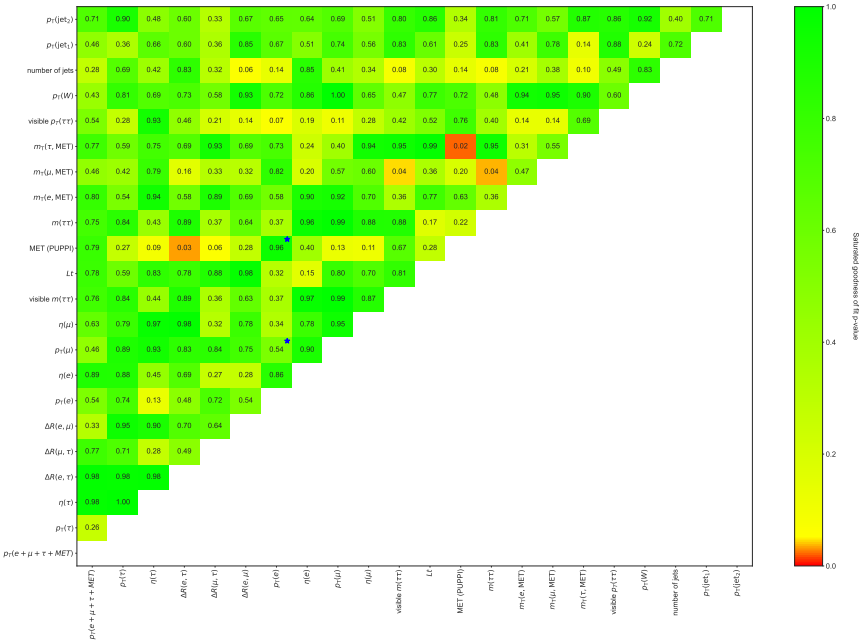

Figure A.51.: Results for the 2d GoF tests for the input variables used for the NN classification in the e$\mu\tau_h$ final state using 2017 data.

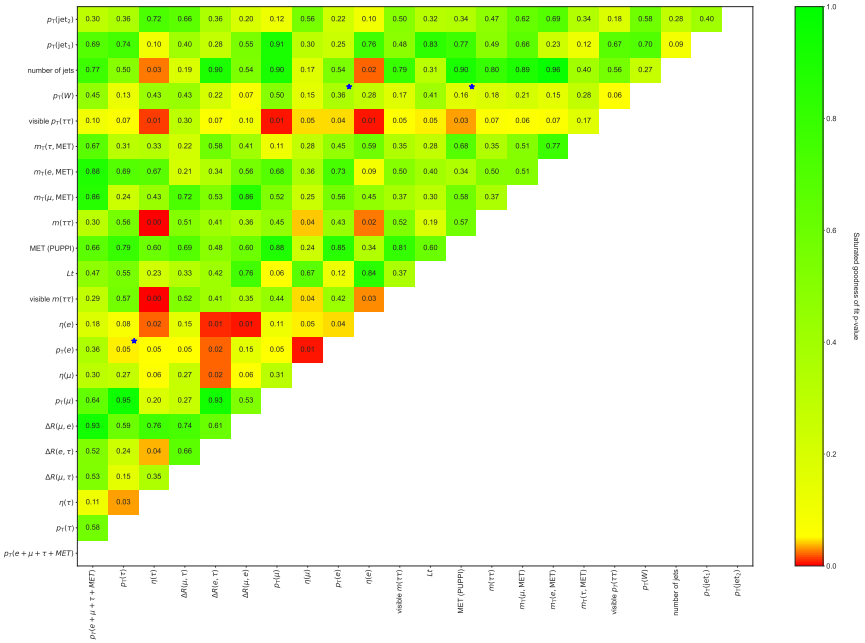

Figure A.52.: Results for the 2d GoF tests for the input variables used for the NN classification in the $\mu e \tau_h$ final state using 2017 data.

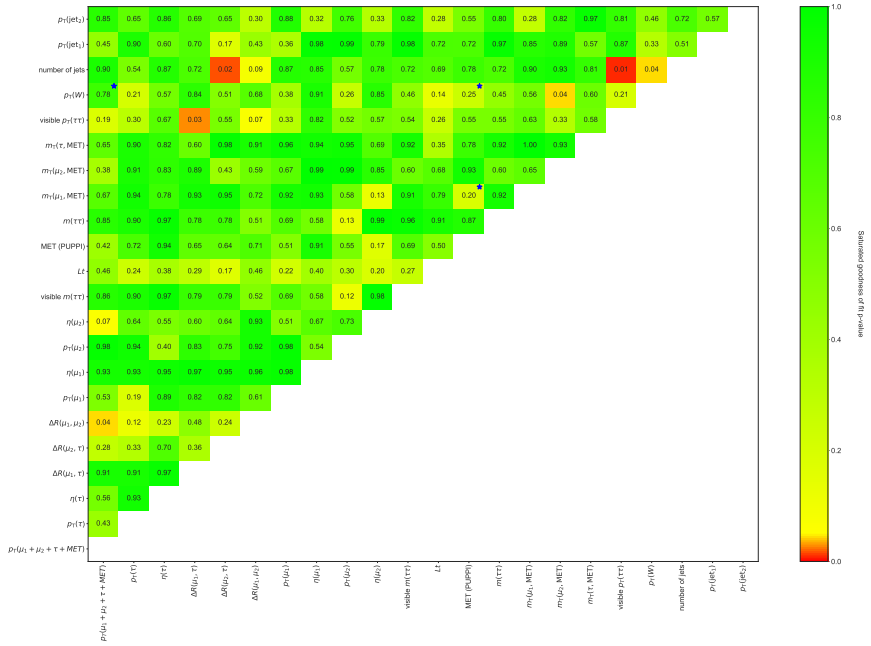

Figure A.53.: Results for the 2d GoF tests for the input variables used for the NN classification in the $\mu\mu\tau_h$ final state using 2017 data.

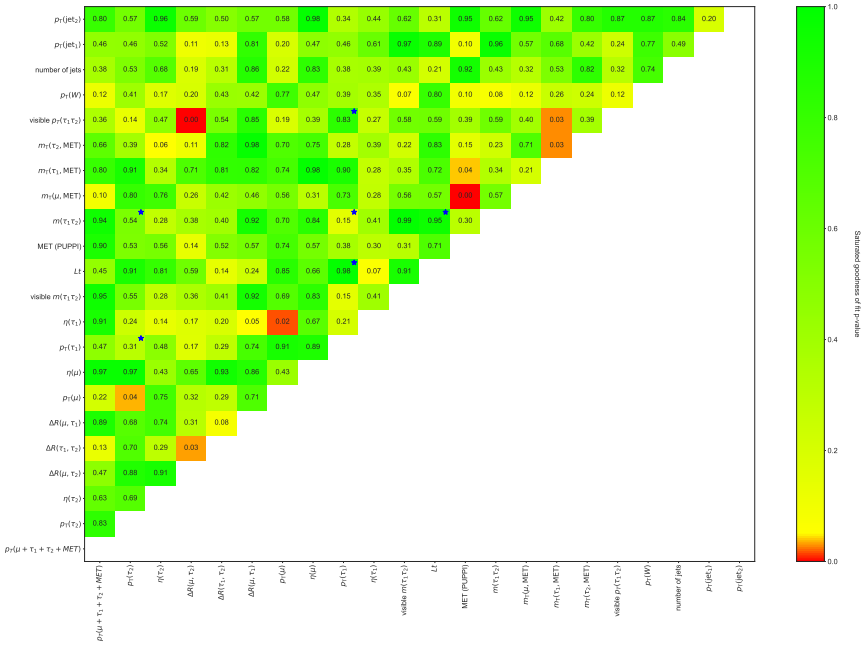

Figure A.54.: Results for the 2d GoF tests for the input variables used for the NN classification in the $\mu\tau_h\tau_h$ final state using 2017 data.

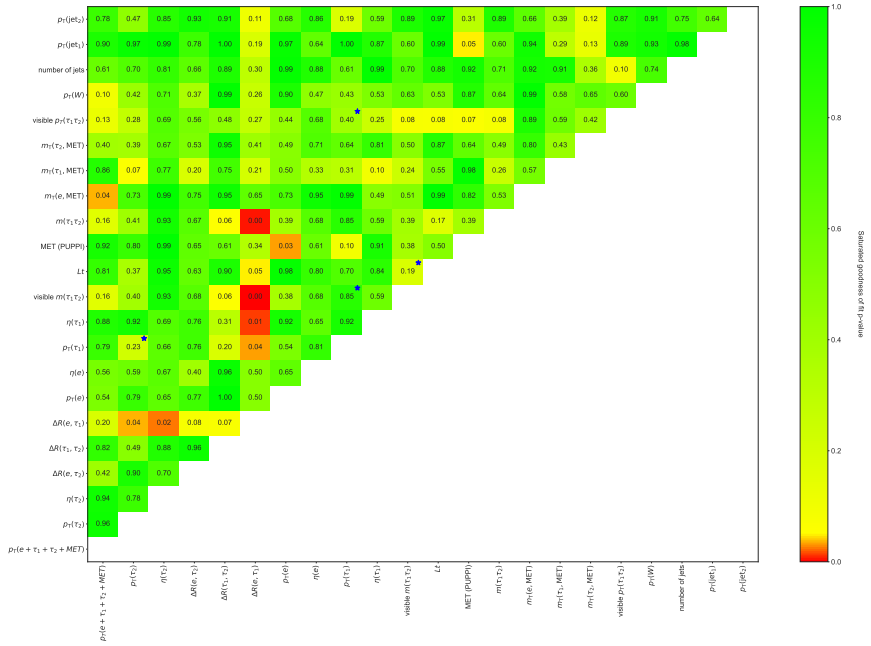

Figure A.55.: Results for the 2d GoF tests for the input variables used for the NN classification in the $e\tau_h\tau_h$ final state using 2017 data.

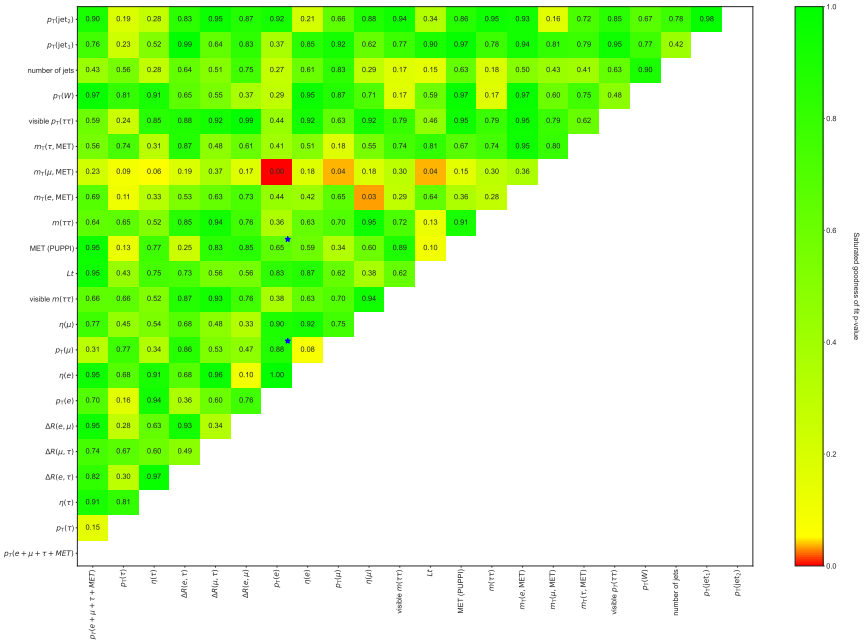

Figure A.56.: Results for the 2d GoF tests for the input variables used for the NN classification in the e$\mu\tau_h$ final state using 2018 data.

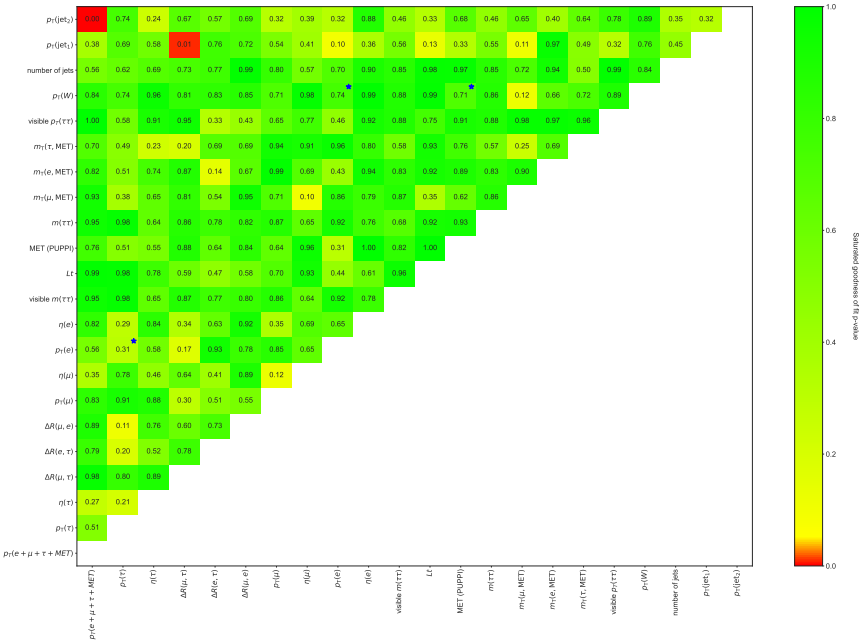

Figure A.57.: Results for the 2d GoF tests for the input variables used for the NN classification in the $\mu e \tau_h$ final state using 2018 data.

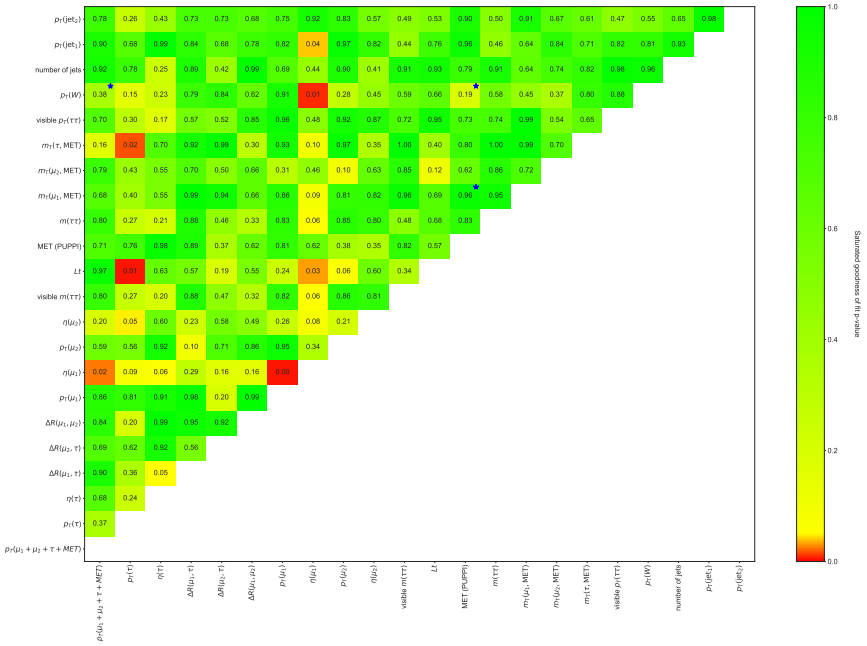

Figure A.58.: Results for the 2d GoF tests for the input variables used for the NN classification in the $\mu\mu\tau_h$ final state using 2018 data.

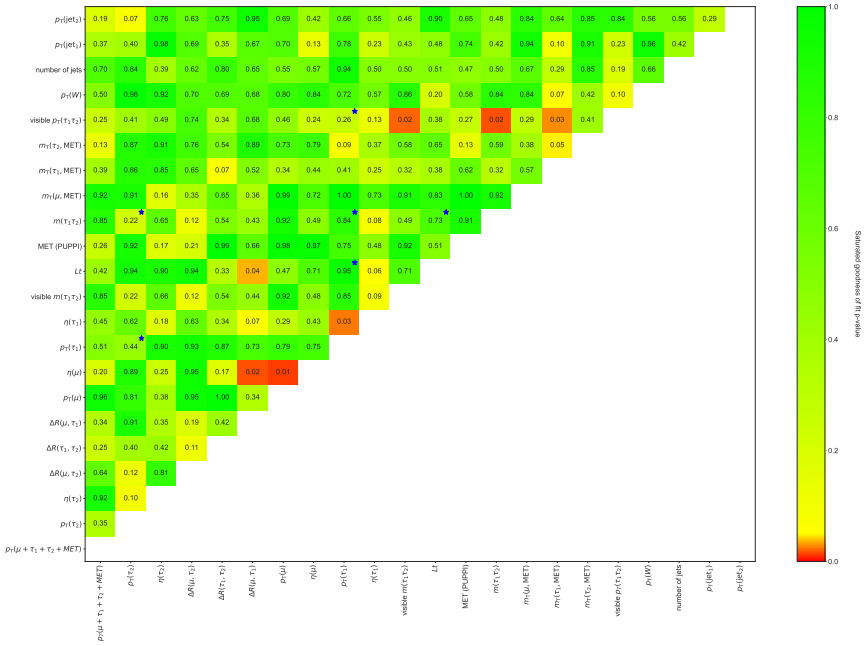

Figure A.59.: Results for the 2d GoF tests for the input variables used for the NN classification in the $\mu\tau_h\tau_h$ final state using 2018 data.

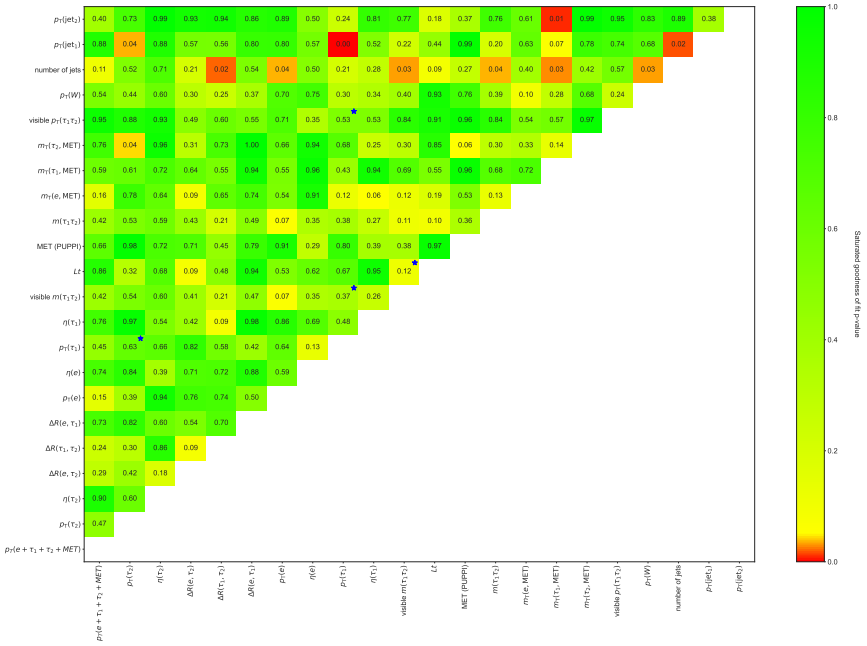

Figure A.60.: Results for the 2d GoF tests for the input variables used for the NN classification in the $e\tau_h\tau_h$ final state using 2018 data.

List of Figures

List of Tables

Acknowledgments

Ein großer Abschnitt in meinem Leben geht zu Ende. Seid 10 Jahren mache ich nun Physik, vier Jahre davon als Doktorand am ETP. In dieser Zeit habe ich viel gelernt, sowohl über Physik und Datenanalyse als auch über mich. Ich würde mich sehr gerne bei den Menschen bedanken, die mir die Möglichkeit gegeben haben und mich über diese Zeit begleitet und unterstützt haben.

Zunächst möchte ich Markus Klute dafür danken, dass er mir die Möglichkeit gegeben hat, nach der Masterarbeit am ETP weiterarbeiten zu können und für die stete Unterstützung während der Arbeit. Ich war zu dieser Zeit unsicher, was ich machen soll, aber ich wusste, dass ich mich hier am ETP sehr wohlfühle. Das hat letztlich den Ausschlag für die Entscheidung weiterzumachen gegeben und ich bin sehr froh darüber.

Als nächstes möchte ich mich bei meinem direkten Betreuer Roger Wolf bedanken. Ich habe mich immer sehr unterstützt und gehört gefühlt und das schätze ich wirklich sehr. Jederzeit konnte ich vorbeikommen und bei ihm klopfen. Er hatte immer ein offenes Ohr, wenn ich eine Diskussion gebraucht habe. Er wusste mich zu motivieren, wenn ich es gebraucht habe, zu bestärken, wenn ich unsicher war und mir Freiraum zu lassen, wenn es gut lief. Vor allem im letzten Jahr, als wir gemeinsam aus der Arbeit das Papier geschrieben haben, war er quasi ein 24/7 support.

Sowohl Markus als auch Roger möchte ich dafür danken, dass ich neben der Doktorarbeit genug Kapazität hatte meiner politischen Arbeit nachzugehen wodurch ich weniger Arbeitsstunden hatte als die meisten Doktorant*innen. Ich finde das überhaupt nicht selbstverständlich und respektiere das wirklich sehr.

Vielen lieben Dank an die ETP-Higgs Arbeitsgruppe für das ständige Feedback und die Diskussionen. Es ist ein tolles, hilfsbereites Klima bei uns. Besonders möchte ich mich bei Nikita, Artur, Christian, Nicolò und Maximilian für ihre Unterstützung bedanken. Ein ganz wichtiger Teil meines PhDs war Büro 8/16 mit Christian, Florian und Sebastian. Es hat richtig viel Spaß gemacht mit euch das Büro zu teilen. Hier möchte ich besonders Sebastian hervorheben. Mein Bürogenosse, der mich so sehr unterstützt hat. Ich glaube, ich wage mich nicht zu weit aus dem Fenster, wenn ich sage: ohne Sebastian wäre das nichts geworden. Danke.

Vielen lieben Dank an meine Eltern und Schwestern, an meine Freundin Irene und meine Freunde Felix und Pablo. Eure Liebe gibt mir soviel Lebensfreude und Energie. Bei euch kann ich mich zurückziehen, ich sein und fühle mich bedingungslos unterstützt. Ihr habt meine Klagen, Ängste und Zweifel angehört, mich bestärkt einen Weg zu finden, der für mich gut ist. Mit euch in Beziehung zu sein ist ein großes Privileg.